University of Alberta

Graphene Reinforced Adhesives for Improved Joint Characteristics in Large Diameter Composite Piping

by

Avinash Parashar

A thesis submitted to the Faculty of Graduates Studies and Research
in partial fulfilment of the requirement for the degree of

Doctor of Philosophy

Department of Mechanical Engineering

Spring 2013
Edmonton, Alberta

Abstract

Higher specific properties and corrosion resistance of fibre reinforced polymer (FRP) pipes make them a potential candidate for replacing metallic piping structures. This research project is concerned with adhesively bonded FRP pipe sections. The project can broadly be classified into three phases. In the first phase the effects of dimensional scaling as well as fibre architecture on adhesive bonding strength were studied. A macro analysis of adhesively bonded FRP pipe sections was conducted employing a finite element approach in conjunction with strength of materials and fracture mechanics damage criteria. Through this phase of the project the most damage-prone components within adhesively bonded FRP pipe sections were identified. The second phase of the research project was designed to investigate a suitable nanofiller material for the reinforcement of the weakest joint component, i.e. the adhesive bondline. Due to its superior mechanical properties and relatively low cost, graphene was considered as the nanofiller. Phase two of the project was further extended to include a novel modelling technique for characterizing graphene at the atomistic level. The third and final phase of the project dealt with the overall impact of graphene nanofiller on the adhesive material. A multiscale model was developed to investigate fracture toughening and stability effects with the aim of producing a nanocomposite with improved mechanical properties.

Acknowledgement

I would like to express my sincere thankfulness to my advisor Dr. Pierre Mertiny for the valuable guidance, patience and support that he provided throughout the course of my doctoral thesis work. I would like to extend my thanks to Dr. Zihui Xia for his support and advice during my thesis work. Further, I would like to acknowledge the help and support that I received from my colleagues at the Advanced Composite Materials Engineering Group.

I would like to express my appreciation to the Natural Sciences and Engineering Research Council of Canada, Alberta Innovates, the American Society of Mechanical Engineers, the University of Alberta and the Department of Mechanical Engineering for recommending and awarding prestigious scholarships.

I would like to express my deep gratitude to my parents, Rahul, Rachna and Akanksha for their support and encouragement. Finally, I would like to thank my twin daughters Aparna and Agrata for being a source of energy and inspiration.

Table of Contents

Abstract

Acknowledgement

Table of Contents

List of Tables

List of Figures

List of Tables

List of Figures

Chapter 1: Introduction

1.1 Background to current study

Fibre reinforced polymer (FRP)composite pipes are emerging as a potential candidate for replacing metallic piping structures since the latter are more susceptible to environmental degradation such as corrosion and wear. Higher specific strength and stiffness make a FRP composite a superior structural material when weight is also a design requirement. Higher costs of composite piping can be compensated for with lower maintenance needs, longer system life and ease of transportation. Another advantage associated with composite structures is the large number of design variables, which allow a composite structure to be tailored closely to the design requirements. Despite the advantages associated with FRP structures, their application is still limited, partly due to unsatisfactory methods for joining composite subcomponents and inadequate knowledge of failure mechanisms under different loading conditions. Adhesive bonding is emerging as a promising technique to join tubular FRP structures. The ability to maintain an undamaged fibre architecture is a major advantage with adhesive bonding technology. Adhesively bonded joints are also attractive for many applications since they offer integrated sealing and minimal part count and do not require pipe extremities with complex geometries such as threads or bell and spigot configurations. Generally an adhesive joint results in a more uniform stress distribution owing to an undamaged fibre architecture and smooth surface contours.

An important area of research pertaining to FRP piping is the connection of pipe sections. Challenges associated with the joining of FRP tubular sections are often considerable, which limits more widespread industrial application. In this research project the focus was set on identifying the limitations associated with the adhesive bonding technique for FRP pipe subsections, and efforts were made to propose a numerical solution to overcome such shortcomings.

1.2 Introduction to fibre reinforced polymer (FRP)

A composite is a structural material with two or more constituent phases that are mixed at a meso-scale level. Composites consist of a reinforcing phase (e.g. fibres, particles, flasks, etc.) and a matrix material (e.g. polymer).

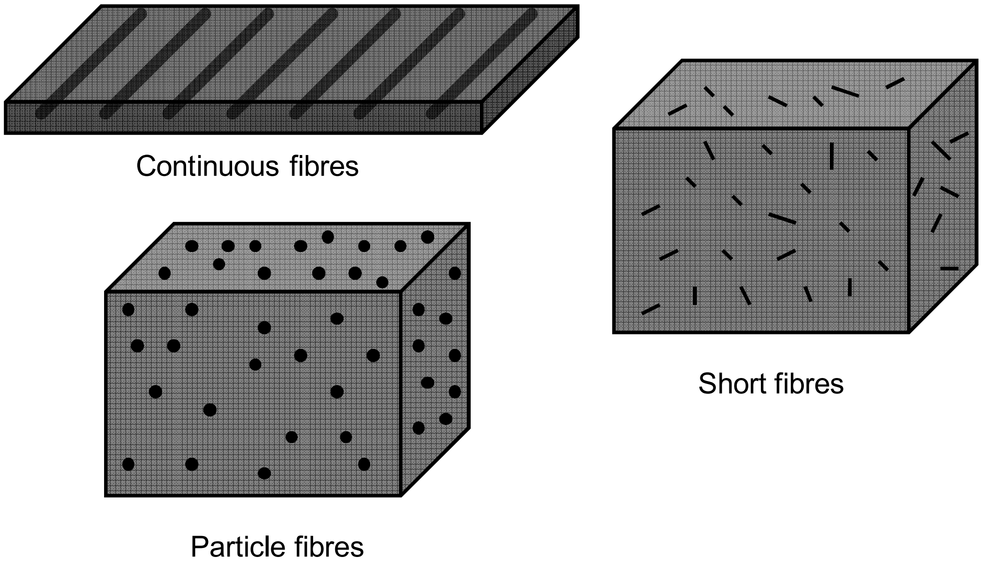

Fig.1.1 *Composites with different type of fibres, adopted from [1].*

<u>Matrix phase:</u>

The continuous material phase in a composite is termed the matrix. Its main function is to hold the reinforcement phase such as fibres in the required position/direction, and to transfer loads to and in between the reinforcing phase. The matrix has significant influence on damage initiation, and hence it is generally considered the weakest link in a composite.

Polymers have established themselves as a common matrix material for composites in many applications. The attractiveness of polymers for the role of matrix is that they are lightweight, often with a density of little more than unity, and they can be processes either in solution or a molten state. This results in low density composite materials, simple forming tools, relative ease of fibre matrix impregnation, and ultimately low cost of manufacturing. Moreover, polymers are highly resistant to corrosive environments, which provides composites with further valuable properties. Polymers used as matrix materials can be divided into two primary families, the nature of which depends on their molecular structures, these are thermosetting and thermoplastic resins.

Reinforcing phase:

The reinforcing phase can also be defined on the basis of dimension, e.g. continuous fibres, shorts fibres and particles (as shown in Fig.1.1). Continuous fibres are the most common reinforcing constituent in composites and allow for high volume fractions. Fibres are the main load-bearing component in composites. The orientation of fibre phase is important for tailoring the mechanical properties in the development of a composite structure. Commonly employed fibres are glass fibres, carbon/graphite fibres, and Kevlar fibres.

1.3 Filament winding

Filament winding is commonly employed technique for the manufacturing of FRP tubular structures such as pressure vessels and pipes. As shown in Fig.1.2 the filament-winding process consists of depositing fibres under tension onto a mandrel. In this process the mandrel usually revolves about the longitudinal axis, while the winding machine carriage dispensing the fibres moves horizontally parallel to the longitudinal axis of the mandrel. Fibre tows/strands are run through a resin wet dip or drum bath system where the fibres are impregnated with resin matrix. After the impregnation of the fibres with resin, the fibre tows are placed on the revolving mandrel in the desired pattern to obtained properties tailored for the desired performance of the composite structures.

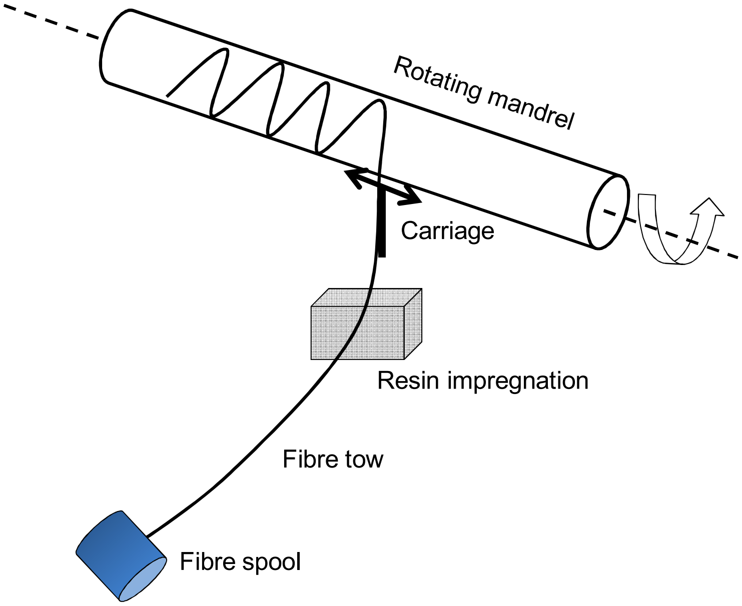

Fig.1.2 *Filament winding process, adopted from [2].*

1.4 Introduction to nanocomposites

During the last two decades, strong emphasis has been made by the researcher community to develop polymer nanocomposites. Polymer nanocomposites are defined with respect to the dimensions of the filler material, which is in the order of nanometers. In general, the unique combination of specific mechanical properties of nanofillers (e.g. stiffness, strength) and low concentration required to affect the overall properties of the polymer, places nanocomposites among the group of the most advanced materials [3].

The transition from micro to nanoparticles is accompanied by a significant shift in the physical properties of the material under consideration. Nanoscale particles are superior fillers due to a large surface area for the given volume [4].Final properties of the developed nanocomposite depend on the size or scale of its constituent phases and the degree of mixing/dispersion.

1.4.1 Characterization techniques for nanocomposites

Characterization is a crucial step to comprehend the physical and chemical properties, and their enhancement, of developed nanocomposites. Various techniques to characterize the properties of nanocomposites are available to researchers [5]. Most commonly used are powerful techniques such X-ray diffraction, scanning electron microscopy (SEM) and transmission electron microscopy [6,7].

1.4.2 Carbon nanotube (nanocomposites)

Carbon nanotubes (CNTs) can be considered a graphene sheet rolled into a seamless cylindrical configuration with diameters in the order of nanometers (see Fig.1.3). Due to the high aspect ratio of CNT they have superior mechanical properties, while the C-C bond also makes them electrically/thermally conductive. During the last two decades significant emphasis has been made by researchers to develop CNTs as a reinforcing filler for conventional materials (such as polymers) [9-11].

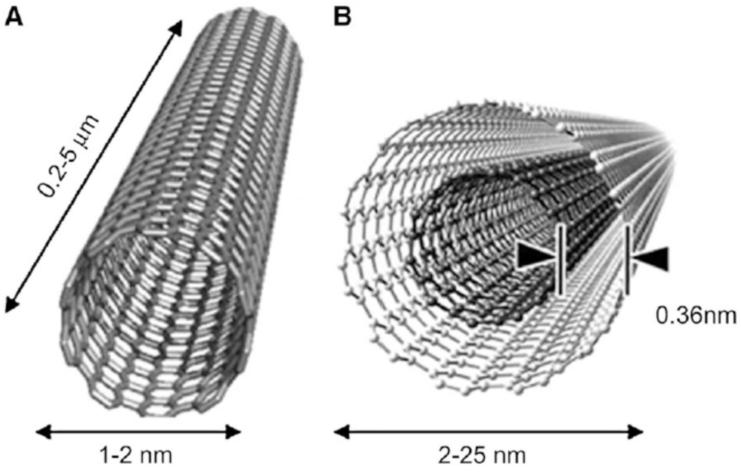

Fig.1.3 *Carbon nanotube configuration with dimensional parameters (A) Single wall (B) Multiwall [8].*

1.4.3 Nanoplatelet (nanocomposites)

Silicate clay and graphene based nanocomposites fall under the category of nanoplatelet nanocomposites. Clay material generally has a layered structure consisting of hydrous, magnesium or aluminum silicate [12]. Montmorillonite (MMT) is more commonly employed for reinforcing polymers due to its high surface area and surface reactivity as well as low cost. Natural graphite flakes also have a layered structure similar to nanoclays [13]. In graphene flakes each layer of carbon atoms is covalently bonded to the other carbon atoms, and these covalent bonds are responsible for providing the overall structural strength. Interlayer spacing between different graphite layers is maintained by weaker van der Waals forces. The weak inter-planar forces allow for certain atoms, molecules and ions to intercalate into the inter-planar spaces of graphite.

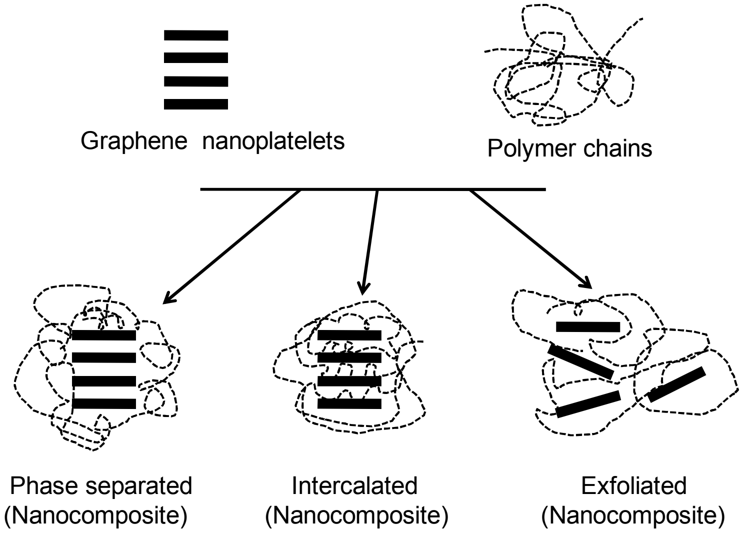

Fig.1.4 *Nanoplatellet nanocomposites [3].*

1.5 Outline of the thesis

The objective of this research project is to propose a numerical methodology for analysing and improving characteristics of adhesively bonded joints, particular for FRP composite piping structures. The research project has been divided into three phases.

Phase I:

Phase I of the research project, consisting of Chapters 2 and 3,deals with the macroscopic analysis and modelling of adhesively bonded FRP pipe sections. A literature review for adhesively bonded composite pipe sections is presented in Chapter 2. A numerical investigation was performed with respect to dimensional scaling and fibre architecture of adhesively bonded pipe sections, which is described in Chapter 3.

Phase II:

The second phase of the research project, which is incorporated into Chapters 4 and 5, was designed to investigate a suitable nanofiller material for the reinforcement of the weakest joint component, i.e. the adhesive bondline. A finite element based atomistic model was developed in this phase to characterize the mechanical properties of nanofiller. This phase, which concentrates on the atomistic modelling of the nanofiller, also provides insight into the effect of weak van der Waals interaction forces on the mechanical properties of the nanofiller itself.

Phase III:

The third and final phase of the research project presented in Chapters 6 and 7 describes and discusses multiscale aspects of modelling, which was performed to study the effect of nanofillers on the mechanical properties of the polymer nanocomposite. In this work, nanofillers and the polymer matrix were modelled on the atomistic scale and as a continuum phase respectively.

1.6 Significance of the research project

The research project has been designed to provide numerical modelling techniques for improving the understanding, knowledge and ultimately performance of adhesively bonded composite pipe sections.

1. To author's knowledge, the available technical literature on adhesively bonded composite pipes is mute on large diameter pipe joints. An attempt has been made in this research project to study adhesively bonded composite pipe sections for a range of inside pipe diameters. Solutions from the numerical model being formulated in this project indicate that the region susceptible to failure shifts as a function of inside pipe diameter. The proposed numerical model thus aids in the development of composite piping structures and enables a broader range of practical applications.

2. Based on insights gained in Phase I of this project, reinforcement of the polymer materials employed in the joint region is desirable. Nanoplatelet nanocomposites based on graphene were considered herein for this purpose. A finite element based atomistic approach was proposed to characterize the mechanical properties of graphene sheets. The proposed modelling approach is less computational intensive as compared to conventional numerical techniques (e.g. molecular dynamics, Monte Carlo simulation etc.) as fewer degrees of freedom are involved in the analysis. The proposed numerical

modelling technique makes it possible to incorporate discrete graphene sheets in the simulation without causing undue computational cost.

3. A novel multiscale modelling technique was proposed herein to characterize mechanical properties of graphene/polymer nanocomposites, as well as to explore the underlying strengthening mechanism for such advanced materials. The two-dimensional configuration of graphene poses considerable challenges for the experimental characterization of graphene nanocomposites. The proposed multiscale modelling approach employing the finite element method is capable of exploring the mechanical properties of graphene/polymer nanocomposites at very reasonable computational efforts. The multiscale model enables numerical solutions for the study and mitigation of damage in joint regions susceptible to failure as identified in the first phase of the research project.

Overall, novel numerical techniques were developed and employed in the present research project that not only aid in improving joint characteristics of large diameter composite piping but may also be useful for other polymer-based structures.

1.7 Bibliography

1. compositecenter.org (July 30th,**2012**)
2. http://www.etamax.com.au/filament_winding.html (September 21, **2012**)
3. F.Hussain, M.Hojjati, M.Okamoto, R.E.Gorga, *Review article: polymer matrix nanocomposites, processing, manufacturing, and application: an overview*. J. Compos. Mater. 40 (**2006**) 1511-1575.
4. J.J.Luo, I.M.Daniel, *Characterization and modelling of mechanical behaviour of polymer/clay nanocomposites*. Compos. Sci. Technol. 63(**2003**) 1607-1616.

5. M.Meyyappan, *Carbon nanotubes, science and application*, CRC Press **2006**.
6. M.Alexandre, P.Dubois. *Polymer layered silicate nanocomposites: preparation properties and uses of a new class of materials*. Mater. Sci. Eng.Rep. 28 (**2000**) 1-63.
7. E.P.Giannelis, *Polymer Layered Silicates Nanocomposites*, Adv. Mater. 8 (**1996**) 29–35.
8. R.M.Reilly, *Carbon nanotubes: potential benefits and risks of nanotechnology in nuclear medicine*. J. Nucl. Med. 48 (**2007**) 1039-1042
9. C.Bower, R.Rosen, L.Jin, J.Han, O.Zhou, *Deformation of carbon nanotubes in nanotube polymer composites*. Appl.Phy. Lett. 74 (**1999**) 3317-3319.
10. C.A. Cooper, D.Rayich, D. Lips, J. Mayer, H.D. Wagner, *Distribution and alignment of carbon nanotubes and nanofibrils in a polymer matrix*. Compos.Sci.Technol. 62 (**2002**) 1105-1112.
11. R.Haggenmueller, H.H.Gommans, A. G.Rinzler, J. E. Fischer, K.I.Winey, *Aligned single wall carbon nanotubes in composites by melt processing methods*, chemical. Phy. Le. 330 (**2000**) 219-225.
12. M.A.Scott, K.A.Carrado, P.K.Dutta, *Handbook of layered materials*, Taylor ad Francis, **2004**.
13. Y.X.Pan, Z.Yu, Y.Ou, G.Hu, *A new process of fabricating electrically conducting nylon 6/graphite nanocomposites via intercalation polymerization*. J.Polym. Sci. part B. 38 (**2000**) 1626-1633.

Phase I(Macroscopic analysis)

The scope of Phase I of this research study is as follows:

- Review the current state of art for adhesively bonded FRP pipe sections
- Conduct dimensional scaling of adhesively bonded FRP pipe sections
- Investigate the effect of fibre architecture on the performance of adhesively bonded FRP pipe sections

Work as part of Phase I has previously been presented in the form of peer reviewed journal publications:

Avinash Parashar and Pierre Mertiny, *Adhesively bonded composite tubular joints: Review*. Int.J.Adhes.Adhes. **2012**, 38: 58-68.

Avinash Parashar and Pierre Mertiny, *Effect of FRP pipe scaling on its adhesive bonding strength*. J.Adhes.**2012**, 88: 866-880.

Avinash Parashar and Pierre Mertiny, *Failure mechanism in adhesively bonded FRP pipe sections with different fibre architecture*. Composite Part B. **2012**, (d.o.i – 10.1016/ j.compositesb.2012.10.041).

Chapter 2

Adhesive Bonding of FRP Pipes: Review[1]

2.1 Introduction

Fibre reinforced polymer (FRP)/composite materials have many inherent qualities, including high specific stiffness and strength. These special properties make composites an ideal candidate for replacing metallic piping structures in industries such as chemical, petrochemical, and energy. Composite structures are being intensively studied as replacements for metallic structures, as metallic structures are considered more prone to corrosion and wear in harsh environments.

The complex layout of industrial piping systems, along with limitations associated with composite pipe manufacturing, demands repeatable and durable joining mechanisms. It is a known fact that joints are the weakest links of such composite structures. Composite pipe joints can be accomplished either mechanically or adhesively. Mechanical joints are associated with trimming, bolting, and fastening, which result in localized stress concentration in the structure and often weaken the joint as well as the whole structure. Drawbacks associated with the mechanical joining of composite tubes divert the research towards adhesive bonding of tubular sections.

Adhesive bonding of FRP structures was studied by a number of researchers [1–4]. With advancements in filament winding technology, ongoing efforts are also being made to study the adhesive bonding of tubular structures [5–9]. Lubkin and Reissner [10] may be considered among the pioneer researchers in the field of adhesively bonded tubular joints. They experimentally investigated the stresses developed in an adhesive joint, which were further validated with the finite

---

[1] A version of this chapter has been published asA. Parashar and P. Mertiny. **2012** *Int.J.Adhes.Adhes.*38:58-68.

element model developed by Adams and Peppiatt [5]. The first theoretical analysis of the tubular single lap joint was performed by Volkersen [11] and further modified by Adams and Peppiatt [5]. The numerical expression proposed by Adams and Peppiatt for shear stress in the adhesive bondline subjected to torsion loading *T* is given in Equation 2.1, and an illustration is provided in Fig.2.1.

$$\tau_a = \frac{T\alpha}{2\pi a^2}\left[\frac{1-\varphi\left(1-cosh(\alpha L)\right)}{sinh(\alpha L)}\right] cosh(\alpha z) - \varphi sinh(\alpha z) \qquad (2.1)$$

where

$$\delta = \frac{2\pi r_{1o} G_a a^2}{G_1 J_1 \eta}$$

$$\varphi = \frac{G_2 J_2 r_{1o}}{G_1 J_1 r_{2i} + G_2 J_2 r_{1o}}$$

$$\alpha = \left(\frac{\delta}{\varphi}\right)^{0.5}$$

In the preceding equations, $r_{1o}$and r_{2i} are the outer and inner radius of the cylinder and tube adherend, respectively; a is the average radius of the adhesive; J_1 and J_2 are correspondingly the polar moment of inertia for cylinder and tube adherend; G_1 and $G_2$are the shear moduli of the cylinder and tube adherend, respectively; and G_a, and $\eta$are respectively the shear modulus and thickness of the adhesive.

On practical grounds, their theory was bounded by the concept of thin-wall structures and the Goland and Reissner [12] criteria. According to these criteria [12], normal and shear stresses in the adherend can be neglected if values of constant 'β' satisfy the condition given in Equation 2.2 below:

$$\beta = \frac{\eta \times E}{E_a \times t} \simeq \frac{\eta \times G}{G_a \times t} \geq 10 \tag{2.2}$$

In Equation 2.2, η is thickness of adhesive layer; E_a and G_a are correspondingly the Young's and shear modulus of the adhesive; E,G and t are the Young's and shear modulus and wall thickness of the tubular section respectively.

In accordance with the Goland and Reissner criteria [12], the results of Lubkin and Reissner [10] were formulated around the assumption that shear and peel stresses in the tubular subsections can be neglected when compared with the same stresses in the adhesive layer.

In the research work of Alwar and Nagaraja [13], visco-elastic behaviour of the adhesive material was incorporated in a finite element analysis of the joint, subjected to different loading conditions. It was reported in their conclusions that the viscoelastic behaviour of the adhesive helps to reduce the maximum stresses at the edge of the joint. Some researchers have also provided closed-form solutions for mapping stress distribution within adhesively bonded joints. One such solution was provided by Volkersen [11] for a tubular joint subjected to torsional loads; another was provided by Terekhova and Skoryi [14] for a joint subjected to internal and external pressure.

In 2010, Xu and Guoqiang [15] established that stress components along the thickness of the adhesive layer are not constant. These results were contrary to earlier established assumptions of constant stress values along the thickness of the adhesive layer. Xu and Guoqiang [15] used a finite difference method to calculate six stress components in the adhesive layer [15]. The effects of fibre orientation, composite laminate stacking sequence, overlap length, and adhesive layer thickness on shear and peel stresses developed in the adhesive layer were also studied in the same research work.

2.2 Classification of adhesively bonded tubular joints

2.2.1 Lap joints

Adhesive bonding provides a convenient method for assembling structures such as composite laminates and tubes. The typical and conventionally used joining technique for tubular structures is the lap joint. Applications of such lap joints include bonding a metal and fitting to a composite tube in space structures and automotive drive shafts.

Composite shafts are becoming common these days due to ease of manufacturing and low rotational inertia at a relatively high stiffness compared with similar metallic shafts. Torque transmission capabilities of adhesively bonded composite shafts or tubular sections are the focus of many research works [16–19]. The experimental work of Choi et al. [18] on single lap composite joints was further extended to cover adhesively bonded tubular sections [20]. In that research work [20], the effect of adhesive thickness was studied with respect to the torque transmission capacity of the single lap tubular joint. For the purpose of modelling, the adhesive was divided into three regions as shown in Fig.2.1.

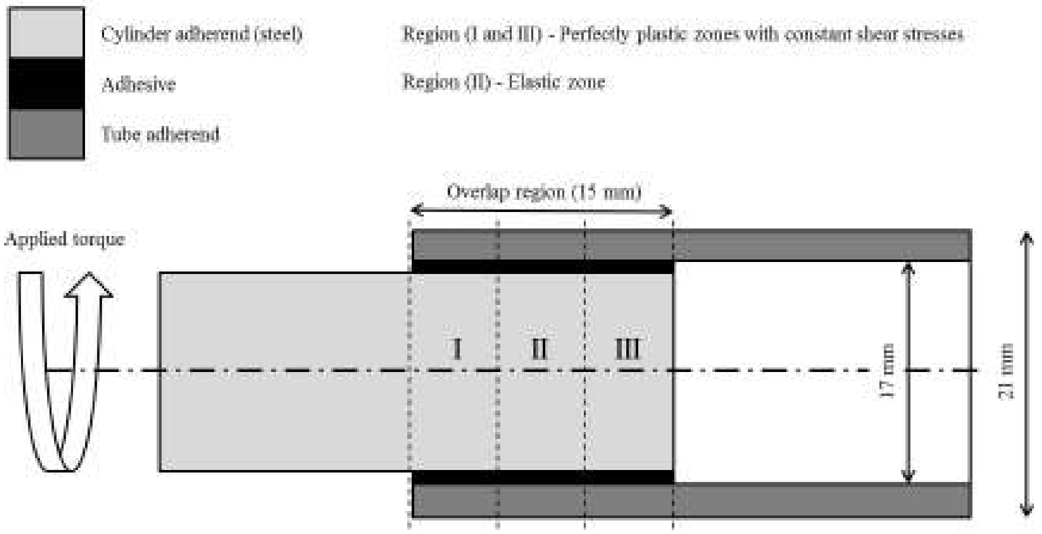

Fig.2.1 Schematic of joint subjected to torsional loading by Choi and Lee [20].

In the work by Choi and Lee [20] the effects of adhesive thickness and thermal residual stresses on the torque transmission capacity of single lap tubular joints were investigated, using epoxy-based adhesive. Elastic properties were assumed for the adhesive when deriving closed form solutions, whereas elastic perfectly plastic behaviour for the adhesive was assumed in the numerical-based solution for investigating the effect of adhesive thickness on the torsional capacity of the joint. It was considered in the research work that the adhesive failed under fracture when the maximum shear strain reached its ultimate value. Contrasting trends for the torsional capacity of the adhesively bonded joint were reported in the work of Choi and Lee when the behaviour of adhesive material was modelled as elastic perfectly plastic instead of elastic. It was concluded in their work that the torsional capacity of the joint decreased linearly with respect to adhesive thickness, when adhesive properties were modelled as elastic perfectly plastic material behaviour, which was opposite to the trend obtained with elastic properties for the adhesive. A linear increase in torsional capacity with elastic properties was attributed to the mitigation of stress concentration at the end of the adhesive with increased thickness. Later on, these closed-form and numerical results were compared with those obtained from experimental work. It was finally concluded that the experimental findings were in close agreement with the numerical results, which further emphasised the behaviour of adhesive as elastic perfectly plastic instead of elastic.

Kim and Lee [21] employed a 3-D finite element model to study the effect of shaft fibre architecture on its torque transmission capacity. They modelled composite shafts with three different stacking sequences of $[\pm 15°]_{nT}$, $[\pm 30°]_{nT}$ and $[\pm 45°]_{nT}$. Filament winding angle of $[\pm 15°]_{nT}$ was recommended to increase the natural frequency of the composite shaft, whereas $[\pm 45°]_{nT}$ was considered for improved torque transmission capacity. The authors reported that composite shaft joints with $[\pm 15°]_{nT}$ and $[\pm 30°]_{nT}$ failed within the composite adherend, whereas in those with the fibre architecture of $[\pm 45°]_{nT}$, failure shifted towards the adhesive bondline.

In addition to torsional loading, efforts were also made to study single lap joints under axial loading [6, 22]. Guess et al. [23] performed experimental as well as numerical investigations of single lap metal to composite pipe joints under axial tension, compression, and flexure loading. They considered two different sets of materials in their research: weave E-glass fabric/epoxy to aluminium and tri-axially reinforced E-glass/polyester to steel. Furthermore, their study also considered the effect of tapered/un-tapered geometry of metallic pipe sections as shown in Fig.2.2. They reported that the primary failure mode was adhesive de-bonding at the inner bond end of the joint. The failure was reported in the region with highest peel stresses under the influence of tensile and compressive loading. The axial compression strength of the metal to composite joint was reported significantly lower than the tensile strength; the only exceptions were the tapered aluminium pipe sections. However, no significant improvement in the joint strength under compressive loading was observed when aluminium was replaced with a steel adherend, even with a tapered end component.

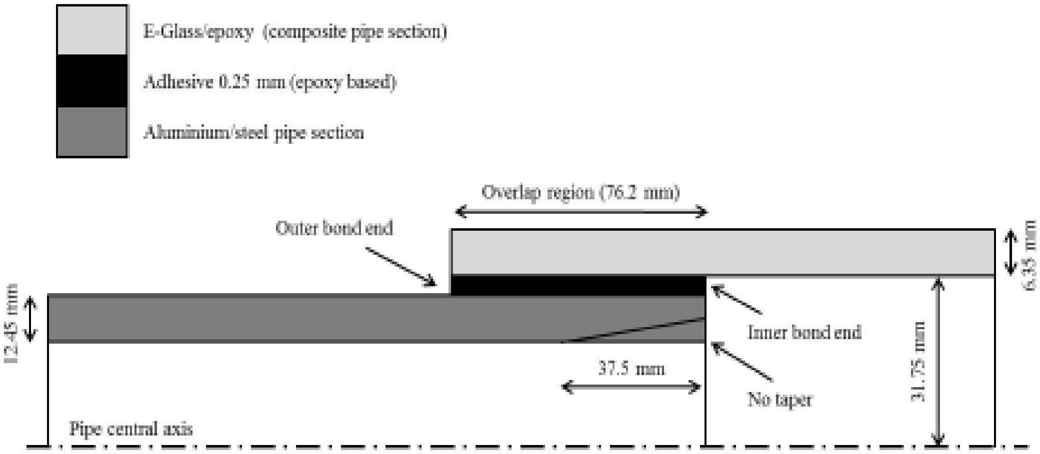

Fig.2.2 *Schematic of single lap metal to composite tubular joint [23].*

So far, this review on single lap tubular joints has focused on material strength criteria. Significant contributions have also been made with respect to a fracture mechanics approach. The problem of delamination in composite structures is very common, and Bolotin [24] summarized a comprehensive review on this topic. Considering the influence of delamination on the bonding strength of adhesively bonded components, Qin and Dzenis [25] were the first to explore delamination in adhesively bonded joints. Panigrahi and Pradhan [26] studied the effect of delamination on adhesively bonded composite pipes, simulating the problem as composite laminate plates. Taheri et al. [27] used the research work of Panigrahi and Pradhan [26] to validate their proposed numerical model. Taheri and his team employed a finite element environment to investigate delamination in adhesively bonded aluminium and composite pipe sections as shown in Fig.2.3. A parametric finite element study was performed to study the effect of geometrical and loading parameters on the peel and shear stresses developed inside the adhesive layer. For the numerical simulation, aluminium pipe was modelled with an inside radius of 16.95 mm and a wall thickness of 2 mm, while the composite counterpart was modelled with an outside radius of 16.80 mm and similar wall thickness. The thickness of the adhesive layer in each model was kept at 0.15 mm.

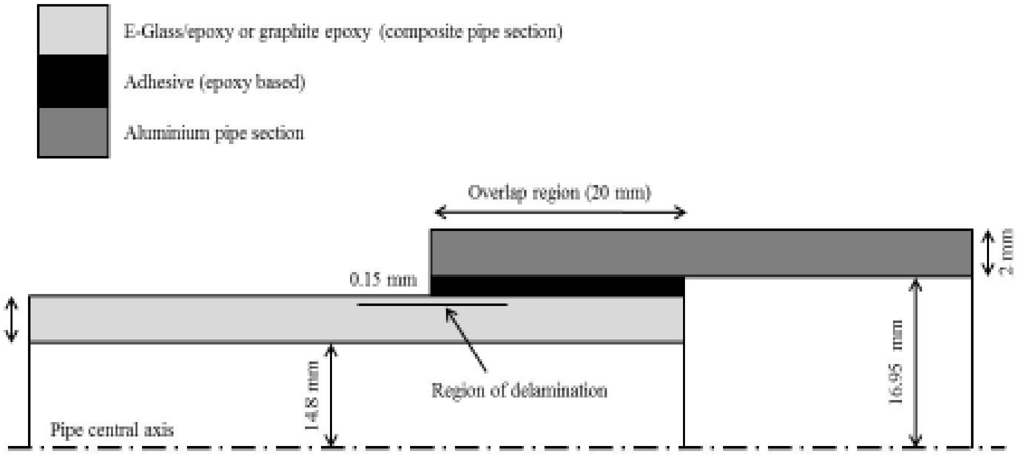

Fig.2.3 *Simple cross-sectional view of adhesive joint to study delamination [27].*

In the discussed research, the maximum peel and shear stresses within the adhesive layer were considered to be important characterizing parameters for adhesively bonded joints. Pre-existing in-plane delamination between different laminas of composite pipe was also considered in the study. The effect of delamination on joint strength with respect to the position of delamination in composite pipe was investigated, and it was reported that the position of delamination, overlapping the edge of the joint as shown in Fig.2.3, had a more significant effect on the peel and shear stresses in the adhesive layer in comparison with the position of delamination, either lying fully in the overlapped region or fully outside the overlapped region. The depth of delamination along the composite pipe thickness was also studied in that paper, and it was concluded that delamination at shallower depth from the pipe surface had the least effect on peel and shear stresses in the adhesive layer. Two different composites were modelled, one a glass/epoxy composite and the other a stiffer combination of graphite/epoxy. It was reported that stress distribution within the adhesive layer was similar for both composites, but values of stresses changed significantly.

Recently, in the research work of Das and Pradhan [28], material strength as well as a fracture mechanics approach was employed to study the effect of fibre architecture on the failure characteristics of an adhesive joint. A parametric study was performed in a finite element environment to optimise the stacking sequence of a composite based adherend (graphite/epoxy). Initially, a material strength based approach was used to estimate the region responsible for initiating the failure, and subsequently a fracture-based approach was used to optimise the configuration. It was finally concluded that composite adherends with angle ply laminates favour mode I failure in the adhesive, whereas $[45/-45]_{4S}$ and $[30/60]_{4S}$laminates are more prone to mode II failure.

Besides the fracture mechanics approach, researchers also used more realistic approaches to analyze polymeric composite materials. Induced plastic strain in most polymeric materials even at low loads makes it unrealistic to assume polymeric adhesive material as linear. In the early 1990s, Thomsen described how with linear property assumptions only information such as stress distribution and displacements could be obtained about the adhesives [29]. His research was considered as an extension of the earlier work of Gali [30, 31] and Dolev [32]. Thomsen implemented the theory of orthotropic laminated shells developed by Keller for nonlinear analysis of adhesive joints [33].

Thus far, the review of adhesive joints in this section has been limited to the non-linear behaviour of polymeric adhesives. Recently, attempts have also been made to also consider non-linearity in the adherent, and it was mentioned by Hosseinzadeh and Taheri [34] that the effect of non-linearity could be significant if both adhesive and adherent show non-linear behaviour with respect to material properties. The above case is common when polymer based piping, such as FRP pipes, are joined with polymeric adhesive, such as epoxy. Optimization of coupler configurations with respect to nonlinear property considerations has been accomplished in a few research publications [34–36].

2.2.2 Prepreg joints

Single lap joints, discussed in the preceding sections, were designed mostly to connect metal with composite adherends. In the late 1990s, Huysmans et al. [37] introduced prepreg technology for the bonding of two composite pipe sections. Prepreg technology may be considered as the initial step towards minimising the efforts involved in adhesive bonding of composite pipes (hand layup). However, there was still some manual work involved in prepreg technology in wrapping prepreg tape around the aligned pipe extremities. Besides a moderate amount of manual work, the prepreg-based joining technique required a long curing time, which possibly increase further with the thickness of the prepreg coupler.

When compared with hand layup methods that were commonly used for joining composite pipes, prepreg technology was claimed to be more field friendly. The prepreg-based joining concept is illustrated in a simplified sketch in Fig.2.4.

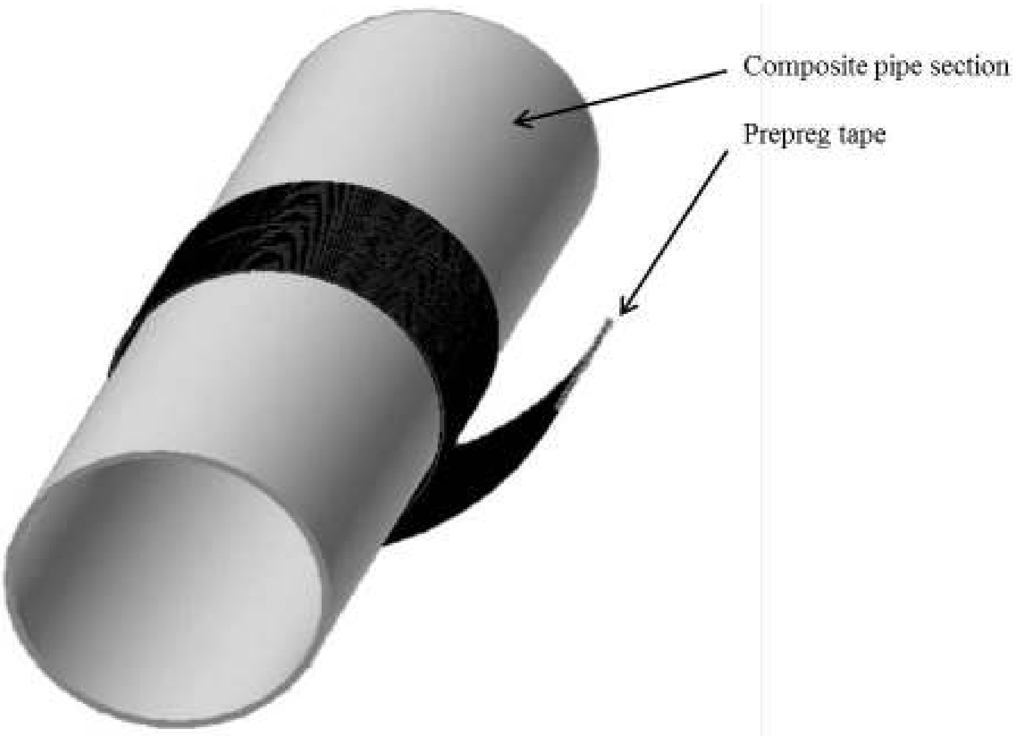

Fig.2.4 *Prepreg wrapping technique around pipe extremities [37].*

In the prepreg-based technology, non-crimp glass fabric impregnated with epoxy was considered for the manufacturing of the prepreg tapes. It was mentioned in the research work of Huysmans et al. [37] that the prepreg material and its chemical combination were selected so that a long shelf life could be obtained. The author of the papers [37, 38] performed mechanical and thermo-mechanical tests on cured resin to optimise the curing temperature and process time with respect to resin toughness and mechanical properties of the prepreg coupler. An optimal cure temperature was finally proposed to cure the resin of the prepreg coupler. Then, Huysmans and his research team optimised the reinforcement material with respect to fibre orientation or stacking sequence. Classical laminate theory was employed for optimising the geometry and stacking sequence of fibre in the prepreg coupler. Four different stacking sequences of [±45°], [0°/±45°], [0°/±90°], and [45°/90°/-45°/0°] were considered during the optimisation of fibre architecture for the prepreg coupler. Bi-material interface fracture toughness under mode I and mode II was employed by Huysmans et al. [38] for optimising the fibre stacking in the prepreg coupler. Finally, it was concluded that the pipe/coupler interface with [±45º] stacking next to the pipe surface had the maximum fracture toughness under mode I loading. It was also mentioned that with [±45°] stacking next to the pipe surface, failure shifts to the prepreg coupler, whereas with the other stacking sequences, interfacial failure was observed. The work on the prepreg coupler was further extended to study the structural strength of the joint using a fracture mechanics approach.

In the prepreg-based bonding of tubular joints, delamination between the pipe and prepreg coupler interface was considered to be the most dominant cause of failure. A fracture mechanics approach was employed in the papers [38, 39] to study and optimise the prepreg coupler and joint configuration. In these papers, delamination at the interface of pipe and coupler as well as pipe and filler material (epoxy) was used to optimise the coupler dimensional parameters.

Wahab and Roeck [39] considered two separate artificial cracks in their finite element model to study the fracture strength of the prepreg joint shown in Fig.2.5.

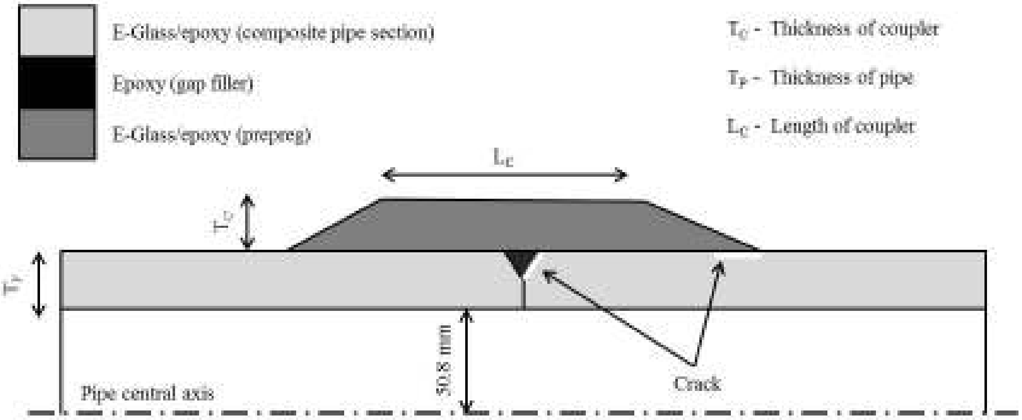

Fig.2.5 *Cross- sectional view of model employed by Wahab and Roeck [39]*

Crack growth under opening mode (mode I) was considered a dominant cause of failure, as strain energy under tearing (mode III) constituted only 1% of mode I strain energy release rate. In this work, SERR values under mode I were employed to optimise the prepreg stacking sequence, joint length (L), prepreg thickness (Tc), and angle of taper.

2.2.3 Filament wound sleeve couplers

Prepreg technology developed for the joining of composite pipe sections has limited potential for automation. Processing prepreg joints requires special equipment and/or long curing times. The latter was considered to be one of the major drawbacks associated with prepreg joining technology, which also limits the field applicability of the technology. To overcome some of these drawbacks and to introduce automation in adhesive bonding of pipe sections, Mertiny and Ellyin [40] introduced a new concept for adhesive bonding of composite pipe sections. In the proposed technique they replaced the prepreg couplers with filament wound sleeve couplers. The sleeve coupler, shown in Figs.2.6 and 2.7, was pre-manufactured with filament winding, which made the whole joining process simpler and semi-automatic in nature. It was claimed that the efforts required for prepreg technology and also the handling difficulties associated with scarf joints could be addressed with the proposed technology of pre-manufactured sleeve couplers.

The filament wound overlapping sleeve coupler was used in conjunction with a unique adhesive injection technique. The simplicity of this technique has made it more industry friendly; hence, it may be used in the field for joining composite pipes. It is claimed in [40] that the design of the sleeve coupler also enhances the contact surface area between the coupler and pipe sections, which makes the load transfer smoother and aids in mitigating stress singularities within the adhesive joint.

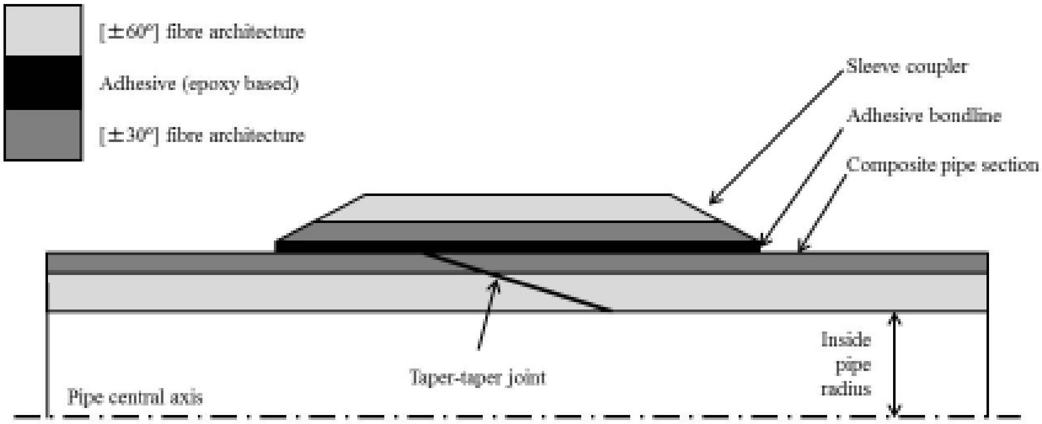

Fig.2.6 *Schematic of filament wound overlap sleeve coupler joint configuration [40].*

The fibre architecture for the overlap sleeve coupler was derived from research on multi-angle filament wound tubular structures [41, 42]. In the experimental work on these structures, four different stacking sequences were considered: $[\pm 60_n^\circ]_T$, $[\pm 45^\circ,\pm 60_n^\circ]_T$, $[\pm 60^\circ,\pm 45_n^\circ]_T$, and $[\pm 30^\circ,\pm 60_n^\circ]_T$. These stacking sequences were experimentally tested for hoop, axial, and multi-axial loadings. Finally, a[±60°] layup was found to be best under pure hoop loading, whereas the $[\pm 30^\circ, \pm 60_n^\circ]_T$ stacking sequence was reported to have the best strength under the multi-axial loading. Keeping these results in mind, Mertiny and his research team employed the stacking of $[\pm 30^\circ, \pm 60_n^\circ]_T$ for the manufacture of overlapped sleeve coupler and pipe as shown in Fig.2.6. In the proposed joint configuration, [±30°] stacking was kept next to the adhesive bondline in the pipe as well as in the coupler. Laminas with stacking of [±30°] were responsible for providing axial strength along the pipe axis, whereas [±60°] laminas provided hoop strength.

Semi-automatic fixture (alignment device) as shown in Fig.2.7 was deployed to align the pipe extremities. Later on, filament wound sleeve couplers were tested for their strength under static as well as dynamic loads with FRP pipes of inside diameter of 50mm and 100mm respectively [40, 43]. Functional and structural failures were reported in these research papers, when the joint with overlapped sleeve coupler was tested under multi-axial loading with different hoop to axial stress ratios. Functional failure was defined as weeping of inside fluid during the load test, while the structure was still considered good enough to sustain the applied load, whereas in structural failure, the joint collapsed and could not take any further load.

It was reported in the experimental testing of the joint with multi-axial loading [40] that hoop stress produced with the internal pipe pressurisation had a reinforcing effect on the adhesive joint, whereas axial loading was considered detrimental to the adhesive joint. Mertiny and Ellyin [40] further employed finite element codes to optimise the overlap length, adhesive thickness, and stacking sequence of the filament wound sleeve coupler. Adhesively bonded tubular sections with overlapped sleeve coupler were further tested under dynamic loading, and it was finally concluded from the experimental and theoretical analysis that tensile loading was the main cause of joint failure. De-bonding of sleeve coupler and matrix cracking in pipe sections were the reasons behind the degradation of pipe assembly under dynamic loading [43].

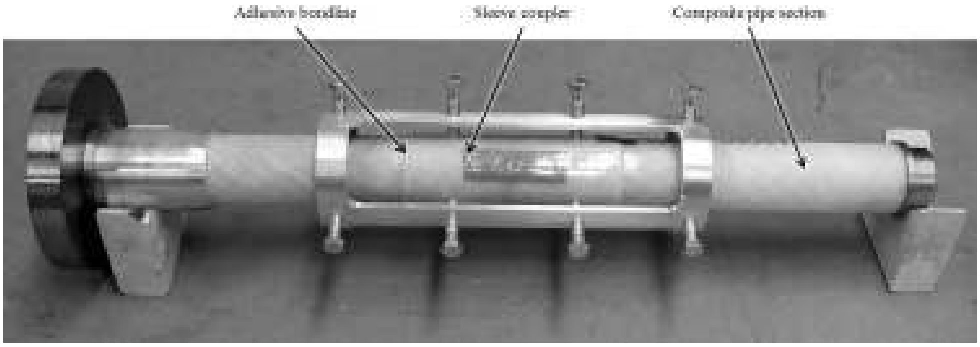

Fig.2.7 *Aligning device with composite pipe sections and sleeve coupler [40].*

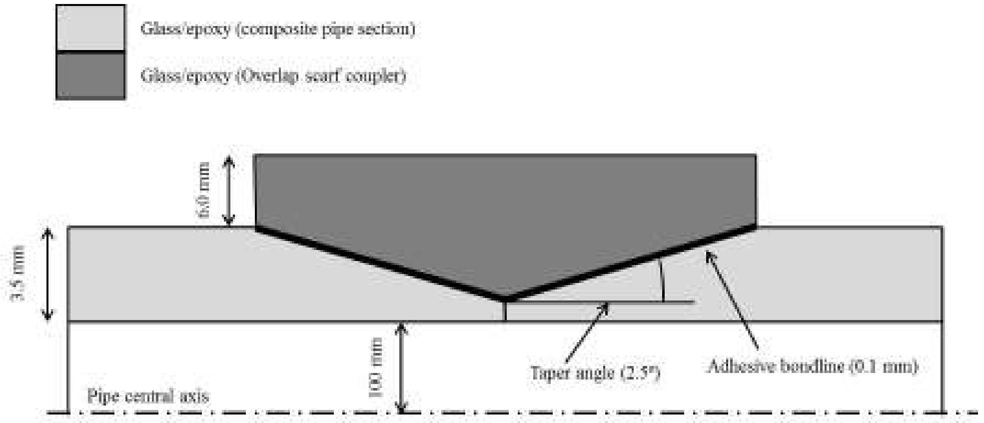

Fig.2.8 *Schematic of taper/taper joint configuration proposed by Hashim et al. [44].*

2.2.4 Scarf joint

Thus far, the discussion has been focused on the optimising of manufacturing techniques for an overlapping coupler. Designing the adhesive joint for higher load bearing capacity is another aspect covered by many researchers to improve the quality of the adhesive joint. In the late 1990s, Hashim et al. [44] attempted to optimise the design configuration of adhesively bonded tubular joints. They proposed a taper/taper configuration of the coupler and adjoining pipe sections as shown in Fig.2.8 for improved joint characteristics. In the adhesive joint design shown in Fig.2.8, the adhesive bondline was kept fixed at 0.1 mm, and the taper of the pipe extremities to fit the coupler taper was kept at 2.5°. The researchers claimed that the proposed taper end for pipe extremities and coupler achieved a good joint fit, a thin adhesive layer, and improved joint handling capability.

Researchers tested the scarf joint configuration for its short as well as long-term integrity. It was a well-known fact that the long-term behaviour of adhesive joints was significantly affected by environmental conditions such as humidity and water, and such facts were considered while testing the scarf joint integrity. Poor adhesion at the glass reinforced epoxy (GRE) pipe surface was the main defect against which the joint was designed and tested. Four different load conditions were employed for testing the joint configuration: tension, tension with internal pressure, bending, and bending with internal pressure. Knox and his research team employed experimental as well as finite element techniques to study the proposed joint integrity [45]. During the experimental work, axis symmetric de-bonding at the surface of the pipe was produced in the joint configuration with the help of poly-tetra fluoroethylene (PTFE) spray. During most of the experimental work, failure was reported either in the adhesive bondline or in the composite adherend. Scarf joint configuration was further tested for short as well as long-term joint performance.

Short term: During the short term, the joint was subjected to tension or tension with internal pressure. A different percentage of de-bonding was created in the adhesive joint prior to the start of experiments. It was reported in [45] that a de-bonding percentage above 30% between the pipe and the adhesive bondline would shift the region of failure from the composite pipe to the adhesive bondline. However, it was also reported in the same work that while testing the joint with bending, the de-bond percentage was reduced to 17%, shifting the region of failure from the GRE pipe to the adhesive bondline. On the other hand, in tests performed with bending along with internal pressure, de-bonding of 10% was found sufficient to shift the failure.

Long term: For long-term integrity, the joint was tested against creep deformation with different sets of temperature and percentages of axis-symmetric defects. Extensive work on the creep behaviour of polymer composites has already been published by a number of researchers [46–49]. The visco-elastic behaviour of polymer composites at higher temperatures compelled Knox and his research team to study the creep behaviour of scarf joints [50]. Findley's empirical model

(Equation 2.3) for characterising the non-linear creep behaviour of polymer materials was also employed in the study of scarf joints [51].

$$\varepsilon(t) = \epsilon_o + mt^n \tag{2.3}$$

In Equation 2.3, $\varepsilon(t)$ and ε_0 are strain at time t and strain values independent of time, respectively, m is the coefficient of the time-dependent term, and n is a constant which is independent of stress values. It was reported in the research that creep deformation of a scarf joint behaved as a function of temperature and axis-symmetric defects. At an experimental temperature of 65ºC, no creep deformation was observed, but significant creep deformation was reported at higher temperatures such as 95ºC.

Knox and his research team [52] further tested the scarf configuration for dynamic loads. Joints showed a high level of integrity with bending load at ambient temperatures, even with a high percentage of axis-symmetric defects. However, the joint strength decreased significantly at high temperatures. A similar observation was made with tensile loading of the joint geometry. It was experimentally observed that failure resided in the GRE pipe section for perfect joint specimens, whereas failure shifted into the adhesive bondline for specimens containing axis-symmetric defects.

2.2.5 Hybrid joint

The butt weld hand layup technique used for joining composite pipes normally results in a high-strength joint configuration. However, a high curing time with the hand layup technique lowers the joining efficiency. Attempts were made by Stabblefield et al. [53] and Mensah et al. [54] to increase the joining efficiency of prepreg butt weld composite pipe joints.

Compared to the wet layup technique, prepreg welding significantly reduces the coupling time of the pipe extremities. It was reported in the work of Guoqiang et al. [55] that butt weld composite pipe joints have the potential to provide the composite market with a user-friendly, portable, and cost effective process for onsite joining. However, it was also reported that the internal pressure rating was not good enough to satisfy the industrial requirement of at least 2.07 MPa for composite pipes.

Thus far, the joint technologies reviewed use either prepreg or adhesive material to bond adjoining pipe sections. In 2003, Guoqiang et al. [55] introduced the concept of hybrid joints. Hybrid technology incorporates both prepreg and adhesives for bonding composite pipes. It has been reported in the research work that with butt joints, there remains a gap at the bondline between the two pipe extremities. This gap enlarges as the internal pressure of the pipe increases. Stress singularities normally develop in between the butt ends of the two pipe extremities, due to the crack-like gap between the pipe ends. These stress singularities are driven by axial stresses in the pipe as well as by the pressurised fluid in the gap. Developed stress singularities considerably weaken the adhesive joint strength. Configuration of the hybrid joint with a prepreg coupler and adhesive in between the butt ends of the pipe extremities is shown in Fig.2.9.

It was claimed by the researchers in their work [55] that in the hybrid technique the load was shared between the prepreg coupler and the adhesive layer, whereas in all other joining techniques the load was transferred either through the prepreg coupler or through the adhesive bondline.

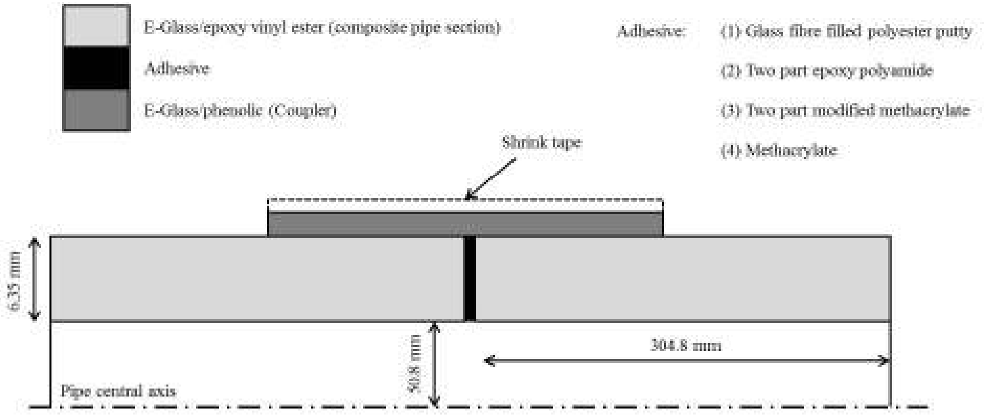

Fig.2.9 *Schematic of hybrid joint [55].*

2.3 Trends in improving the adhesive joints

2.3.1 Improved curing techniques

The prepreg technique for joining composite pipes was further improved by introducing heat-activated devices to reduce curing time and to enhance the strength of the adhesive joint [56–57]. The original idea behind heat-activated joining was to improve the joining efficiency of the butt weld joint.

Stubblefield et al. [53] made a significant contribution in improving the curing technology for prepreg joints by replacing the catalyst and promoter with a heating device. They briefly discussed the importance of the temperature for obtaining the optimum strength of the adhesive joint and concluded that low curing temperatures normally left the resin under-cured, whereas high temperatures led to hardening of the resin. To obtain optimum strength from the adhesive joint, they introduced heating device technology in [53].

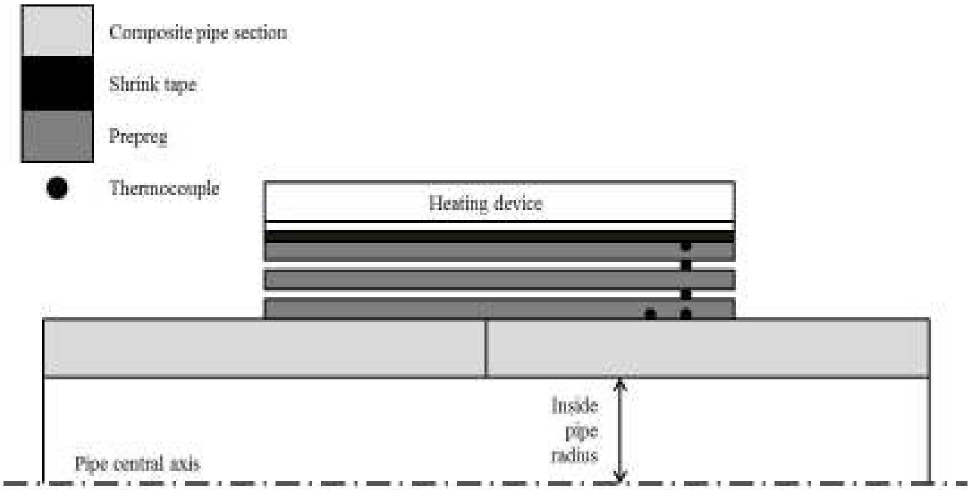

Fig.2.10 *Schematic of heating device technology developed by Stubblefield et al. [53].*

In the heating device technology introduced by Stubblefield and his research team [53], embedded thermocouples are used in conjunction with closed-loop temperature control devices as shown in Fig.2.10. Temperature history is maintained with the help of embedded thermo-couples, which helps in obtaining the optimum cure cycle. Shrink tape on the top of prepreg tape is employed to obtain uniform pressure during the curing cycle, which helps to reduce the thermal contact resistance and to squeeze out excess resin. The performance of the cured joint with the aid of a heating device was later evaluated with the help of hydro and three-points bending tests.

2.3.2 Ultraviolet-assisted curing

The heating technique developed to improve the curing of adhesive joints was later considered to be a cumbersome technology, as it required continuous power supply for hours, which made it difficult to implement for onsite applications. To replace the heat-activated curing technique, Pang et al. [58] proposed a new field-level curing method based on ultraviolet (UV) heating. UV-cured resins are common in the field of dentistry, and the impact of UV intensity on cure has already been studied by many researchers [59–65].

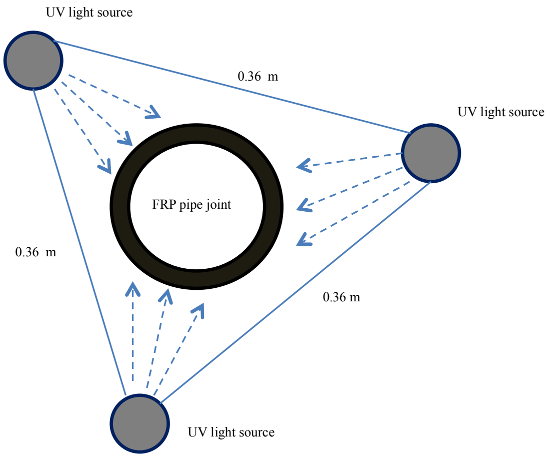

Fig.2.11 *Schematic of the arrangement for the UV curing of an adhesive joint [66].*

UV curing of resin takes place through photo polymerisation by free radicals. Photo inhibitors are added to the resin and adhesive promoters to initiate polymerisation with the help of UV radiation. The free radicals produced by excited molecules help in initiating polymerisation of the monomers and oligomers. A schematic of the UV curing process employed by Peck et al. [65] is shown in Fig.2.11, where three fixtures consisting of six 160 W UV fluorescent lamps were aligned vertically. The resulting irradiance on the centre of the joint was calculated with the help of the inverse square law.

Considering the fact that composite pipes and tubes are extensively used in truss or frame structures, Peck et al. [65] tested the UV-cured joints for their bending strength. Testing proved that reduced curing time with UV-assisted curing did not have any impact on the bending stiffness of the joint. They also tested the joint for its pressure rating and reported that the internal pressure rating of a UV-cured joint was reduced to 3.28 MPa, compared with an ambient-cured joint with a pressure rating of 8.27 MPa. This signifies that UV-cured joints cannot be used for carrying liquid and gases under pressure. A high interfacial stress concentration at the interface of cured and uncured FRP sections was cited as the major reason for the low pressure rating of UV-cured joints.

Jerry et al. [66] studied the reasons cited in the work of Peck et al. [65] for the low pressure rating. In their work on UV-cured joints, they studied the effect of joint thickness with three different sets of models, consisting of 3, 5, and 8 layers along the pipe thickness. They reported that the pressure rating of the joint with the highest thickness (8 layers) was the worst, whereas the joint consisting of 5 layers was found to have the highest pressure rating of the three thickness models. They concluded that the low pressure rating of the UV-cured joint with the highest thickness was due to uncured resin left in the joint structure, whereas the low pressure rating of the joint consisting of 3 layers was due to less reinforcement. They also reported that the bending stiffness of the UV-cured joints was independent of the joint thickness. It was also established experimentally that an optimum thickness of adhesive was required for UV-cured joints [66, 67].

2.3.3 Smart material (piezoelectric) in adhesive joints

The adhesive bondline between the coupler and the composite pipe plays a significant role in transferring stresses via peel and shear stresses. Due to the transition of load from the pipe to the coupler, end regions of the adhesive bondline always remain under a significant amount of stress, which ultimately results in the failure of the adhesive assembly [68–70]. The stress singularities at the edges of the adhesive bondline establish it as the weakest link of the whole assembly. Efforts have been made by researchers to mitigate the stress singularities in the adhesive bondline either by modifying the edge geometry or mechanically reinforcing the edges [71–73].

It was proposed by Cheng et al. [74–75] that stress singularities developed at the adhesive bondline were significantly reduced by blending piezoelectric material with the composites. The application of smart material in the field of structural engineering is now considered to be in its mature state. Already, a lot of research work has been reported on smart material with similar applications in engineering [76–85]. Configuration of the adhesive joint with a reinforced layer of piezoelectric material is demonstrated with a simple sketch in Fig.2.12.

Cheng et al. [74, 75, 86] proposed that stress singularities in the adhesive bondline could be reduced significantly with the use of piezoelectric material in conjunction with a well-determined amount of electric force. It was stated in their research that the applied electric field induced relevant deformation in the piezoelectric material, which ultimately resulted in additional force/moment in the adhesive material. This induced force/moment helped in neutralising the stress singularities developed within the adhesive bondline. Later on, Cheng and Li [87] implemented the same concept of piezoelectric material for improving the torsion strength of adhesive-bonded tubular joints.

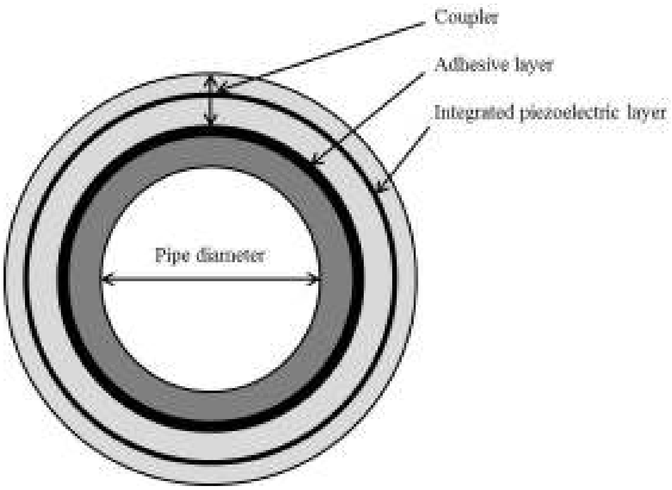

Fig.2.12 *Schematic of adhesive joint with piezoelectric layer in the coupler proposed by Cheng et al. [74,75].*

2.4. Concluding remarks

From the preceding review of the technical literature pertaining to adhesive joining technology for tubular composite structures, it can be concluded that adhesive joints are an advancing technology in the field of FRP piping. With the cited advancement in joining techniques, bonding of composite pipes is becoming relatively simple and less cumbersome in terms of time and alignment. Semi-automation and field-friendliness are reported as a key aspect in achieving consistently high joint quality, long-term performance, and cost-effectiveness of composite piping as a whole.

2.5 Bibliography

1. F.Ascione, G.Mancusi, *Axial/bending coupled analysis for FRP adhesive lap joints*, Mech. Adv. Mater. Struct. 17 (**2010**) 85-98.

2. Y.X.Gan,X.Yong, *Effect of interface structure on mechanical properties of advanced composite materials*, Int. J. Mol. Sci. 10 (**2009**)5115-5134.

3. M.D.Banea, L.D.Silva, *Adhesively bonded joints in composite materials: an overview*, J. Mater. Des. Applic. 224 (**2010**) 51-62.

4. S.A.Meguid, Y.Sun, *On the tensile and shear strength of nano-reinforced composite interfaces*, Mater. Des. 25 (**2004**) 289-296.

5. R.D.Adams, N.A.Peppiatt, *Stress analysis of adhesive bonded tubular lap joints*, J. Adhes. 9 (**1977**) 1-18.

6. L.Hollaway, A.Ramh, M.Gunn, *Optimisation of adhesive bonded composite tubular sections*, Compos. Struct. 16 (**1990**) 125-170.

7. H.N.Hashmi, J.N.Rossetos,A.P. Melo, *Multiaxial fatigue life evaluation of tubular adhesively bonded joints*, Int. J.Adhes. Adhes. 17 (**1997**) 55-63.

8. F.Mortensen, O.T.Thomsen, *Coupling effects in adhesive bonded joints*, Compos. Struct. 56 (**2002**) 165-174.

9. F.Mortensen, O.T.Thomsen, *Analysis of adhesive bonded joints: a unified approach*, Comps. Sci. Technol. 62 (**2002**) 1011-1031.

10. J.L.Lubkin, E.Reissner, *Stress distribution and design data for adhesive lap joints between circular tubes*, J. Appl. Mech. 78 (**1958**) 1213-1221.

11. O.Volkersen,*Recherchessur le theoric des assemblages colles, Constr*. Metall. 4 (**1965**)3-13.

12. M.Goland, E.Reissner, *The stresses in cemented joints*, J. Appl. Mech. 66 (**1944**) 17-27.

13. R.S.Alwar, Y.R.Nagaraja, *Viscoelastic analysis of adhesive tubular joint*, J. Adhes. 8 (**1976**) 76-92.

14. L.P.Terekhova, I.A.Skoryi, *Stresses in bonded joints of thin cylindrical shells*, Streng. Mater. Vol. 4 (**1972**) 1271-1274.

15. X.Wei, L.Guoqiang, *Finite difference three dimensional solution of stresses in adhesively bonded composite joint subjected to torsion*, Int. J.Adhes. Adhes. 30 (**2010**) 191-199.

16. P.J.Hipol, *Analysis and optimsation of tubular lap joint subjected to torsion*, J. Compos. Mater. 18 (**1994**) 298-310.

17. S.R.Groves, D.F.Adams, *Analysis of a bonded joint in a composite tube subjected to torsion*, J. Compos. Mater. 15 (**1981**) 211-224.

18. J.H.Choi, D.G.Lee, *Experimental investigation of the static torque transmission capabilities of the adhesively bonded single lap joints*, J. Mater. Process. Technol. 48 (**1995**) 341-347.

19. H.Ramin, K.Shahin, F.Taheri, *On the influence of overlap length on static capacity and fatigue life of adhesively bonded joints with tubular composite adherends subject to torsional loading*, Int. J. Mater. Prod. Technol. 40 (**2011**) 165-185.

20. J.H.Choi, D.G.Lee, *An experimental study of the static torque capacity of the adhesively bonded tubular single lap joint*, J.Adhes. 55 (**1996**) 245-260.

21. W.T.Kim, D.G.Lee, *Torque trnsmissioncapabilitites of adhesively bonded tubular lap joints for composite drive shafts*, Compos. Struct. 30 (**1995**) 224-240.

22. E.D.Reedy, T.R.Guess, Composite to metal tubular lap joints, Int. J.Fract. 63 (1993) 351-367.

23. T.R.Guess, E.D.Reedy, A.M.Slavin*Testing composite to metal tubular lap joints*, J. Compos. Tech. Res. 17(**1995**) 117-124.

24. V.V.Bolotin, *Delaminations in composite structures- its origin, buckling, growth and stability*, Composites Part B. 27B (**1996**) 129-145.

25. M.Quin, Y.A.Dzenis, *Analysis of single lap adhesive composite joints with delaminated adherends*, Composites Part B. 34B (**2003**) 167-173.

26. S.K.Panigrahi, B.Pradhan, *through the width delamination damage propogationcharecteristics in single- lap laminated FRP composite joints*, Int. J. Adhes. Adhes.29 (**2009**)114-124.

27. A.R.Esmaeel, F.Taheri, *Stress analysis of tubular adhesive joints with delaminated adherend*, J. Adhes. Sci. Technol. 23 (**2009**) 1827-1844.

28. R.R.Das, B.Pradhan, *Adhesion failure analysis of bonded tubular single lap joints in laminated fibre reinforced plastic composites*, Int. J. Adhes. Adhes. 30 (**2010**) 425-438.

29. O.T.Thomsen, *Elsto-static and elasto-plastic stress analysis of adhesive bonded tubular lap joints*, Compos. Struct. 21 (**1992**) 249-259.

30. S.Gali, O.Ishai, *Interlaminar stress distribution within adhesive layer in the non-linear range*, Int. J. Adhes. Adhes. 1 (**1978**) 253-266.

31. S.Gali, G.Dolev, O.Ishai, *An effective stress/strain concept in the mechanical characterisation of structural adhesive bonding*, Int. J. Adhes. Adhes. 1 (**1980**) 135-140.

32. G.Dolev, O.Ishai, *Mechanical characterisation of adhesive layer in situ and as a bulk material*, J. Adhes. 12 (**1981**)283-294.

33. L.Keller, C.Decker, K.Zahouily, S.Benfarhi, J.M.L.Meins, J.M.Brendle, *Synthesis of polymer nano-composites by UV curing of organoclay-acrylic resins*, Polym. 45 (**2004**) 7437-7447.

34. H.Ramin, F.Taheri, *Non-linear investigation of overlap length effect on torsional capacity of tubular adhesively bonded joints*, Compos. Struct. 91 (**2009**) 186-195.

35. H.Ramin, N.Cheraghi, F.Taheri, *An engineering approach for desing and analysis of metalic pipe joints under torsion by the finite element method*, J. Str. Analys. Eng. Des. 41(**2006**) 443-452.

36. H.Ramin, K.Shahin, F.Taheri, *On the influence of overlap length on static capacity and fatigue life of adhesively bonded joitns with composite adherends subject to torsion loading*, Int. J. Mater. Prod. Technol. 40(**2011**)165-185.

37. G.Huysmans; J.F.Marsol; I.Verpoest; J.D.Roeck; L.D.Ridder; J.Vansant, *A field friendly rigid composite coupler for GRP pipes*. 1997, Compos.Struct.31(**1997**) 155-164.

38. G.Huysmans, I.Verpoest, G.D.Roeck, *Structural analysis of GRP pipe couplers by using fracture mechanical approach*, Composites Part B. 29B (**1998**) 477-487.

39. M.M.A. Wahab, G.D.Roeck, *A fracture mechanics approach for designing an adhesive joint for glass fibre reinforced pipes*, J. Adhes. Sci. Technol. 11 (**1997**)719-733.

40. P.Mertiny, F.Ellyin, *Joining of fibre-reinforced polymer tubes for high-pressure applications*, Polym. Compos. 27(**2006**)99-109.

41. P.Mertiny, F.Ellyin, A.Hothan, *Stacking sequence effect of multi-angle filament wound tubular composite structures*, J.Compos. Mater. 38 (**2004**) 1095-1113.

42. P.Mertiny, F.Ellyin, A.Hothan, *An experimental investigation on the effect of multi-angle filamnet winding on the strength of tubular composite structures*, J. Compos. Sci.Technol. 69 (**2004**) 1-9.

43. P.Mertiny, K.Ursinus, *A methodology for assesing fatigue degradation of joined fibre-reinforced polymer composite tubes*, Polym. Test. 26 (**2007**) 751-760.

44. S.A.Hashim, M.J.Cowling, S.Lafferty, *The integrity of bonded joints in large composite pipes*, Int. J. Adhes. Adhes. 18 (**1998**) 421-429.

45. E.M.Knox, S.Lafferty, M.J.Cowling, S.A.Hashim, *Design guidance and structral integrity of bonded connections in GRE pipes*, Composites Part A. 32 (**2001**) 231-241.

46. Z.Zhu, I.Ahmad, A.Mirmiran, *Fatigue modelling of concrete-filled fibre reinforced polymer tubes*, J. Compos. Constr. 13 (**2009**) 582-590.

47. R.M.Guedes, *Viscoplastic analysis of fibre reinforced polymer matrix composites under various loading conditions*, Polym. Compos. 30 (**2009**)1601-1610.

48. S.C.Yen,D.H.Morris, *Creep and fatigue lifetime prediction of polymer matrix composites based on simple cumulative damage laws*, Composites Part A. 39 (**2008**) 1716-1725.

49. P.W.Scott, J.S.Lai, A.H.Zureick, *Creep behaviour of fibre reinforced polymeric composites: a review of the technical literature*, J. Reinf. Plast. Compos. 14 (**1995**) 588-617.

50. E.M.Knox, M.J.Cowling, S.A.Hashim, *Creep analysis of adhesively bonded connection in GRE pipe including the effect of defects*, Composites Part A. 31 (**2000**) 583-590.

51. W.N.Findley, *Combined stress creep of non-linear viscoelastic*, Applied science publication, **1971**.

52. E.M.Knox, M.J.Cowling, S.A.Hashim, *Fatigue performace of adhesively bonded connections in GRE pipes*, Int. J. Fatigue. 22 (**2000**) 513-519.

53. M.A.Stubblefield, C.Yang, S.S.Pang, R.H.Lea, *Development of heat activated joining technology for composite to composite pipe using prepreg fabric*, Polym. Eng. Sci. 38 (**1998**) 143-149.

54. P.F.Mensah, M.A.Stubblefield, S.S.Pang, D.Wingard, *Thermal analysis characterisation of fibre glass epoxy prepreg used to join composite pipes*, Polym. Eng. Sci. 39 (**1999**) 778-788.

55. L.Guoqiang, D.Dishili, S.Carlos, P.Jerry, S.P.Sung, *Joining composite pipes using hybrid prepreg welding and adhesive bonding*, Polym. Compos. 24 (**2003**) 697-705.

56. G.Li, J.E.Helms, S.S.Pang, *Development of high pressure composite butt weld joints*, Polym. Compos. 24 (**2003**) 60-67.

57. G.Li, D.Davis, C.Stewart, J.Peck, S.S.Pang, *Joining composite pipes using hybrid prepreg welding and adhesive bonding*, Polym. Compos. 24 (**2003**) 697-705.

58. S.S.Pang, G.Li, H.D.Jerro, P.Jerry, *Fast joining of composite pipes using UV curing FRP composites*, Polym. Compos. 25 (**2004**) 298-306.

59. C.Decker, *Kinetic study and new applications of UV radiation curing*, Macromol. Rapid Commun. 23 (**2002**) 1067-1093.

60. T.Scherzer,U.Decker, *Real time FTIR-ATR spectroscopy to study the kinetics of ultrafast photopolymerisation reactions induced by monochromatic UV light*, Vib. Spectrosc. 19 (**1999**) 385-398.

61. C.Decker, L.Keller, K.Zahouily, S.Benfarhi, *Synthesis of nanocomposite polymers by UV radiation curing*, Polym. 46 (**2005**) 6640-6648.

62. O.Soppera, C.Barghorn, *Real-time Fourier transform infrared study of the free-radical ultraviolet-induced polymerization of a hybrid sol–gel. II. The effect of physicochemical parameters on the photopolymerization kinetics*, J.Polym. Sci. Part A. 43 (**2003**) 831-840.

63. G.T.Russell, R.G.Gilbert, D.H.Napper, *Chain length dependent termination rate process in free radical polymerisations.1.Theory*, Macromolecules. 25 (**1992**) 2459-2469.

64. J.H.Harris, P.H.Jacobsen,D.M.O. Doherty, *The effect of curing light intensity and test temperature on the dynamic mechanical properties of two polymer composites*, J. Oral Rehabil. 26 (**1999**) 635-639.

65. J.A.Peck, G.Li, S.S.Pang, M.A.Stubblefield, *Light intensity effect on UV cured FRP coupled composite pipe joints*, Compos. Struct. 64 (**2004**) 539-549.

66. A.P.Jerry, A.J.Randy, S.S.Pang, G.Li, B.H.Smith, *UV cured FRP joint thickness effect on coupled composite pipes*, Compos. Struct. 80 (**2007**) 290-297.

67. J.K.Kim, D.G.Lee, *Effects of applied pressure and temperature during curing operation on the strength of tubular single lap adhesive joints*, J. Adhes. Sci. Technol. 18 (**2004**) 87-107.

68. H.Smith. *Adhesive bonded single lap joints*, NASA, **1973**. CR.

69. R.D.Adams, W.C.Wake, *Structural adhesive joints in engineering*. 1st. London : Elsevier, **1984**.

70. M.Y.Tsai, J.Morton, *An evaluation of analytical and numerical solutions to the single-lap joint*, Int. J. Solids Struct. 31 (**1994**) 2537-2563.

71. T.M.Roberts, *Shear and normal stresses in adhesive joints*, J. Eng.Mech. 115 (**1989**) 2460-2479.

72. S.Cheng, D.Chen, Y.P.Shi, *Analysis of adhesive bonded joints with non-identical adherends*, J. Eng.Mech. 117 (**1991**) 605-623.

73. A.M.Albat, D.P.Romilly, *A direct linear-elastic analysis of double symmetric bonded joints and reinforcements*, Compos. Sci. Technol. 59 (**1999**) 1127-1137.

74. J.Q.Cheng, F.Taheri, *A novel smart adhesively bonded joint system*, Smart Mater. Struct. 14 (**2005**) 971-981.

75. J.Q.Cheng, F.Taheri, *A smart single lap adhesive joint integrated with partially distributed piezoelectric patches*, Int. J. Solids Struct. 43 (**2006**) 1079-1092.

76. E.F.Crawley, D.L.Javier, *Use of piezoelectric actuators as elements of intelligent structures*, AIAA. 25(**1987**) 1373-1385.

77. C.K.Lee, F.C.Moon, *Modal sensors and actuators*, J. Appl. Mech. 57 (**1990**) 434-441.

78. J.Q.Cheng, C.F.Qian, M.H.Zhao, *Effects of electric fields on the bending behaviour of PZT-5H piezoelectric laminates*, Smart Mater. Struct. . 9 (**2000**) 824-831.

79. X.X.Wu, J.Q.Cheng, B.Wang, *Influence of applied electric field on the energy release rate for cracked PZT/elastic laminates*, Smart Mater. Struct. 10 (**2001**) 970-978.

80. R.C.Batra, T.S.Geng, *Enhancement of the dynamic buckling load for a plate by using piezoceramic actuators*, Smart Mater. Struct. 10 (**2001**) 925-933.

81. Q.T.Luo, L.Tong, *Exact static solutions to piezoelectric smart beams including peel stresses,I theoretical formulation*, Int. J. Solids Struct. 39 (**2002**) 4677-4695.

82. Z.G.Zhou, B.Wang, *The behaviour of two parallel symmetry permeable interface cracks in a piezoelectric layer bonded to two half piezoelectric material planes*, Int. J. Solids Struct. 39 (**2002**) 4485-4500.

83. Z.G.Zhou, B.Wang, Y.G.Sun, *Investigation of the dynamic behaviour of two parallel symmetric cracks in piezoelectric materials use of non-local theory*, Int. J. Solids Struct. 40 (**2003**) 747-762.

84. J.Q.Cheng, B.Wang, S.Y.Du, *A theoretical analysis of piezoelectric/composite laminate with larger amplitude deflection effect part I:fundamental equations*, Int. J. Solids Struct.42(**2005**) 6166-6180.

85. J.Q.Cheng,B.Wang,S.Y.Du, *A theoretical analysis of piezoelectric/composite laminate with large amplitude deflection effect,partII:Hermite differential quadrature method and application*, Int. J. Solids Struct. 42 (**2005**) 6181-6201.

86. J.Cheng, X.Wu, G.Li, S.S.Pang, F.Taheri, *Design and analysis of smart composite pipe joint system integrated with piezoelectric layers under bending*, Int. J. Solids Struct. 44 (**2007**) 298-319.

87. J.Cheng, G.Li, *Stress analysis of a smart composite pipe joint integrated with piezoelectric composite layers under torsion loading*, Int. J. Solids Struct. 45 (**2008**) 1153-1178.

Chapter 3

Dimensional Scaling of Adhesively Bonded FRP Pipe[2]

3.1 Introduction

As discussed in the previous chapter, the rapid development of polymer-based engineering materials with enhanced properties has provided potential substitutes for metallic piping structures [1,2]. A major advantage associated with FRP structures is the presence of a large number of design variables, which allow for maximizing performance by tailoring the structure according to given requirements. Comparatively higher initial costs of FRP piping can be compensated for by lower maintenance needs and longer service life. However, industrial application of FRP piping is still limited, in part due to inadequate knowledge related to the joining of pipe sections. Adhesive bonding is emerging as a promising technique for FRP piping, and in recent years, research has increasingly been focused on this subject [2-5].

Mertiny et al. [6,7] proposed an adhesive bonding method based on filament-wound sleeve couplers, which provides the potential for automation of the adhesive bonding process. Due to less labor intensive and having potential for semi automation, adhesive bonding technique discussed in section 2.2.3 has been considered in this research project as the potential joining technique.

A strength-of-material approach is commonly used to design and optimize structures made from composite materials [8]. Such an approach has also been successfully employed to investigate failure in composite tubular structures [2, 9-12]. In addition to the strength of material approach, significant contributions have also been reported in the field of adhesively bonded tubular joints with respect to their fracture strength [13,14].

---

[2] A version of this chapter has been published as: A.Parashar and P.Mertiny 2012.*J.Adhes*. 88: 866-880

To the author’s knowledge, the available technical literature was mostly concerned with small diameter pipe joints. Limitations associated with the manufacturing, and testing of large diameter pipe joints, restrict researchers from studying the underlying failure mechanism for large pipe joints. An attempt has been made and results are reported in this section to characterize the transition, if any, in the failure mechanism of different diameter pipe joints. The present section documents the investigation of adhesively (epoxy based) bonded FRP pipes with respect to scaling parameters as well as with respect to two different fibre architectures. Joint strength was studied by considering the components made from FRP, i.e. pipe bodies and sleeves couplers, and the adhesive bondline. The work presented herein complements earlier work within the technical literature, which mostly dealt with overall joint strength without explicitly addressing the strength of individual subcomponents constituting the adhesive joint. The present investigation considers dimensional scaling (pipe with increased inside diameter) effects for the subcomponents of a joint separately (i.e. pipe body, sleeve coupler and adhesive bondline), which was accomplished by defining failure indices for the individual subcomponents, enabling the identification of regions of failure under the scope of strength of materials. In addition to the strength of material approach, a virtual crack closure technique has also been employed to study the significance of scaling and fibre architecture on the fracture behaviour of adhesively bonded tubular sections.

3.2 Theory

This chapter incorporates results obtained from two different approaches based on strength of materials and fracture mechanics. A brief introduction for both approaches is provided in the following.

3.2.1 Strength of materials approach

Several criteria are available to predict failure in anisotropic composite structures [2,11-12,15]. In the present work the Tsai-Wu failure theory was employed to study the onset of damage in FRP pipes and overlapping sleeve couplers. To discern failure initiation or yield in the isotropic polymer adhesive the well-known von Mises criterion was used. The Tsai-Wu failure theory describes a three-dimensional failure envelope that is defined by the quadratic expression given in Equation 3.1.

$$F_i\sigma_i + F_{ij}\sigma_i\sigma_j = \beta \text{ with } i, j = 1\ldots 6 \qquad (3.1)$$

Stresses σ_1, σ_2 and σ_3 in Equation 3.1 correspond to the material coordinate system of a unidirectional lamina, i.e. '1' indicates the fibre direction, and '2' and '3' correspond to the in-plane and out-of-plane directions transverse to the fibres respectively; σ_4 is the shear stress in the plane of isotropy, and σ_5 and σ_6 are the longitudinal shear stresses in the 1-2 and 1-3 planes respectively. F_i and F_{ij} in Equation 3.1 are correspondingly second and fourth-order tensors describing the material strength parameters, which are given in Equations 3.2 to 3.9 considering the fibre-reinforced polymer to be a transversely isotropic material. Note that in Equation 3.1 all terms with strength parameters not given by Equations 3.2 to 3.9vanish. On the right-hand-side of Equation 3.1 the failure index β is given. A failure index equal to or greater than unity signifies failure of the material.

$$F_1 = \frac{1}{X_t} - \frac{1}{X_c} \qquad F_2 = F_3 = \frac{1}{Y_t} - \frac{1}{Y_c} \qquad (3.2\text{-}3.3)$$

$$F_{11} = \frac{1}{X_t X_c} \qquad F_{22} = F_{33} = \frac{1}{Y_t Y_c} \qquad (3.4\text{-}3.5)$$

$$F_{44} = \frac{1}{R} \qquad\qquad F_{55} = F_{66} = \frac{1}{S} \qquad (3.6\text{-}3.7)$$

$$F_{12} = F_{13} = -\frac{1}{2}\frac{1}{\sqrt{X_t X_c Y_t Y_c}} \qquad\qquad F_{23} = -\frac{1}{2}\frac{1}{Y_t Y_c} \qquad (3.8\text{-}3.9)$$

where X_t and X_c are the tensile and compressive strength along the fibre direction respectively, Y_t and Y_c are those for the direction transverse to the fibre, and R and S represent the shear strength in the plane of isotropy and the longitudinal shear strength respectively. For the adhesive bondline with isotropic material properties the corresponding failure index was simply defined as the ratio of the von Mises stress to yield stress of the adhesive material. In the present study, global stresses were computed using finite element analysis. For FRP subcomponents, global stress states for each lamina were determined which were subsequently converted into stresses in the material coordinate system using appropriate coordinate transformation operations [16].

3.2.2 Fracture mechanics approach

A modified virtual crack closure technique (VCCT) proposed by Rybicki [17] has been adapted in the research work to study the fracture characteristics of adhesively bonded tubular joints. Raju [18], proposed a simple finite element based mathematical expressions for calculating strain energy release rate (SERR) with higher order parametric elements. Numerical expressions for calculating SERR values with eight node elements (plane 82 as shown in Fig.3.1) is provided in Equations 3.10,3.11 and 3.12 respectively.

In the fracture-based approach; cracks at the bi-material interface were dealt according to the formulation provided in the research of Raju et al. [19]. Raju et al. in their published work [19] on interfacial cracks established the fact that SERR (G_{Total}) values obtained with the finite element were independent to mesh size, hence the solution converges to a finite value, whereas other SERR components such as G_I and G_II were found to be mesh dependent and the solution may not converge to a finite value even with a very fine mesh size.

$$G_I = -(2\Delta)^{-1}\left(P_{3y}(v_1 - v_1') + P_{4y}(v_2 - v_2')\right) \tag{3.10}$$

$$G_{II} = -(2\Delta)^{-1}\left(P_{3x}(u_1 - u_1') + P_{4x}(u_2 - u_2')\right) \tag{3.11}$$

$$G_{Total} = G_I + G_{II} \tag{3.12}$$

whereP_i, u_i and v_i are the nodal forces, sliding displacement and opening displacement respectively at the ith node from the crack tip.

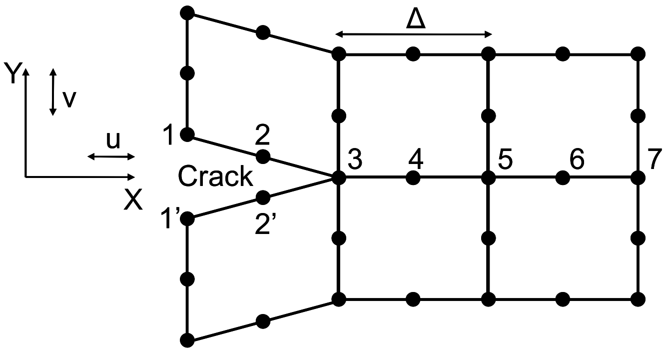

Fig.3.1 *Schematic of crack tip model*

Crack propagation in isotropic materials, under mode I (opening mode) has been studied by many researchers e.g. [20,21] and it has been established that cracks propagate in such a way that either the SERR (G_I) value will be maximized or the mode II stress intensity factor (K_II) becomes zero (K_II= 0). Bradley et al. [21] reported in their research work on isotropic materials that the critical strain energy release rate value under mode I (G_Ic) was significantly smaller than SERR (G_IIc) value under mode II, which further emphasis the tendency of adhesives to fail in

G_{I}(opening) mode, even when the joint was subjected to shear stresses. In addition, microscopic hackle patterns can also be observed experimentally on the delaminated resin surfaces under the mode II failure. Hackle patterns created on the surface of isotropic resin can be attributed to the tendency of resin material to fail under the influence of mode I [22]. Keeping these facts in mind, SERR (G_{I}) was employed in this research as the fracture characterising parameter for cracks lying in adhesive bond line and resin rich layer, whereas for interfacial cracks total SERR (G_{Total}) values were employed.

3.3 Finite element model

Linear elastic finite element modelling was used in this investigation to study the effect of dimensional scaling and fibre architecture on adhesively bonded tubular joints. The joint geometry shown in Figs.3.2 and 3.4 was modelled two-dimensionally within the ANSYS 12 software package. Eight-node axis-symmetric elements ('PLANE82') were used to mesh the joint geometry. Symmetric conditions along the radial direction of the pipe as shown in Fig.3.2 were only applied to the coupler and the adhesive.

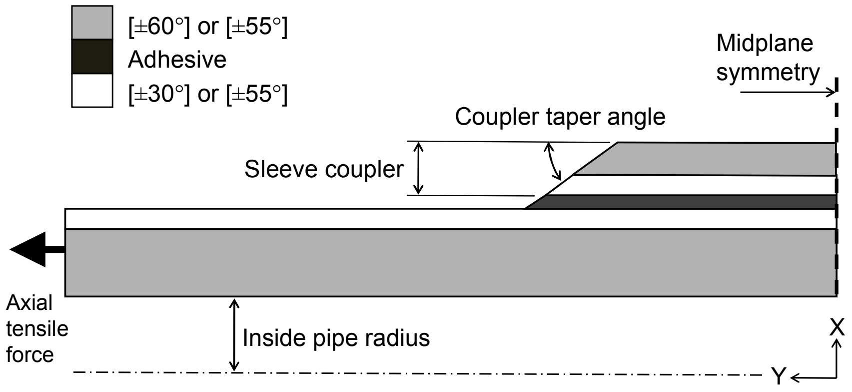

Fig.3.2 *Schematic of finite element model employed using strength of material approach.*

The model shown in Fig.3.2 was used with the strength of material criterion. Two separate approaches were adopted with this model to avoid singularities at the bi-material interfaces. An adhesive fillet with a constant radius of 1.25 mm was introduced at the interface of pipe and adhesive bondline to avoid a bi-material singularity at this location. The mesh density was kept constant in all the scaled models and the third-node criterion as discussed in the research paper by Gleich [23] was employed to avoid singular stress values (details are provided in Appendix 2). According to third-node criterion a stresses atleast two nodes away from the bi-material interface was considered in the calculations. Mesh sensitivity analysis was performed with all four models described in Table 3.3 and results with respect to model #1 with multi-angle fibre architecture [±30°,±60°] are provided in Fig.3.3.

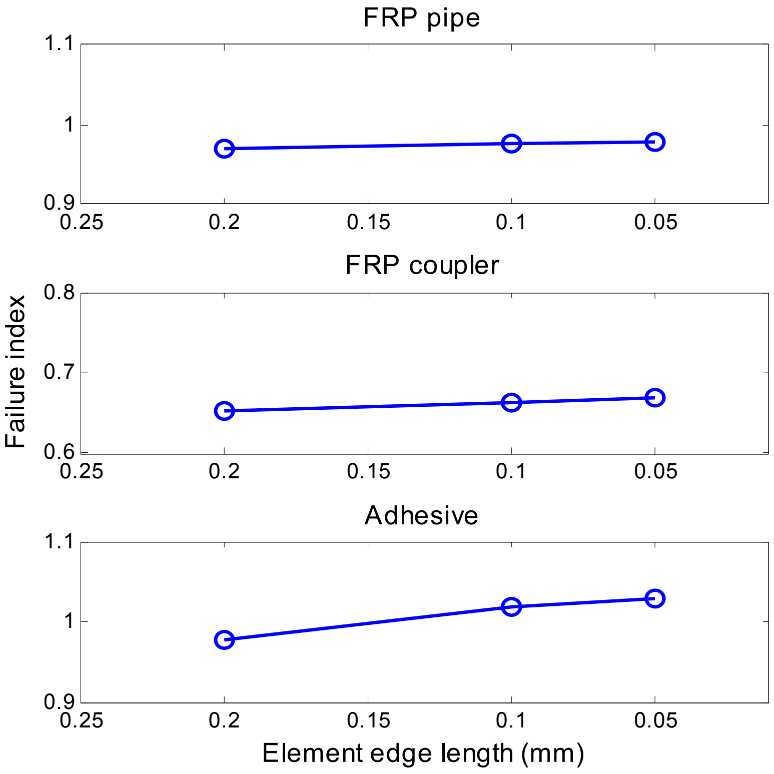

Fig.3.3 *Results of mesh sensitivity analysis for model #1 with multi-angle fibre architecture.*

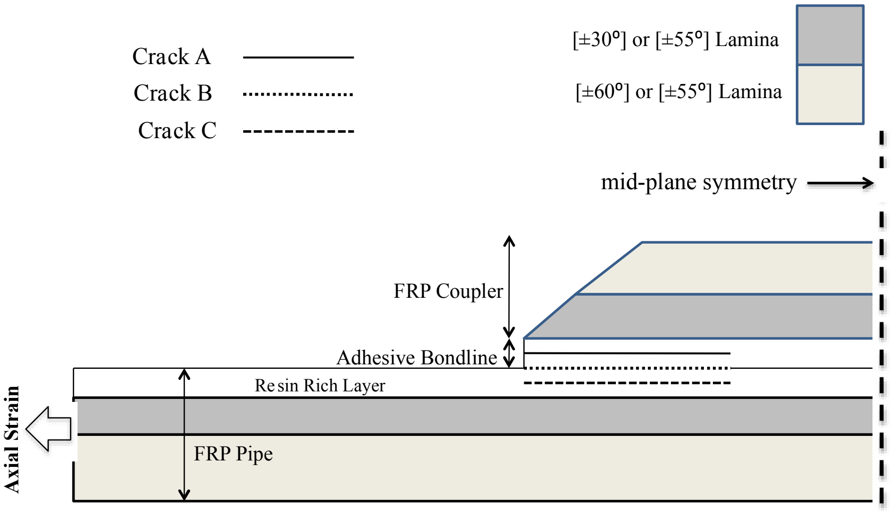

Fig.3.4 *Schematic of finite element model employed using fracture approach.*

A schematic of the axis-symmetric model as employed for the fracture analysis of the adhesive joint is provided in Fig.3.4. Again, Plane 82 elements with 8 nodes and axis-symmetric properties were used to mesh the joint geometry. Three separate crack propagation cases were considered during the numerical analysis, i.e. cracking in the adhesive bondline (Crack A), an interfacial crack (Crack B) and in the resin-rich layer (Crack C).The location of cracks defined above was based on previous experimental results with small diameter pipes, which indicated that region next to the interphase between pipe and adhesive is critical from a strength point of view. The position of the three cracks considered during the modelling is well defined in the 2D geometrical representation of the model in Fig.3.4. Mesh sensitivity analysis was again performed with respect to finite element model shown in Fig.3.4 to verify the convergence of strain energy release rate values. Results obtained from the mesh sensitivity analysis for multi-angle fibre architecture [±30°,±60°] are shown in Fig.3.5. It can be seen from the sensitivity analysis that results converged in the range of 1% even with the coarse meshing.

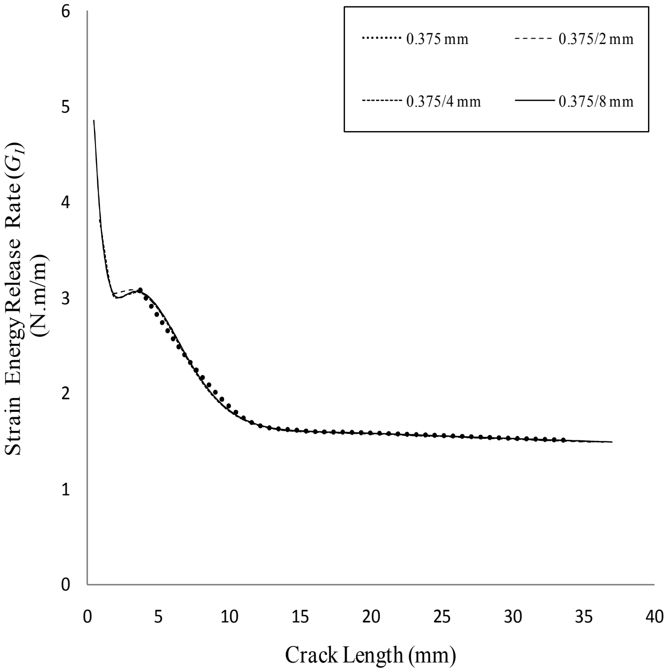

Fig.3.5a *Mesh sensitivity analysis results with different element edge size for crack in adhesive (Crack A).*

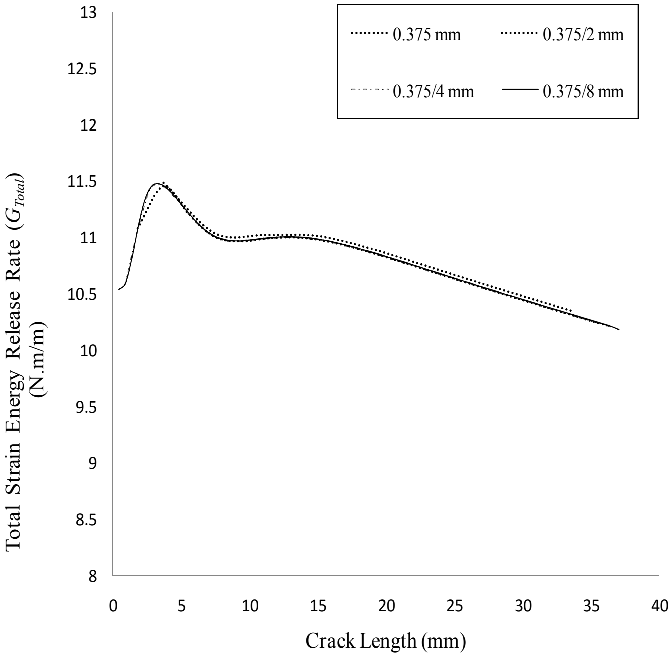

Fig.3.5b *Mesh sensitivity analysis results with different element edge size for crack in interface (Crack B).*

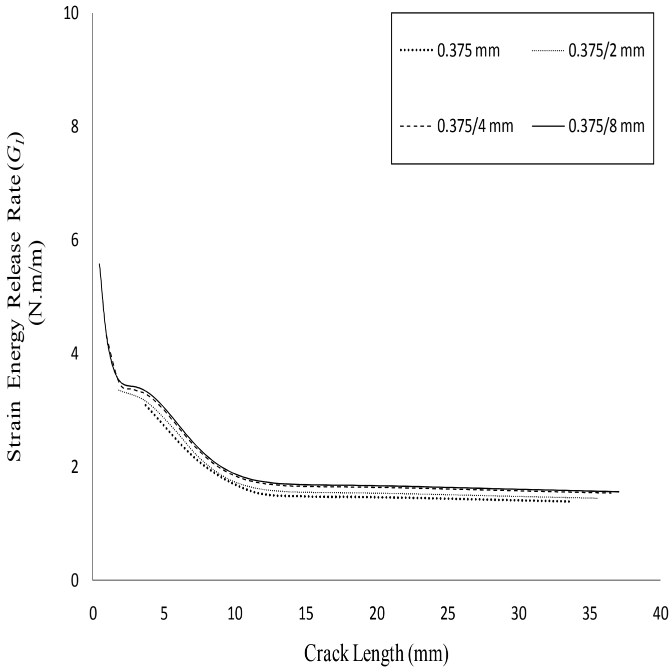

Fig.3.5c *Mesh sensitivity analysis results with different element edge size for crack in resin rich layer (Crack C).*

In the previous experimental work on adhesively bonded pipe joints [6,7] it was established that the critical loading case leading to joint failure was tensile loading along the pipe axis. In accordance with those results the structure was subjected only to axial traction in both the analysis with strength of material as well as fracture approach as shown in Figs.3.2 and 3.4 respectively. A fibre architecture of [±30°,±60°$_m$] was considered in the research work with dimensional scaling for simulating orthotropic material properties for the pipe and sleeve coupler. The fibre architecture was based on experimental work on multi-angle filament-wound tubular structures by Mertiny et al. [24, 25], who showed that a [±30°,±60°$_m$] fibre architecture significantly enhanced the strength of FRP tubes against leakage as well as burst failure for a range of common multi-axial loading scenarios. At the same time the proposed fibre architecture was found to be well within the filament winding processing envelope, ensuring ease of manufacture. In other publications [6,7], pipes with a $[\pm30°,\pm60°_m]_T$ stacking sequence were also employed in conjunction with adhesive joints featuring overlapping sleeve couplers with $[\pm30^o,\pm60^o{}_2]_T$ layup. This configuration placed [±30°] degree layers adjacent to the adhesive bondline in order to provide for high tensile strength of the pipe and coupler in the shear transfer zone. Second fibre architecture of $[\pm55°]_T$, which is more common for manufacturing composite pressure vessels and pipes was also considered in the latter half of this chapter to study the effect of fibre architecture on adhesively bonded pipe sections.

A common elasticity approach (i.e. the Composite Cylinder Assemblage model) was employed to calculate the elastic properties of FRP subcomponents, which were considered to be composed of an epoxy matrix with glass fibre reinforcement. Tubular components made by filament winding are considered in the present study. This process usually produces a pair of undulated angle-ply layers. Hence, models employed herein consider laminates to be composed of orthotropic layers of undulated $\pm\theta$ angle-plies. Note that the laminate nomenclature used herein also reflects this laminate structure. Elastic properties for the different stacking sequences and strength data for a unidirectional lamina are shown in Table 3.1 and 3.2 respectively. Values given in these tables are based on methods and data presented in [16, 26]. Congruent with the experimental work described by Mertiny and Ellyin [6] a constant fibre volume fraction of 0.6 was assumed in the present study for the calculation of lamina properties for all model configurations.

Table 3.1 *Young's moduli (E), shear moduli (G) and Poisson's ratio (v) employed for FRP subcomponents; subscripts x,y and z indicate the radial, axial and hoop direction of the tubular structure respectively.*

Material Properties	FRP [±30°]	FRP [±60°]	Adhesive (Epoxy based)	FRP [±55°]	Resin rich Layer
E_{xx} [GPa]	15.3	15.3	3.4	14.2	4.8
E_{yy} [GPa]	27.3	14.3	3.4	11.7	4.8
E_{zz} [GPa]	14.3	27.3	3.4	20.0	4.8
G_{xy} [GPa]	5.6	5.4	1.2	5.3	1.8
G_{xz} [GPa]	5.4	5.6	1.2	4.7	1.8
G_{yz} [GPa]	11.4	11.4	1.2	13.1	1.8
v_{yx}	0.163	0.291	0.420	0.137	0.340
v_{zx}	0.291	0.163	0.420	0.097	0.340
v_{zy}	0.3012	0.5762	0.420	0.7361	0.340

Table 3.2 *Ultimate (failure) strength properties for unidirectional FRP material*

Strength Property		
Ultimate tensile, parallel to fibre direction	[MPa]	1140
Ultimate compressive, parallel to fibre direction	[MPa]	620
Ultimate tensile, transverse to fibre direction	[MPa]	41
Ultimate compressive, transverse to fibre direction	[MPa]	128
Ultimate shear, longitudinal	[MPa]	89

3.4 Results and discussion

The numerical modelling technique described above was employed in conjunction with respective criteria to identify regions of failure in adhesively bonded pipe joints with scaled inside pipe diameter. To investigate the effect of scaling on the adhesive bonding strength of tubular sections, four separate models were developed using finite elements according to specification provided in Table 3.3.

Table 3.3 *Geometry and joint configuration of scaled pipe joint models*

Parameter	Model #1	Model #2	Model #3	Model #4
Pipe inside diameter	50 mm	100 mm	200 mm	400 mm
Adhesive thickness	0.2 mm	0.4 mm	0.6 mm	0.8 mm
Coupler taper angle	45°	45°	45°	45°
Pipe layup sequence	$[\pm60^{o},\pm30^{o}]_{T}$or $[\pm55^{o}{}_{2}]_{T}$	$[\pm60^{o}{}_{3},\pm30^{o}]_{T}$or $[\pm55^{o}{}_{4}]_{T}$	$[\pm60^{o}{}_{6},\pm30^{o}{}_{2}]_{T}$or $[\pm55^{o}{}_{8}]_{T}$	$[\pm60^{o}{}_{14},\pm30^{o}{}_{2}]_{T}$or $[\pm55^{o}{}_{16}]_{T}$
Coupler layup sequence	$[\pm30^{o},\pm60^{o}]_{T}$or $[\pm55^{o}{}_{2}]_{T}$	$[\pm30^{o},\pm60^{o}{}_{2}]_{T}$or $[\pm55^{o}{}_{3}]_{T}$	$[\pm30^{o},\pm60^{o}{}_{4}]_{T}$or $[\pm55^{o}{}_{5}]_{T}$	$[\pm30^{o},\pm60^{o}{}_{7}]_{T}$or $[\pm55^{o}{}_{8}]_{T}$

Pipe wall thickness scaling was based on the notion of imposing a constant hoop stress σ_{hoop} for each pipe size for a specific internal pressurization p, i.e. according to Equation 3.13 the ratio of internal pipe diameter D to wall thickness t must remain constant for different scales of the structure.

$$\sigma_{hoop} = \frac{pD}{2\,t} \tag{3.13}$$

For each model, the coupler taper angle was kept constant at 45°. The length of overlapping sleeve couplers was set to be three times the pipe diameter. The adhesive bondline thickness was increased incrementally with the scaled pipe diameter. For the adhesive thickness, recommendations made in the research work by Tomblin et al. [27] were considered. However, for the model with the largest pipe diameter (model #4) an adhesive thickness of 0.8mm was assumed since, based on observations described in Mertiny et al., [6], a lower adhesive gap was considered difficult to achieve for the given dimensions. The number of laminae in the coupler was decided on the basis of experimental work of Mertiny et al.

[6,7] and increment in layers for model #3 and 4 was performed in such a way that it will remain as the safest component of the joint.

3.4.1 Scaling with strength of materials approach

Results presented in this section elucidate the influence of scaling on the failure characteristics of adhesively bonded tubular sections. The influence of pipe scaling on joint strength is of considerable interest, which is considered in the present section using the strength of materials approach. The applied tensile loads were selected for each model in such a way that joint failure indices of any one joint component (e.g. pipe, sleeve coupler or adhesive) reached just unity. The applied tensile load for model# 2 was found to be in congruent with that observed for the joint configuration described by Mertiny and Ellyin [6].

The data presented herein are discussed on the basis of failure indices, that is, a failure index above unity indicates a failed component in the joint geometry under consideration. Fig.3.6a delineates the effect of pipe scaling on joint strength for structures with a fibre architecture of $[\pm 30^{\circ},\pm 60^{\circ}_{m}]$. Region critical for the failure was at the interface between FRP pipe and adhesive bondline. In this graph (Fig.3.6a), black bars indicate the failed joint subcomponents (i.e. pipe, coupler or adhesive). It can be observed that failure for the smallest pipe diameter is to be expected within the pipe body. For larger pipe structures, failure will shift to the adhesive (cohesive failure). It is interesting to note that in [6] a crack was apparent that initiated as resin rich layer failure, which is consistent with current results. The observed crack then grew towards the pipe surface, along which it propagated further without penetrating the composite pipe structure. Even though the present modelling approach was not devised to predict a crack path, it is remarkable that fracture observed in actual experiments occurred in the joint zone for which the model predicted a critical stress state (indicated by failure indices close to unity).

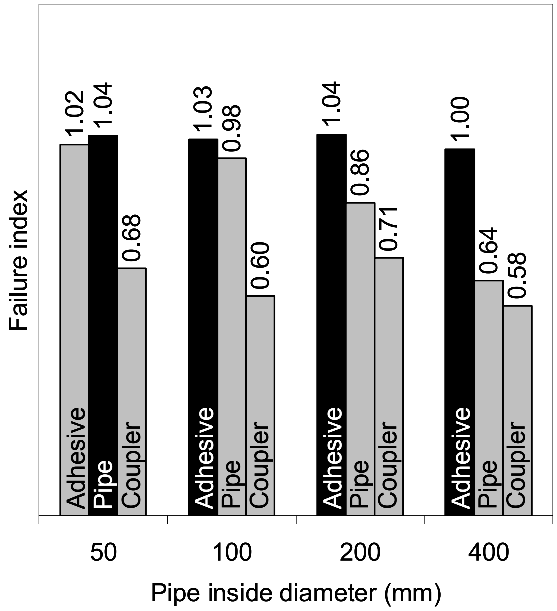

Fig.3.6a *Effect of pipe scaling on joint strength for structures with [30/60] fibre architecture. Black bars indicate failed joint component.*

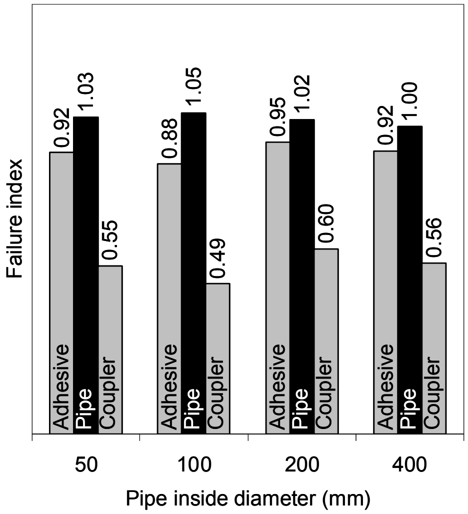

Figure 3.6b *Effect of pipe scaling on joint strength for structures with* [$\pm 55^{o}_{m+1}$] *fiber architecture. Black bars indicate failed joint component.*

Modelling was also performed with [$\pm55^{o}_{m+1}$] fibre architecture, results are plotted in Fig.3.6b, and no significant changes were observed with dimensional scaling. In contrast to the [$\pm30^{o},\pm60^{o}_{m}$] fibre architectures, the analysis predicted failure to occur exclusively in the pipe structure with the [$\pm55^{o}_{m+1}$] type of layup. For both layup configurations the scaled coupler configuration represented the joint component with the lowest failure index.

3.4.2 Effect of scaling on the fracture behaviour of adhesive joint

In this subsection of modelling the modified virtual crack closure technique was employed to investigate the fracture characteristics of adhesively bonded tubular section with scaled inside pipe diameter. In consideration with the numerical results obtained in the previous section with strength of material approach, that no significant changes were observed with a fibre architecture of [$\pm55^{o}_{m+1}$], hence scaling with fracture mechanics approach was studied only with a fibre architecture of [$\pm30^{o},\pm60^{o}_{m}$].

In this section four different models (Table 3.3) were developed for simulating crack growth in adhesive bondline (crack A) and resin rich layer (crack B) as shown in Fig.3.4. During the investigation with each model, axial strain values were kept constant at 0.1%. SERR 'G_{I}' ratios between crack A and crack C are plotted in Fig.3.7 for different scaled models. The strength of materials approach identified the composite pipe and isotropic adhesive as the weakest link in small and large diameter pipe joints respectively. The crack locations as defined above were kept in the identified weakest regions so that a link between the strength of materials and fracture mechanics approaches could be established.

It was assumed in the modelling section that the resin rich layer was an integral part of the composite pipe section. The mathematical relationship given in Equations 3.14 and 3.15 were used to explain the trend shown in Fig.3.7.

$$\frac{G_I(Adhesive)}{G_I(Resin)} \geq 1 \; (Cohesive\ Failure) \tag{3.14}$$

$$\frac{G_I(Adhesive)}{G_I(Resin)} \leq 1 \ (FRP\ Pipe\ Failure) \tag{3.15}$$

With the help of Fig.3.7 and Equations 3.14 and 3.15 it can be concluded that the fracture characteristics of the joint changes with increased pipe diameter. It can be predicted from the trend in Fig.3.7 that the region susceptible to weak fracture behaviour was shifted from the FRP pipe to the adhesive bondline with increased pipe diameter. The results obtained from this section were found to be congruent with the trend obtained with strength of materials approach. Note that the strain energy ratios shown in Fig.3.7 vary only by a small amount from unity. Such a variation may not be significant for experimental evaluation. Nevertheless, variations in strain energy values as obtained here theoretically are noteworthy to validate the trend obtained from the strength of materials approach.

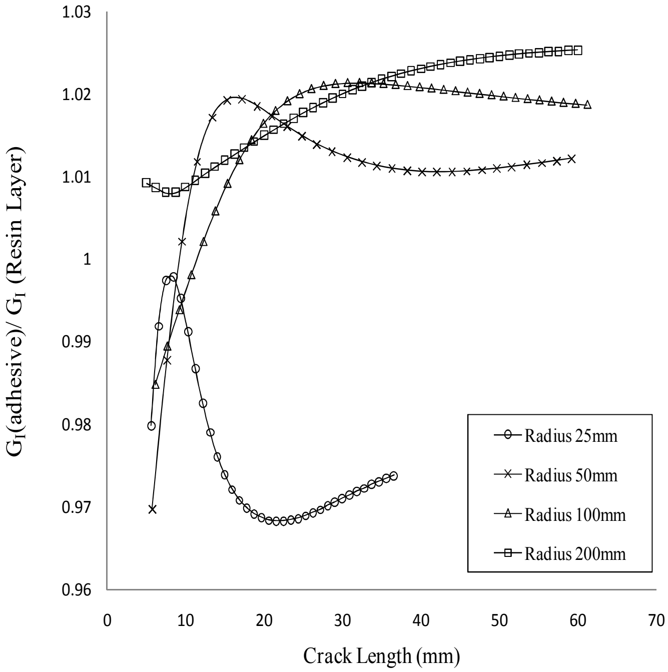

Fig.3.7 *Effect of pipe scaling on energy release rate (G_I) ratios for adhesive and resin.*

In addition to comparing SERR (G_I) values for cracks A and C, modelling was also performed to evaluate the percentage (%) component of SERR (G_I) in 'crack A', when the joint was subjected to axial strain. In Fig.3.8, a comparison has been made between G_I/G_{II} values for a crack propagating in the adhesive bondline with respect to scaled diameter.

The trend depicted in Fig.3.8 indicated an increased percentage of mode I (G_I) driving force with increased inside pipe diameter. It can be concluded from Fig.3.8 that crack growth in the adhesively bonded joint will be enhanced with increased pipe diameter. SERR under mode I (G_I) is considered as the primary driving force for crack growth even in mixed mode failure; this leads to reduced fracture strength of adhesively bonded sections with increased pipe diameter.

Interfacial fracture mechanics is also of great importance because in materials containing interfacial cracks most failures occurs at the interface. At the interface of a bonded joint, there may be a large number of voids, a week bond and a region of high intrinsic stresses. In this section of modelling mixed mode failure criteria (G_{Total}) was assumed for crack growth at the interface (crack B). For small diameter pipes, interfacial failure was predicted to be more dominant in nature on the basis of higher SERR (G_{Total}) values for crack B as shown in Fig.3.9. From the plotted results in Fig.3.9, it can be concluded that in addition to the interface, adhesives also starts behaving as the weakest link in large diameter pipe joints.

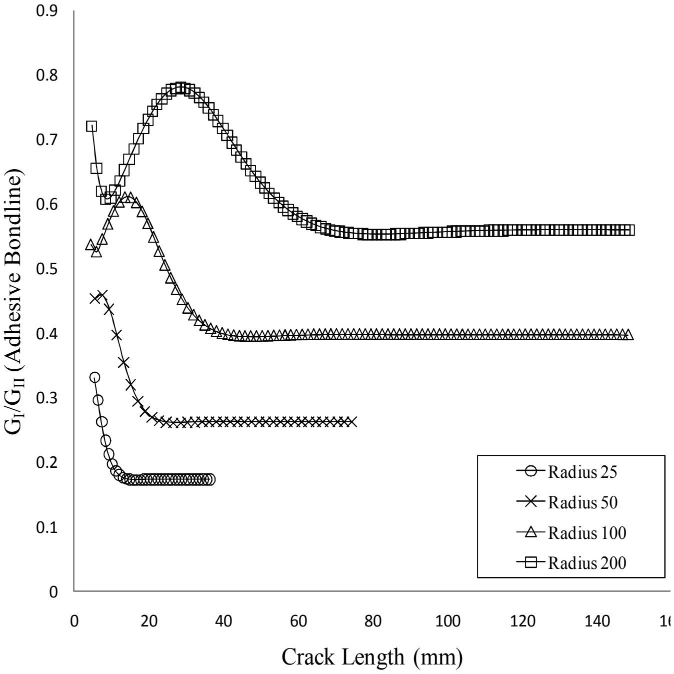

Fig.3.8 *Effect of pipe scaling on the ratio of G_I/G_{II} in adhesive bondline crack.*

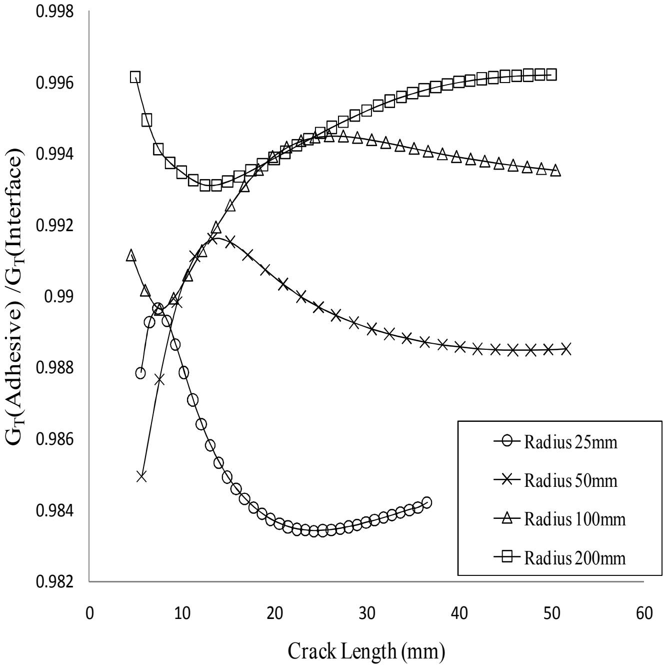

Fig.3.9 *Effect of pipe scaling on the ratio of G_T (adhesive)/G_T (Interface).*

3.4.3 Effect of fibre architecture on joint strength[3]

This subsection describes a study that was performed with respect to two-different types of fibre architecture. Dimensions considered for the finite element model was kept same as described for model #2 in Table 3.3. Initially, a strength of material approach was chosen to identify the region susceptible to failure in adhesively bonded tubular joints with fibre architectures of [$\pm 55°_{m+1}$] and [$\pm 30°,\pm 60°_{m}$]. Following post processing of data, results obtained in terms of failure index for the two fibre architectures are shown in Fig.3.10. The graph reveals that the joint configuration with the fibre architecture of [$\pm 55°_{m+1}$] failed at an applied tensile load of 29 kN, whereas for the fibre architecture of [$\pm 30°,\pm 60°_{m}$] the failure load increased to 34 kN.

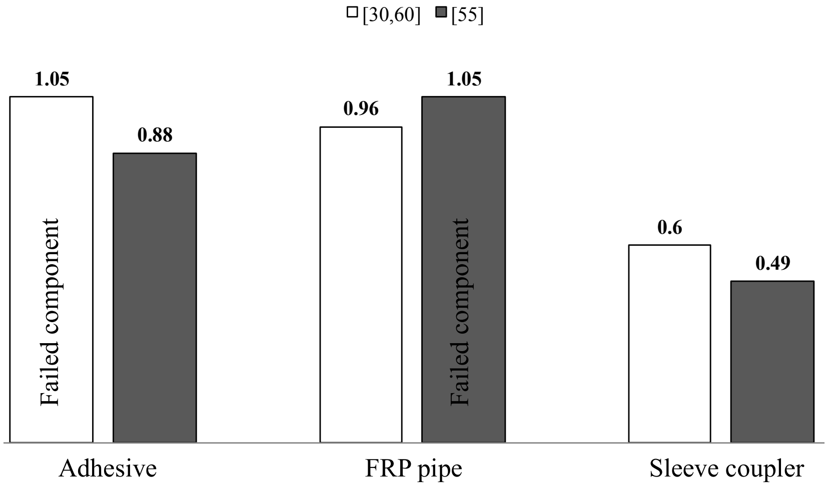

Fig.3.10 *Failure indices of subcomponents of the adhesively bonded FRP tubular sections.*

---

[3] A version of this chapter has been submitted for publication. A.Parashar and P.Mertiny 2012.*Comp.Part B* (accepted with minor revisions)

It can be observed from Fig.3.10 that the overlapping sleeve coupler was identified as the safest component in the joint with the lowest failure index. Figure 3.10 also shows that for the fibre architecture of [$\pm55°_{m+1}$] failure occurred in the FRP pipe section (failure index of pipe is 1.05), whereas with for the [$\pm30°,\pm60°_{m}$] multi angle layup failure shifted to the adhesive material (failure index 1.05).

In the preceding analysis using a strength of materials approach, the region susceptible to failure was identified as the FRP pipe and adhesive bondline for the [$\pm55°_{m+1}$] and [$\pm30°,\pm60°_{m}$] fibre architectures respectively. In the next analysis, using a fracture based approach, crack growth in the adhesive bondline (crack A) and resin rich layer/FRP pipe (crack B) was modelled for the two fibre architectures as shown in Fig.3.4. Crack growth in the adhesive bondline as well as in resin rich layer/FRP pipe was modelled under the applied axial tensile strain of 0.1%. A VCCT approach in conjunction with finite elements was employed to estimate SERR values under opening mode (mode I) and shear mode (mode II) for the crack growth and results are plotted in Fig.3.11. It can be inferred from the results plotted in Fig.3.11 that multi-angle tubular structures provide better strength to the pipe as well as to adhesive material against an opening fracture mode as illustrated by the data plotted in Figs.3.11a and 3.11c respectively. In contrast to mode I failure, a conventional winding angle of [$\pm55°_{m+1}$] showed superior resistance towards the shear failure mode in the adhesive as well as in FRP pipe as illustrated in Figs.3.11b and 3.11d respectively.

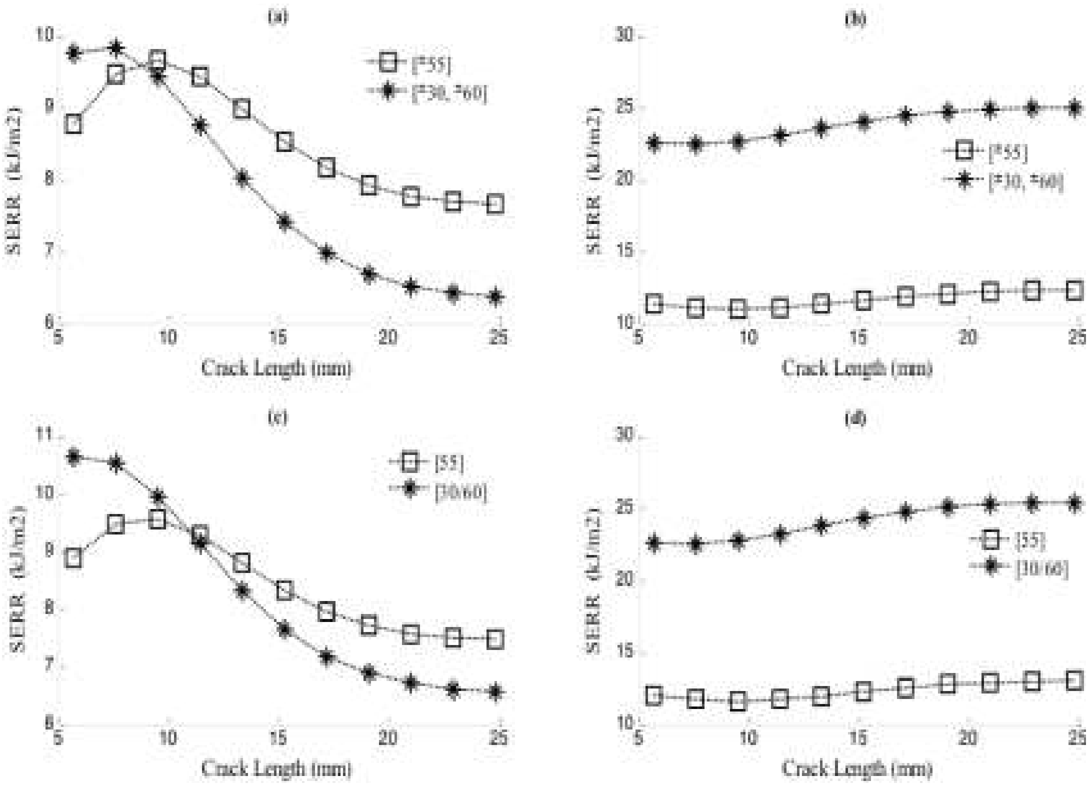

Fig.3.11 *SERR results for two fibre architectures: (a) mode I cracking in adhesive (crack A), (b) mode II cracking in adhesive (crack A), (c) mode I cracking in resin rich layer/FRP pipe (crack B), and (d) mode II cracking in resin rich layer/FRP pipe (crack B).*

3.5 Conclusions

Two separate approaches based on either strength of materials or fracture mechanics were employed in conjunction with finite element modelling to study failure mechanisms of pipe sections joined by means of adhesively bonded overlap sleeve couplers. The analysis with respect to dimensional scaling indicated that the region susceptible to failure shifted from the pipe material in small diameter pipes to the adhesive bondline in large diameter pipes with a fibre architecture of [±30°, ±60°$_m$], whereas no shift in the region of failure was observed for a conventional fibre architecture of [±55°$_{m+1}$]. It can be concluded from the analysis performed in this section that adhesives behave as the weakest link in the joint for large diameter pipes.

It can also be concluded from the strength of materials approach that FRP tubular structures with a fibre architecture of [±30°, ±60°$_{m}$] provide better strength to the adhesively bonded subsections for tensile loading as compared to tubular joints with a fibre architecture of [±55°$_{m+1}$]. The fracture mechanics approach led to the conclusion that the [±30°, ±60°$_{m}$] fibre architecture gives superior strength against mode I failure, whereas the [±55°$_{m+1}$] fibre architecture provides better resistance against a shear fracture mode.

3.6 Bibliography

1. T.Kaneko, S.Ujihashi, H.Yomoda, S.Inagi,*Finite element method failure analysis of a pressurized FRP cylinder under transverse impact loading*, Thin Walled Struct. 46 (**2008**) 898-904.
2. S.A.Hashim, M.J.Cowling, S.Lafferty, *The integrity of bonded joints in large composite pipes*, Int. J. Adhes. Adhes. 18 (**1998**) 421-429.
3. G.Huysmans, J.F.Marsol, I.Verpoest, G.D.Roeck, L.D.Ridder, J.Vansant, *A field friendly rigid composite coupler for GRP pipes*, Compos. Struct. 37 (**1997**) 155-164.
4. E.M.Knox, M.J.Cowling, S.A.Hashim, *Fatigue performance of adhesively bonded connections in GRE pipes*, Int. J. Fatigue. 22 (**2000**) 513-519.
5. E.M.Knox, S.Lafferty, M.J.Cowling, S.A.Hashim, *Design guidance and structural integrity of bonded connections in GRE pipes*, Composites Part A. 32 (**2001**) 231-241.
6. P.Mertiny, F Ellyin, *Joining of fibre-reinforced polymer tubes for high-pressure applications*, Polym. Compos. 27 (**2006**) 99-109.

7. P. Mertiny , K.Ursinus, *A methodology for assessing fatigue degradation of joined fibre-reinforced polymer composite tubes*, Polym. Test. 26 (**2007**) 751–760.

8. C.Stamblewski, B.V.Sankar , D.Zenkert, *Analysis of three-dimensional quadratic failure criteria for thick composites using the direct micromechanics method*, J. Compos. Mater. 42 (**2008**) 635-654.

9. A.K.Roy, T.N.Massard, *A design study of thick multilayered composite spherical pressure vessels*, J.Reinf. Plast. Compos. 11 (**1992**) 479-493.

10. S.Adali, E.B.Summers, V.E.Verijenko, *Optimisation of laminated cylindrical pressure vessels under strength criterion*, Compos. Struct. 25 (**1993**) 305 -312.

11. A.S.Kaddour, P.D.Soden , M.J.Hinton, *Failure of ±55 degree filament wound glass/epoxy composite tubes under biaxial compression*, J. Compos. Mater. 32 (**1998**) 1618-1645.

12. P.Y.Tabakov, E.B.Summers, *Layup optimisation of multilayered anisotropic cylinders based on a 3D elasticity approach*, Comput. Struct. 84 (**2006**) 374-384.

13. G.Huysmans, I.Verpoest, G.DeRoeck, *Structural analysis of GRP pipe couplers by using a fracture mechanical approach*, J. Composites part B 29B (**1998**) 477-487.

14. J.D.Whitcomba, K.Wooa, *Analysis of debond growth in tubular joints subjected to tension and flexural loads*, J. Comput. Struct. 46 (**1993**) 323-329.

15. S.W.Tsai, E.M.Wu, *A general theory of strength for anisotropic materials*, J. Compos. Mater. 5 (**1971**) 58-80.

16. A. K Kaw, *Mechanics composite materials*, Second ed., New York, Taylor and Francis **2006**.

17. E.F.Rybicki, M.F.Kanninen, *A finite element calculation of stress intensity factors by a modified crack closure integral*, Eng. Fract. Mech. 9(**1977**) 931-938.

18. I.S.Raju, *Calculation of strain energy release rates with higher order and singular finite elements*, J. Eng. Frac. Mech. 28 (**1987**) 251-274.

19. I.S.Raju, J.H.Crews, M.A.Aminpour, *Convergence of strain energy release rate components for edge delaminated composite laminates*, J. Eng. Frac. Mech. 30 (**1988**) 383-396.

20. R.V.Goldstein, R.L.Salganik, *Brittle fracture of solids with arbitrary crack*, Int. J. Fract. 10(**1974**) 507-523.

21. W.L.Bradley, *Understanding the translation of neat resin toughness into delamination toughness in composites*. Key Eng. Mat. 37 (**1989**) 161-198.

22. S.M.Lee, *Mode II delamination failure mechanisms of polymer matrix composites*, J. Mater. Sci. 32 (**1997**) 1287-1295.

23. D.M. Gleich, V.Tooren , A.Beukers, *Analysis and evaluation of bond line thickness effects on failure load in adhesively bonded structures*, J. Adhes. Sci. Technol. 15 (**2001**) 1091-1101.

24. P.Mertiny, F.Ellyin, A.Hothan, *An experimental investigation on the effect of multi-angle filament winding on the strength of tubular composite structures*, J. Compos. Sci. Technol. 64 (**2004**) 1-9.

25. P.Mertiny, F.Ellyin, A.Hothan, *Stacking sequence effect of multi angle filament wound tubular composite structures*, J. Compos. Mater. 38 (**2004**) 1095-1113.

26. I.M.Daniel, O.Ishai, *Engineering Mechanics of Composite Materials*, New York, Oxford Univ. Press,**1994**.

27. J.Tomblin, P.Harter,W.Seneviratne,C.Yang, *Characterisation of bondline thickness effects in adhesive joints*, J. Compos. Tech.Res. 24 (**2002**) 332-345.

Phase II(Atomistic analysis)

The scope of Phase II of this research study is as follows:

- Investigation of a suitable nanofiller reinforcement material, i.e. graphene.
- Development of a novel characterisation/modelling technique for graphene at the atomistic scale.
- Validation of the proposed atomistic modelling technique for graphene.
- Study of the effects of weak van der Waals interaction forces.

Work as part of Phase II has previously been prepared in the form of peer reviewed journal publications:

Avinash Parashar and Pierre Mertiny, Study of mode I fracture of graphene sheets using atomistic based finite element modelling and virtual crack closure technique. Int. J. Frac. **2012**,176: 119-126.

Avinash Parashar and Pierre Mertiny, Finite element analysis to study the effect of dimensional and geometrical parameters on the stability of graphene sheets. Comput. Theor. Nanosci. **2012** (Accepted).

Avinash Parashar and Pierre Mertiny, Effect of van der Waals interaction on the fracture characteristics of graphene sheet.**2012** (Under review).

Avinash Parashar and Pierre Mertiny, Effect of van der Waals forces on the buckling strength of multiple graphene sheets.**2012** (Accepted).

Chapter 4

Effect of van der Waals Forces on Fracture Characteristics of Graphene[4]

4.1 Introduction

Joining of composite pipe sections without damaging the fibre architecture is a challenging task, and adhesive bonding techniques are emerging as promising methods for furnishing the joint between two composite pipe sections. Chapter 3 discussed the effects of dimensional scaling and fibre architecture on the adhesive bonding strength for composite pipe sections. It has already been shown by the experimental work of Mertiny and his team that multi angle [$\pm 30°,\pm 60°_m$] filament wound structures are superior to burst pressure and leakage under multi-axial loadings as compared to the more common/conventional winding angle of [$\pm 55°_{m+1}$]. In addition to this, dimensional scaling results from previous chapter indicated a shift in the region of failure from composite pipe material to adhesive material with increased pipe diameter.

To improve the properties of the adhesive material in multi-angle pipe joints, it has been proposed to reinforce the adhesive with the nanofillers. Potential nanofillers considered in this research project for reinforcing the epoxy based adhesive materials were carbon nanotubes (CNTs), nanoclay and graphene platelets.

Challenges in using CNTs are the relatively high cost and stringent processing requirements to protect personnel from potentially health damaging effects. Due to these challenges CNTs are almost exclusively only employed in the aerospace industry where cost is usually not a dominating design factor. In recent years

---

[4] A version of this chapter has been published. A.Parashar and P.Mertiny 2012. Int. J.Frac. 176: 119-126.

graphene has emerged as an alternative to CNTs with comparable mechanical properties. Stankovich et al. [1] recently introduced a unique technique to mass-produce graphene sheets. Relatively low cost of graphene offers the opportunity to reinforce polymers for a variety of applications. Many contributions have been made by researchers to explore the unique properties of graphene [2-4] and related nanocomposites [5-7].

Experimental work of Rafiee et al. [8] further justified the selection of graphene as a nanofiller for this research project(see Table 4.1). In their experimental work with graphene reinforced polymer, an improvement of 60% in fracture toughness was reported for polymer material reinforced with 0.125%wt of graphene. Similar improvements in fracture toughness of epoxy-based polymer was achieved with different weight fractions of nanoclay and CNTs as shown in Table 4.1.

To investigate the effect of nanofiller (e.g. graphene) in this research project, an atomistic modelling technique was proposed. The modelling of graphene is proposed in such a way that it can also be incorporated in the multiscale model in the final phase of the research project. The finite element based modelling of graphene, which is proposed and discussed in subsequent sections was validated with the help of literature data and properties from the continuum scale.

Table 4.1 *Weight fractions required to achieve 60% improvement in fracture toughness of polymer with reference to 0.125% wt. of graphene [8].*

Reinforcement	Weight in terms of graphene (0.125%)
SiO2	120x graphene
Intercalated clay	(20-30)x graphene
DWCNT	4xgraphene (only 40% rise in K_{IC})

Conventional numerical techniques such as Ab initio quantum chemistry methods, molecular dynamics and Monte Carlo simulation are commonly used to study the properties of nanocomposites, even though these methods are computationally intensive [9-10]. Bucon et al. [11] and Gillis [12] employed simple lattice models to study properties of graphene. Kudin et al. [13] used an Ab initio approach to predict a Young's modulus of 1.02 TPa and a Poison's ratio of 0.149 for graphene sheets. Through a similar approach Lier et al. [14] determined a Young's modulus of 1.11 TPa.

Fracture mechanics is a well-established engineering discipline that enables the study and characterization of material properties at the continuum as well as the atomistic level. At the atomistic level, fracture is defined as the breaking of bonds between atoms. Attempts have been made by researchers to establish stress singularities at the atomistic crack tip and also to identify a stress relationship in atomistic models that is proportional to $1/r^{0.5}$, where r is the distance from the crack tip [10,15]. It was reported by Miller et al. [16] for single crystal nickel that the atomistic stress after three atom spacings from the crack tip was consistent with the above concept. In a later publication Zhou et al. [17] also concluded that the atomistic stress field near the crack tip is singular in nature.

The notion of simulating an atomistic structure as space frame structure was explored by Li et al. [18] in their work with CNTs. These researchers later on used the same atomistic based structural model to study the bucking as well as compressive strength of CNTs [19,20]. Tserpes et al. [21] also employed an atomistic based space frame model within a finite element environment to study CNT structural strength.

In the present chapter, a finite element based structural mechanics approach was employed to formulate the mathematical expressions for characterizing mode I fracture in graphene monolayers. An atomistic based approach is proposed herein, which was validated using the results obtained from continuum modelling. The proposed model in finite element was further extended to study the effect of van der Waals forces from neighbouring graphene sheets on fracture characteristics. The proposed atomistic approach was found to be less numerical intensive since it involves less degrees of freedom as compared to other available numerical techniques.

4.2 Fracture model

The atomistic as well as the continuum model were realized within the ANSYS finite element software environment (Version 12). The opening mode fracture characteristics of graphene sheets were investigated. Initially, graphene was modelled as a simple plate structure in the continuum approach, whereas a space frame structure was employed in the proposed atomistic approach to validate the finite element based atomistic model. After validating the methodology, model was further extended to incorporate the effect of van der Waals forces.

4.2.1 Continuum approach

In the continuum approach a rectangular graphene plate was modelled with a constant wall thickness of 0.34 nm. The dimensions of the plate were selected to be consistent with the geometry of the atomistic model, which is discussed in the next sub-section.

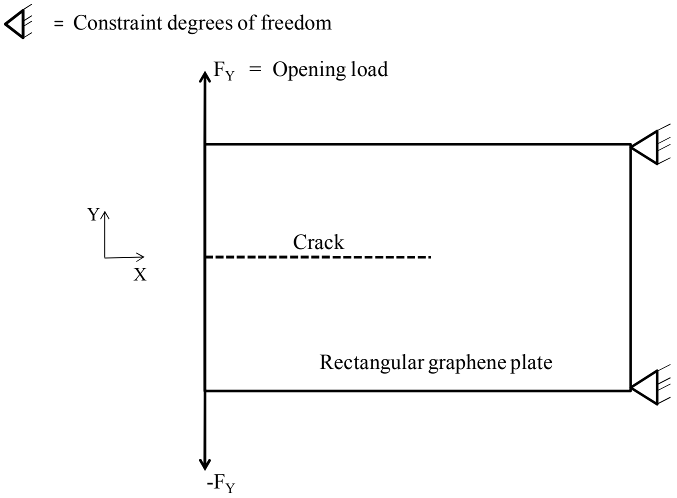

Fig.4.1 *Graphene mono-layer with crack modelled as a continuum plate.*

The modified virtual crack closure technique (VCCT) originally proposed by Rybicki and Kanninen [22] was used in this numerical work to simulate fracture in graphene under opening mode. A schematic of a graphene nano-plate with a crack originating at one of the edges is shown in Fig.4.1. Two-dimensional eight-nodediso-parametric elements (PLANE82) and four-noded quadrilateral elements (PLANE182) were used to mesh and analyse graphene nano-plates in separate models.

The mathematical expressions employed in the continuum approach for determining strain energy release rates (SERR), G_{I}, with PLANE82 and PLANE182 elements are provided in Equations 4.1 and 4.2 respectively. These expressions are self explanatory with the help of Figs.4.2 and 4.3 respectively [23]. A conventional node release technique was used to study the fracture characteristics of graphene sheets.

$$G_I = -(2\Delta a)^{-1}\left(P_{3y}\left(v_1 - v_1'\right) + P_{4y}\left(v_2 - v_2'\right)\right) \tag{4.1}$$

$$G_I = -(2\Delta a)^{-1} P_{2y}\left(v_1 - v_1'\right) \tag{4.2}$$

whereP_{iy} are nodal forces and v_i and v_i' are nodal displacements at node i in the directions tangential to the crack plane.

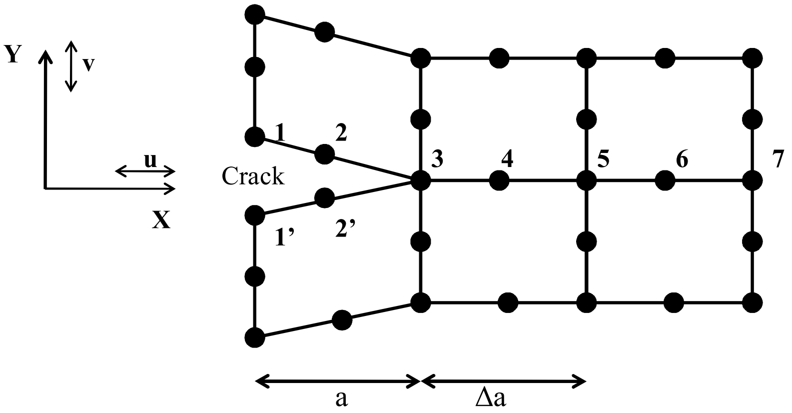

Fig.4.2 *Schematic of continuum fracture model for PLANE 82 elements.*

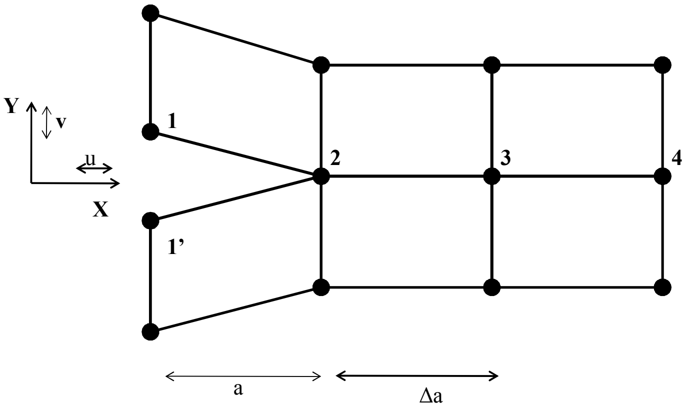

Fig.4.3 *Schematic of continuum fracture model for PLANE 182 elements.*

4.2.2 Atomistic modelling of graphene

The proposed atomistic approach was based on the assumption that molecular attractions can be modelled in the form of a space frame structure. A hexagonal network of sp^2 hybridized carbon atoms was considered to be the repetitive building block for modelling graphene as space frame structure (see schematic in Fig.4.4). At the atomistic level, carbon atoms are covalently bonded with two other carbon atoms at a bonding angle of 120º. These bonds are primarily responsible for maintaining the structural strength of graphene during external tractions. In their finite element model of CNT Tserpes et al. [21] simulated covalent bonds between carbon atoms as structural beams. In the present atomistic model of graphene the distance between carbon atoms in the space frame structure was fixed at 0.1421 nm, which is the experimentally established distance between two carbon atoms [24]. The finite element model thus composed was validated for convergence.

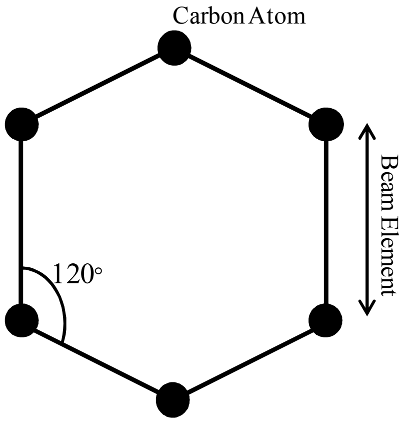

Fig.4.4 *Basic hexagonal unit of carbon atoms in graphene sheets.*

In addition to bonded interactions also non-bonded interactions, i.e. van der Waals and electrostatic forces are present within the atomistic structure of graphene. The potential energy of graphene with bonded as well as non-bonded interactions can be represented by Equation 4.3.

$$\sum U_{total} = \sum U_{bonded} + \sum U_{non-bonded} \tag{4.3}$$

Compared with bonded interactions, non-bonded interactions are considered to have a negligible contribution toward the overall structural strength of graphene. As consequence, non-bonded interactions were disregarded to simplify numerical modelling.Non-bonded interactions are only considered for modelling van der Waals forces between two graphene sheets. The bonded potential between atoms can further be divided into four constituents as described by Equation 4.4 [25]. A schematic depicting these potential energy components, i.e. bond stretching, bending, torsion and inversion, is provided in Fig.4.5.

$$\sum U_{total} = \sum U_{stretching} + \sum U_{bending} + \sum U_{torsion} + \sum U_{inversion} \tag{4.4}$$

Due to the relatively low contributions from the torsional and inversion potentials, these two energy components are usually merged into a single value to simplify the analysis. In the present numerical work the structural strength of bonded carbon atoms was simulated with the help of harmonic potential energy. The properties of beam elements (BEAM3) were estimated by comparing structural strain energies under stretching, bending and torsion with respective harmonic potentials in molecular form. After defining the molecular structure along with its potential energies, harmonic energy values were derived to equate with respective structural strain energy values as explained by Equations 4.5-4.7.

$$U_{Stretch} = \frac{1}{2}\int_0^L \frac{N^2}{EA} dL = \frac{1}{2} K_r (\Delta r)^2 \tag{4.5}$$

$$U_{Bending} = \frac{1}{2}\int_0^L \frac{M^2}{EI} dL = \frac{1}{2} K_\theta (\Delta \theta)^2 \tag{4.6}$$

$$U_{Torsion} = \frac{1}{2}\int_0^L \frac{T^2}{GJ} dL = \frac{1}{2} K_\tau (\Delta \emptyset)^2 \tag{4.7}$$

In the above equations $\mathrm{K_r}(938\mathrm{kcalmol}^{-1}\text{Å}^{-2})$, $\mathrm{K_\theta}(126\mathrm{kcalmol}^{-1}\mathrm{rad}^{-2})$ and $\mathrm{K_\tau}(40\mathrm{kcalmol}^{-1}\mathrm{rad}^{-2})$ are force constants in the molecular potential energy terms [18]; *N*, *M* and *T* represent axial force, bending moment and torsion loads respectively; *E*, *A*, *I*, *G* and *J* are the Young's modulus, uniform cross-section area, moment of inertia, shear modulus and polar moment of inertia for the beam element (ANSYS element type BEAM4) used to simulate the bonded interaction between carbon atoms. Equations 4.8-4.10 were obtained after solving the expressions in Equation 4.5-4.7.

$$\frac{EA}{L} = K_r \tag{4.8}$$

$$\frac{EI}{L} = K_\theta \tag{4.9}$$

$$\frac{GJ}{L} = K_\tau \tag{4.10}$$

Equations 4.8-4.10 were used to approximate the structural parameters for the beam element, i.e. $E = 5.49$ TPa, $A = 0.01687$ nm^2, $I = 0.2267\text{e-}4$ nm^4, $G = 0.871$ TPa, $J = 4.58\text{e-}5$ nm^4 and $L = 0.1421$nm.

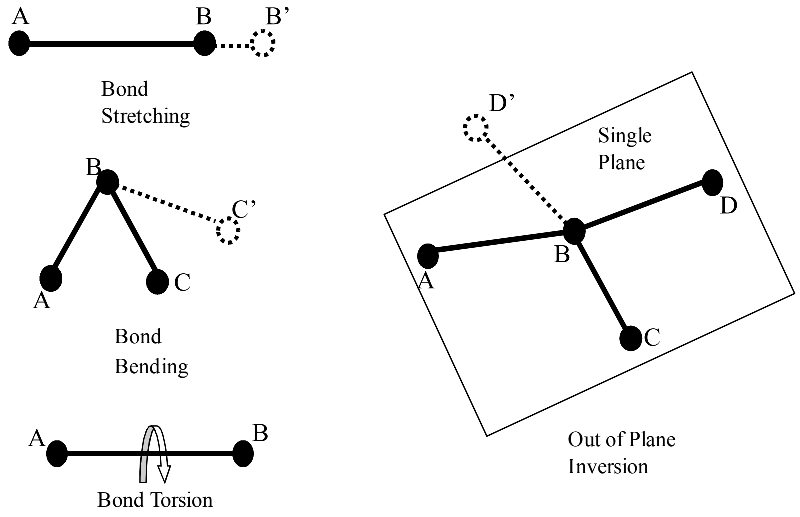

Fig.4.5 *Schematic of interactions between graphene atoms.*

4.2.3 Truss model for van der Waals forces

In the later half of this chapter, multiple graphene sheets are considered in the simulation to further extend the proposed atomistic model. The interaction between different carbon atoms within the same sheet was modelled as a covalent bond, whereas for interactions between atoms of two different graphene sheets non-bonding interactions, i.e. van der Waals forces were taken into account.

The Lennard Jones ‘6-12’ (LJ ‘6-12’) potential was employed for simulating van der Waals interactions between atoms from two different graphene sheets as shown in Fig.4.6 (b and c). LJ ‘6-12’ potential is defined mathematically in Equation 4.11.

$$U(r) = 4\gamma\left[\left(\frac{\varphi}{r}\right)^{12} - \left(\frac{\varphi}{r}\right)^{6}\right] \tag{4.11}$$

where r is the atomic distance between two carbon atoms located on different graphene sheets, φ (0.34m) is hard sphere radius and γ (0.0556 kcal/mol) is potential well depth. In the finite element environment truss elements (LINK8) were deployed to simulate non-bonded interactions. For extracting material properties for those truss elements, LJ ‘6-12’ potential were equated with the structural strain energy of truss elements as proposed by Odegard et al. [26,27] in his research work on CNT and graphene structures. The numerical expression generated after equating the energy terms is provided in Equation 4.12 and was used for calculating the stiffness for truss elements.

$$E(r) = \frac{8\gamma R_{Eq}}{A\left(r-R_{Eq}\right)^{2}}\left[\left(\frac{\varphi}{r}\right)^{12} - \left(\frac{\varphi}{r}\right)^{6}\right] \tag{4.12}$$

where A is the cross-sectional area of the truss element and R_{Eq} (0.3816nm) represents the equilibrium distance between two carbon atoms. For maintaining the efficiency with the proposed numerical model, van der Waals interaction between atoms were considered only when the atomic distance was either equal or less than 2φ.

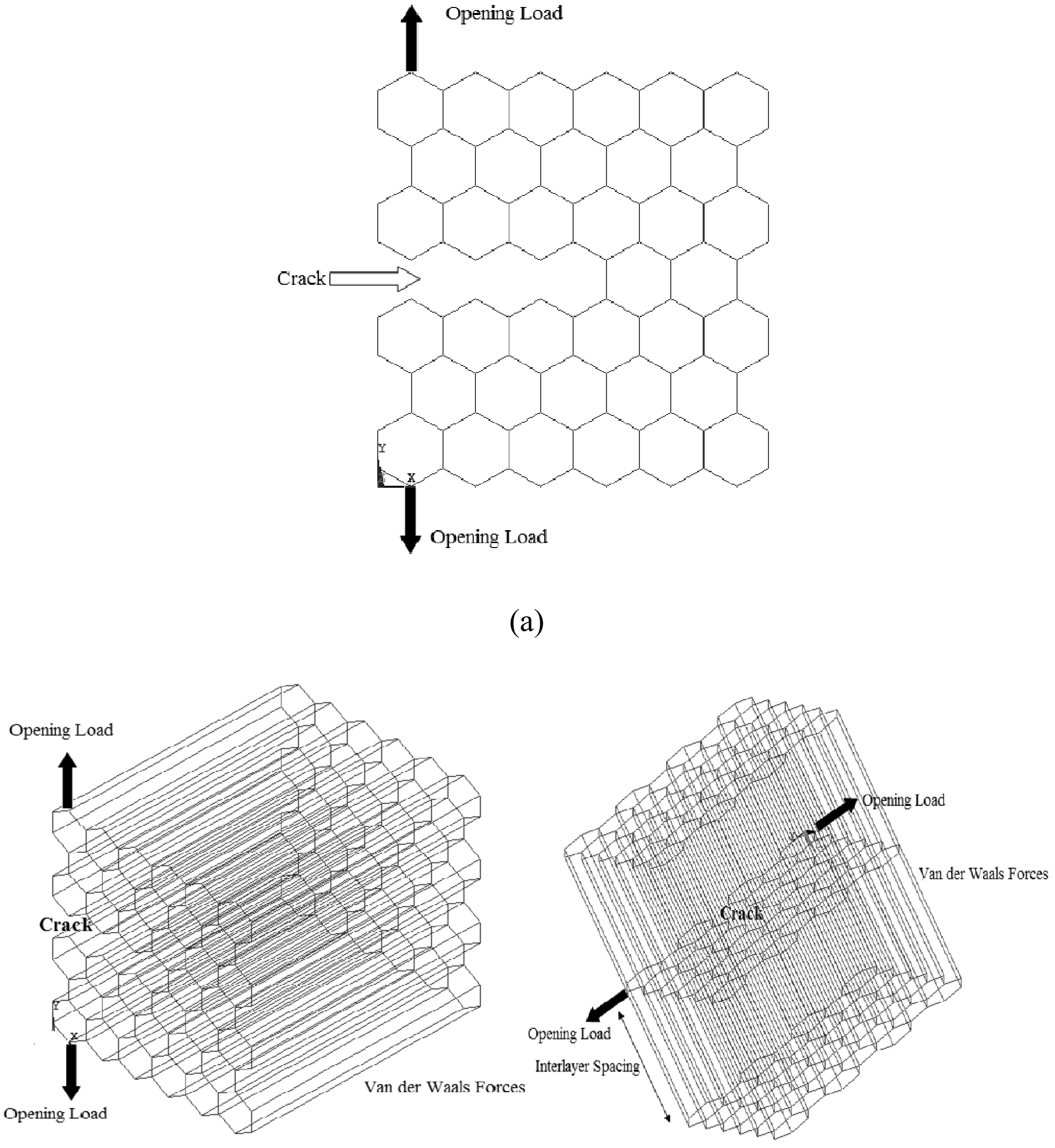

(a)

(b) (c)

Fig.4.6 *Configuration of graphene with applied load: (a) Single graphene sheet with a crack in the center; (b) Twin graphene sheets interlinked with van der Waals interaction and crack lying in the center of the sheet; (c) Triple graphene sheets interlinked with van der Waals.*

4.2.4 Virtual crack closure formulation for atomistic graphene model

Irwin's crack closure technique [28] in conjunction with the work by Rybicki and Kanninen [22] was adapted in this chapter to develop the finite element based atomistic model for assessing fracture characteristics of a graphene monolayer. Fig.4.7 illustrates how in the atomistic model a crack with initial crack length *a* was extended to a length of *a+Δa* by breaking a carbon-carbon bond (indicated by the dotted line). The model geometry considered symmetry about the crack plane.

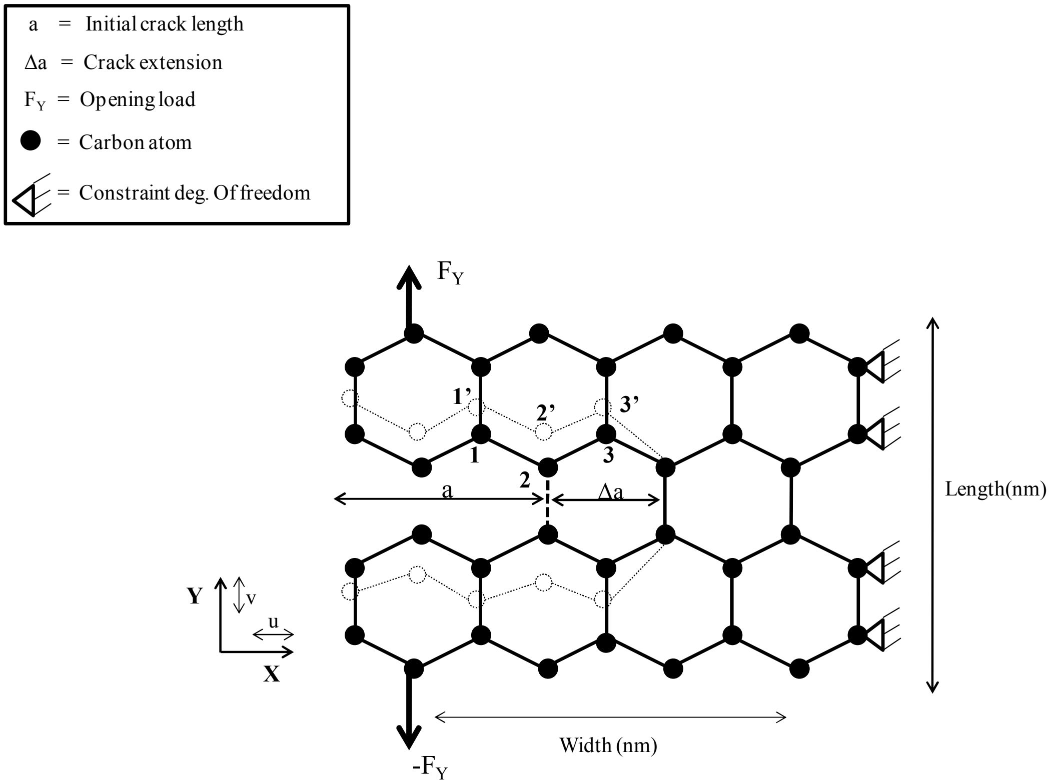

Fig.4.7 *Atomistic based graphene model with a center crack.*

Values for the SERR, G_I, were estimated based on Irwin's notion that the energy released by a crack extending by Δa from a length a to a length $a+\Delta a$ is equal to the work necessary to close the crack to its previous state. In the atomistic model the work required for closing a crack back to its original length can be defined with the help of nodal forces and displacement values as described by the concept expressed in Equation 4.13. The quotient of required work and unit crack extension length Δa was taken herein to define the SERR, G_I, for the atomistic model, which yields an expression analogous to Equation 4.1.

$$\Sigma(\text{work}) = (\text{Work at node 1}) + (\text{Work at node 2}) + (\text{Work at node 3}) \tag{4.13}$$

$$G_I = -(2\Delta a)^{-1}\left(P_{1y}\left(v_1 - v_1'\right) + P_{2y}\left(v_2 - v_2'\right) + P_{3y}\left(v_3 - v_3'\right)\right) \tag{4.14}$$

4.3. Results and discussion

Initially, modelling was performed to validate the proposed finite element model to estimate SERR G_I, values for the single graphene sheet. Later on, this proposed model was implemented to evaluate the effect of van der Waals forces on the fracture characteristics of graphene sheet as shown in Fig.4.6.

4.3.1 Validation of the proposed finite element model.

As described above, the proposed atomistic based finite element model was used to estimate SERR G_I for graphene mono-layers, and results were contrasted to those obtained from continuum modelling. Graphene sheets were modelled under the continuum approach with a Young's modulus of 1.11 TPa [14]. For the determination of SERR values, static loading (F_Y) and constraints as shown in Figs.4.1 and 4.7 were applied for the continuum as well as the atomistic model respectively. The proposed atomistic model was evaluated for two different graphene sheet sizes. Initially the length and width of graphene sheets for both the atomistic and continuum model were set to 16.90nm and 16.73nm respectively.

Simulations were again performed for reduced graphene sheet dimensions of 8.38nm (length) and 8.36nm (width). For both sheet dimensions, an opening load of 10^{-2}N was applied. The number of elements contained in the finite element mesh was about 30,000 for the atomistic model. For the continuum approach approximately 15,000 (PLANE82) elements were used for the large-dimension graphene sheet models; the number of elements was about half of that for the small-dimension models.

For the continuum as well as the atomistic model, nodal force and displacement values required for Equations 4.1, 4.2 and 4.14 were obtained through post processing operations within the finite element software environment. Resulting SERR (G_I) data are depicted in Fig.4.8 with respect to crack length. From the results plotted in Fig.4.8 it can be inferred that SERR values obtained from the proposed atomistic based finite element model are in reasonable agreement with those from the continuum model (i.e. using element type PLANE82 and PLANE 182). The results obtained from the proposed atomistic model have a maximum error of 6% when compared with the corresponding continuum values. In addition, the presented results confirm that the proposed atomistic model can be employed for range of graphene sheet dimensions. It is important to note that fewer degrees of freedom are associated with the proposed model and it is more efficient in terms of numerical simulation. Simulations using the proposed model were thus less computational intensive, which constitutes an advantage of this approach.

4.3.2 *Effect of van der Waals forces on the SERR G_I*[5]

The modified virtual crack closure technique has successfully been implemented for estimating SERR (G_I) values for the opening mode of crack in the graphene

---

[5] A version of this section has been submitted for publication. A.Parashar and P.Mertiny 2012.Solid State Commun. (Under review)

sheet. In this study, several graphene sheets (up to three) were modelled with a constant length and width of 6.25 nm and 6.15 nm respectively.

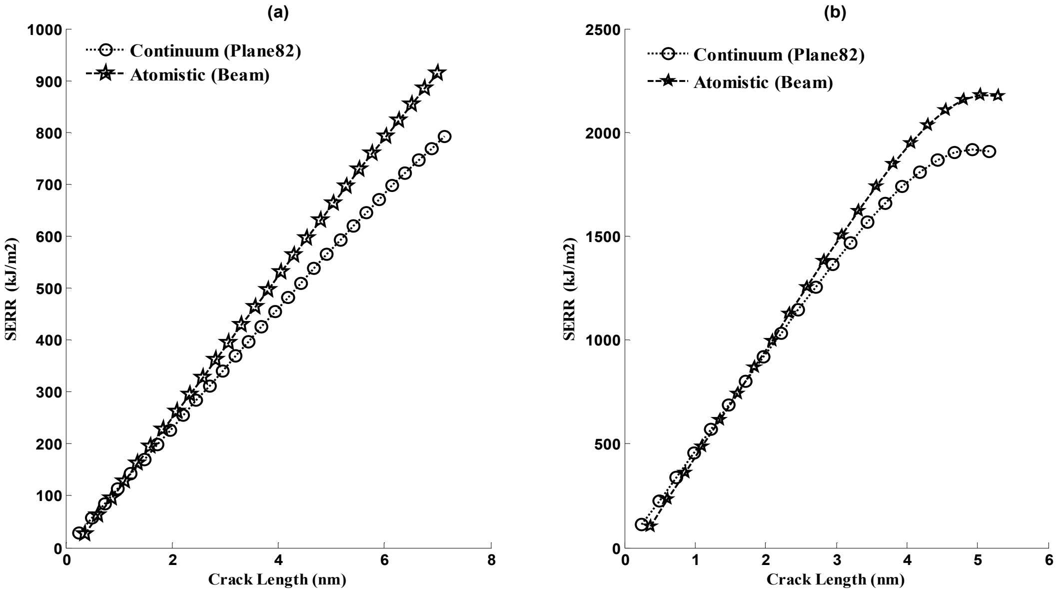

Fig.4.8 *SERR (G_I) values for graphene sheets with length and width corresponding to (a) 16.90 nm and 16.73 nm , and (b) 8.38 nm and 8.36 nm respectively.*

Four different interlayer spacing (as given in Table 4.2) between graphene sheets were used during the simulation. Interlinking force between these graphene sheets were assumed to be the non-bonded van der Waals forces, which are considered to be the function of atomistic distance between graphene sheets under consideration. The atomistic distance of 0.344nm is the experimentally established interlayer spacing between the graphene sheets. For an intercalated nanocomposite interlayer spacing would be increased, and hence, an attempt was made in this section to examine and quantify the effect of increased interlayer spacing on fracture toughness of single graphene sheets.

During the entire course of numerical modelling, SERR (mode I) values were estimated with an opening load of 10 nN. Modelling has been performed with three different set of graphene configurations as shown in Fig.4.6. Results obtained with the three configurations, (a) crack growth in single graphene sheet without any van der Waals interaction forces (as shown in Fig.4.6a), (b) crack growth in graphene under the influence of van der Waals interaction forces from another graphene sheet (as shown in Fig.4.6b) and (c) crack propagation in graphene under the influence of van der Waals interaction forces from both of its sides (as shown in Fig.4.6c) were plotted in Fig.4.9.

Table 4.2 *Different interlayer spacing values considered during the simulation.*

Interlayer spacing	Comments
0.344nm	Experimentally established interlayer spacing [18]
0.3816nm	Equilibrium distance between atoms according to LJ (6-12)
0.425nm	Max LJ (6-12) interaction force between two atoms
0.500nm	Arbitrarily opted distance

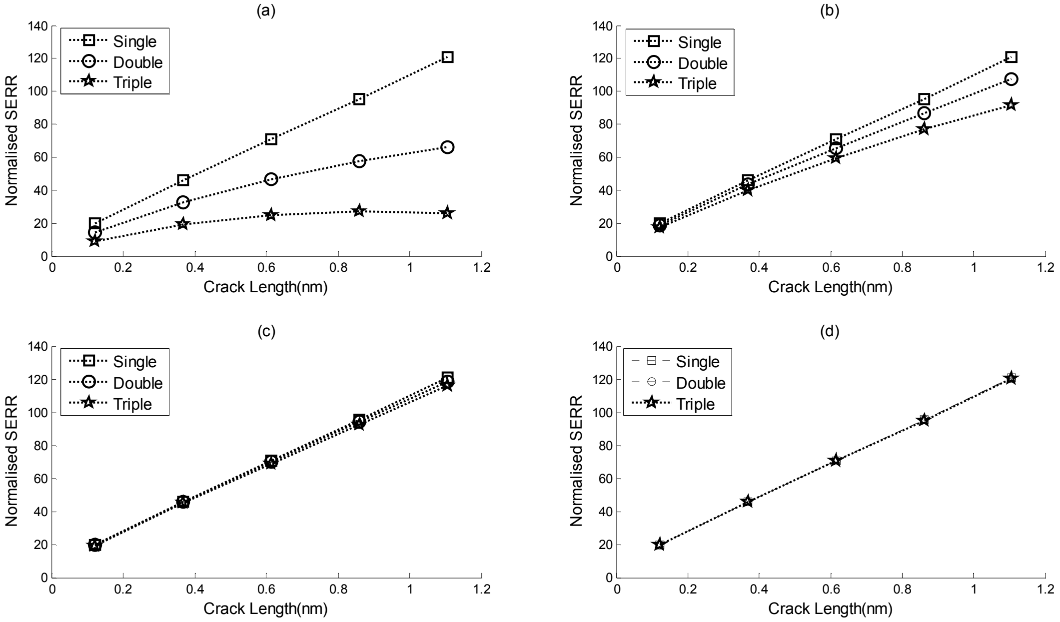

Fig.4.9 *Normalized SERR (GI) values for the three graphene configurations under the opening load of 10 nN and at an interlayer spacing of (a) 0.344 nm (b) 0.3816 nm (c) 0.425 nm (d) 0.500 nm.*

In Fig.4.9 SERR (mode I) values for crack growth in an isolated graphene sheet (Fig.4.6a) were compared with the crack growth in twin (Fig.4.6b) or triple (Fig.4.6c) configurations of graphene with different interlayer spacing. Fig.4.9a represents normalized SERR (mode I) values for the crack growth with an interlayer spacing of 0.344 nm. SERR values were normalised by dividing the actual values with 1 mJ/m^2.A significant improvement in the opening mode fracture characteristics was observed in Fig.4.9a when crack growth was simulated with graphene sheets on either or both of its side. The improvement in the fracture characteristics of graphene sheet with respect to crack growth in an isolated graphene sheet was attributed to the effect of van der Waals interaction forces.

At an interlayer spacing of 0.344nm up to 50% reduction in crack growth of a graphene sheet was observed in Fig.4.9a with the twin configuration of graphene (as described in Fig.4.6b), whereas more than 50% reduction in crack growth was reported with the van der Waals effect under the boundary conditions shown in Fig.4.6c. It can also be observed from the Fig.4.9b that some improvement in fracture characteristics of graphene was still observed at an interlayer spacing of 0.3816 nm, whereas a negligible effect of van der Waals interaction forces was observed at an interlayer spacing of 0.425 nm and 0.500 nm (Figs.4.9c and 4.9d) respectively.

4.4. Conclusions

In this study, a finite element based atomistic model was proposed to simulate the fracture behaviour of graphene mono-layers. The model uses beam elements emulating atomic bonds. It was shown that results in the form of strain energy release rates were congruent with data obtained using continuum models. The proposed model was found to be less computational intensive as fewer degrees of freedom are involved in the analysis. The developed atomistic model has thus the capability to assess fracture characteristics for graphene in its native (atomistic) form while also providing advantages in terms computational effort.The modelling approach as presented in this chapter also has limitations in that it cannot account for impurities/defects within the structure and also cannot interpret the effect of lattice trappings.

The proposed model was further extended to study the effect of van der Waals interaction forces on the opening mode fracture characteristics of a mono graphene sheet. It can be concluded from the finite element simulation that van der Waals interaction forces have a significant impact on the opening mode fracture characteristics of a graphene sheet at an interlayer spacing of 0.344 nm. The effect of van der Waals forces starts to diminish with the increase in interlayer spacing beyond 0.344 nm and ultimately becomes negligible after an interlayer spacing of 0.3816 nm.

4.5 Bibliography

1. S.Stankovich, A.Dmitriy, D.A.Dikin, G.Dommett, K.Kohlhaas, E. Zimney, E.Stach, R.Piner, S.Nguyen, R.Ruoff, *Graphene based composite materials*, Nature 442 (**2006**) 282-286.
2. A.C. Ferrari, *Raman spectroscopy of graphene and graphite: disorder, electron–phonon coupling, doping and nonadiabatic effects*, Solid State Commun. 143(**2007**) 47-57.
3. M.I. Katsnelson, K. S. Novoselov, Graphene: *New bridge between condensed matter physics and quantum electrodynamics*, Solid State Commun. 143 (**2007**) 3-13.
4. C.J. Meyer, A.K. Geim, M.I. Katsnelson, K.S. Novoselov, T.J. Booth, S. Roth, *The structure of suspended graphene sheets*, Nature 446 (**2007**) 60-63.
5. E.J. Duplock, M. Scheffler, P.J.D. Lindan, *Hallmark of perfect graphene*, Phys. Rev. Lett. 92 (**2004**) 225502-4.
6. K.S. Novoseloo, A.K. Geim, S.V. Morozov, D. Jiang, M.I. Katsnelson, I.V. Grigorieva, S.V. Dubonos, A.A. Firsov, *Two-dimensional gas of massless Dirac fermions in graphene*, Nature 498 (**2005**) 197-200.
7. T. Ohta, A. Bostwick, T. Seyller, K. Horn, E. Rotenberg, *Controlling the electronic structure of bilayer graphene*, Science 313 (**2006**) 951-954.
8. M.A. Rafiee, J. Rafiee, I.Srivastave, Z. Wang, H.Song, Z.Z. Yu, N. Koratkar, *Fracture and fatigue in graphene nanocomposites*. Small 6 (**2010**) 179-183.
9. J. L.Tsai, S.H. Tzeng, Y.J. Tzou, *Characterizing the fracture parameters of a graphene sheet using atomistic simulation and continuum mechanics*, Int. J. Solids Struct. 47 (**2010**) 503-509.

10. A. Omeltchenko, J. Yu, R.K. Kalia, P. Vashishta, *Crack front propagation and fracture in a graphite sheet: A molecular-dynamics study on parallel computers*, Phys. Rev. Lett. 78 (**1997**) 2148-2151.

11. A.P.P. Nicholson, D.J. Bacon, *A new force constant model for graphite*, J. Phys. C: Solid State Phys. 10 (**1977**) 295-306.

12. P.P.Gillis, *Calculating the elastic constants of graphite*, Carbon 22 (**1984**) 387-391.

13. K.N. Kudin, G.E. Scuseri, *C2F, BN, and C nanoshell elasticity from ab initio computations*. Phys. Rev. B 64 (**2001**) 235406.

14. G.V. Lier, C.V. Alsenoy, V.V. Doren, P. Geerlings, *Ab initio study of the elastic properties of single-walled carbon nanotubes and graphene*, Chem. Phys. Lett. 326 (**2000**) 181-185.

15. Y. Jin, F.G. Yuan, *Atomistic simulations of J-integral in 2D graphene nanosystems*. J. Nanosci. Nanotechnol . 5 (**2005**) 2099-2107.

16. R. Miller, E.B. Tadmor, R. Phillips, M. Ortiz, *Quasicontinuum simulation of fracture at the atomic scale*, Model Simul. Mater Sci. Eng. 6 (**1998**) 607-638.

17. [16] T. Zhou, X. Yang, C. Chen, *Quasicontinuum simulation of single crystal nano-plate with a mixed-mode crack*, Int. J. Solids Struct. 46 (**2009**) 1975-1980.

18. C. Li, T.W. Chou, *Elastic moduli of multi-walled carbon nanotubes and the effect of van der Waals forces*, Compos. Sci. Technol. 63 (**2003**) 1517-1524.

19. C. Li, T.W. Chou, *Multiscale modelling of compressive behaviour of carbon nanotube/polymer composites*, Compos. Sci. Technol. 66 (**2006**) 2409-2414.

20. C.Li, T.W. Chou, *Modelling of elastic buckling of carbon nanotubes by molecular structural mechanics approach*, Mech. Mater 36 (**2004**) 1047-1055.

21. K.I. Tserpes, P. Papanikos, *Finite element modelling of single-walled carbon nanotubes*, Compos. B 36(**2005**) 468-477.

22. E.F. Rybicki, M.F. Kanninen, *A finite element calculation of stress intensity factors by a modified crack closure integral*, Eng. Fracture Mech. 9 (**1977**) 931-938.

23. I.S. Raju, *Calculation of strain energy release rates with higher order and singular finite elements*, J. Eng. Frac. Mech. 28 (**1987**) 251-274.

24. C. Li, T.W. Chou, *A structural mechanics approach for the analysis of carbon nanotubes*, Int. J. Solids Struct. 40 (**2003**) 2484-2499.

25. M.S. Dresselhaus, G. Dresselhaus, R. Saito, *Physics of carbon nanotubes*, Carbon 33 (**1995**) 883-891.

26. G.M.Odegard, T.S.Gates, K.E.Wise,C. Park, E.J.Siochi,*Constitutive modelling of nanotubes –reinforced polymer composites*. Compos. Sci. Technol. 63 (**2006**) 1671-1687.

27. G.M.Odegard,T.S.Gates, K.E. Wise, L.M. Nicholson,*Equivalent-continuum modelling of nano-structured materials*,Compos SciTechnol 62 (**2002**) 1869-1880.

28. T.L. Anderson, *Fracture mechanics: funda and application*,**2003.**

Chapter 5

Effect of van der Waals Forces on the Stability of Graphene under Compressive Loading[6]

5.1 Introduction

The proposed finite element based atomistic model employed in the previous chapter to study the fracture characteristics of graphene was further extended in this chapter to study the stability of graphene, as an isolated sheet, as well as in a group of two or three sheets. The proposed model was thus extended to demonstrate its versatility in characterising the mechanical properties at the atomistic level.

In the technical literature, few publications have been reported in the field of buckling of graphene sheets. Wilber et al. [1] adopted a continuum approach to discuss buckling of graphene sheets in pairs connected by van der Waals interactions. Sakhaee-Pour [2] numerically investigated the buckling stability of single layer graphene sheets with the help of atomistic modelling. Pradhan [3] employed higher-order shear deformation theory to study buckling characteristics of nano-plates such as graphene sheets.

The study described in the present chapter investigated the buckling stability of graphene monolayers with respect to dimensional as well as geometrical parameters, i.e. aspect ratio, graphene structure geometric configuration and monolayer curvature. To the author's knowledge the technical literature has effectively been mute on the effect of curvature on the buckling stability of graphene as well as on the effect of van der Waals forces on the same strength. The approach taken herein is that of finite element based atomistic modelling used

---

[6] A version of this chapter has been accepted for publication. A.Parashar and P.Mertiny 2012.Comput. Theor. Nanosci. (Accepted)

to investigate the buckling characteristics of graphene monolayers. Owing to this approach, atomistic details can be preserved in the model without compromising the numerical performance of the analysis. Once again the finite element model employed to study the dimensional as well as geometrical parameters was extended to include the effect of van der Waals forces on the buckling stability of graphene sheets.

5.2 Theory and model

5.2.1 Atomistic modelling of graphene

Graphene in the finite element environment was simulated as discussed in Section 4.2.2. Covalent bonding provides the primary structural strength to graphene, which was simulated with the help of beam elements. Interlayer interaction between graphene sheets were simulated with the help of a truss model discussed in Section 4.2.3.

5.2.2 Eigenvalue buckling analysis

A linear analysis for mode one buckling was performed in this work, which is associated with the computation of a bifurcation load and corresponding buckling mode. The analysis in the finite element environment was divided into two sections, i.e. a pre-buckling and a post-buckling analysis [4].

Pre-buckling analysis:

The pre-buckling analysis was performed in the finite element environment to compute the reference stresses (SS^*) within each element. These computed reference values are then used for estimating geometric stiffness matrix (K_G), which is later on needed in the post buckling analysis. To initiate, the analysis in finite element, general matrix form equation provided in Equation 5.1 was employed to estimate the nodal displacements [Q] when the structure was subjected to reference unit load (P_R).

$$[K_o][Q]=[P_R] \tag{5.1}$$

$$\{Q^*\} = [K_o]^{-1}[P_R] \tag{5.2}$$

Here, Q^* and K_o are nodal displacement vector and total stiffness matrix respectively. Total stiffness matrix [K_o] is the assembled global stiffness matrix for the structure defined by elements. Conventional assembling techniques can be used to obtained the global stiffness matrix.

Equation 5.2 is the general solution that is obtained in the finite element analysis after solving the assembled matrices defined in Equation 5.1. Nodal displacement vectors obtained from Equation 5.2 are further post-processed to compute strains and corresponding stress (SS^*) values within each element.

$$\{SS^*\} = [D][B]\{Q^*\} \tag{5.3}$$

In Equation 5.3 matrix [D] represents elasticity matrix (material property), whereas matrix [B] is function of approximating polynomial or shape functions.

Post-buckling analysis:

The post buckling analysis corresponds to a general Eigen value problem as defined by Equation 5.4.

$$[K_o + \lambda K_G]\upsilon = 0 \tag{5.4}$$

$$[K_G] = \int \Gamma^T S\Gamma dV \tag{5.5}$$

Geometric stiffness matrix (K_G) used in Equation 5.4 is defined with the help of Equation 5.5, where Γ is composed of derivatives of shape functions and $S$is function of stress (SS^*) estimated in the pre-buckling analysis. In Equation 5.4, v is the eigen vector of displacements. By solving Equation 5.4 the lowest possible value for the load factor ($\lambda_{\min}$) can be determined, which is then employed to estimate the buckling force given by Equation 5.6.

$$Buckling\ force = \lambda_{min}(Reference\ load) \tag{5.6}$$

5.2.3 Configuration of graphene

Two geometric configurations for graphene monolayers need to be considered, namely the 'zig-zag' and 'arm-chair' configurations, which were both modelled in this study (see schematics in Fig.5.1). Boundary conditions were applied in such a way as to simulate a cantilevered graphene structure implying that the monolayer end opposite to the applied loading is rigidly supported. In addition to the 'zig-zag' and 'arm-chair' configuration, the analysis also considered different curvatures of graphene monolayers as defined in Fig.5.1(c) and also the effect of van der Waals forces. The radius of curvature for flat graphene monolayers as shown in Figs.5.1(a) and (b) was defined at infinity. The aspect ratio of a graphene sheet is defined as the ratio between the length-to-width dimensions of a graphene monolayer where length corresponds to the loading direction.

5.3 Results and discussion

Results for buckling analysis using the finite element based atomistic modelling approach considering graphene sheet aspect ratio, geometric configuration ('zig-zag', 'arm-chair'), curvature and effect of non bonding van der Waals forces are presented and discussed in the following sections.

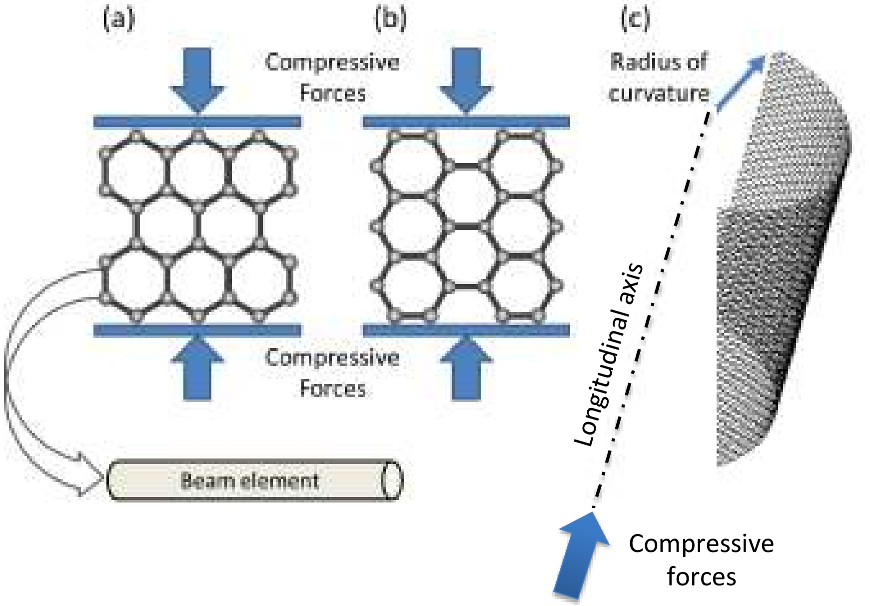

Fig.5.1 *Flat graphene monolayers in (a) zig-zag and (b) arm chair configuration and (c) curved graphene monolayer with compressive force along the longitudinal/ cylindrical axis.*

5.3.1 Aspect ratio effects for flat graphene sheets

Numerical analysis results pertaining to the aspect ratio effect for graphene sheets in ‘zig-zag’ configuration are shown in Fig.5.2. Graphene sheets with lengths ranging from 0.49 nm to 3.91 nm and width from 0.492 nm to 2.46 nm were modelled in this subsection. Plotted on a log-log scale the data appears as straight lines indicating an exponential decrease of buckling stability with aspect ratio. Upon further analysis of the data shown Fig.5.2 it becomes apparent that the buckling load per unit width is constant for a given sheet length.

Similar to the above the effect of aspect ratio was analysed for graphene sheets with ‘arm-chair’ configuration. For sheet lengths and widths ranging from 0.49 nm to 2.46 nm and 0.50 nm to 3.91 nm, analysis results are plotted in log-log scale in Fig.5.3. It can again be observed that buckling stability declines exponentially with increasing aspect ratio. Moreover, comparing data from Figs.5.2 and 5.3 for ‘zig-zag’ and ‘arm-chair’ configurations demonstrates that the ‘zig-zag’ configuration provides greater stability compared to the ‘arm-chair’ configuration (for example, see data points for the approximately square sheets (aspect ratio of unity) with ~0.5 nm width). Higher stability of the ‘zig-zag’ configuration is attributed to a bonding structure, i.e. beam elements that are aligned to a greater extent in the direction of applied loading.

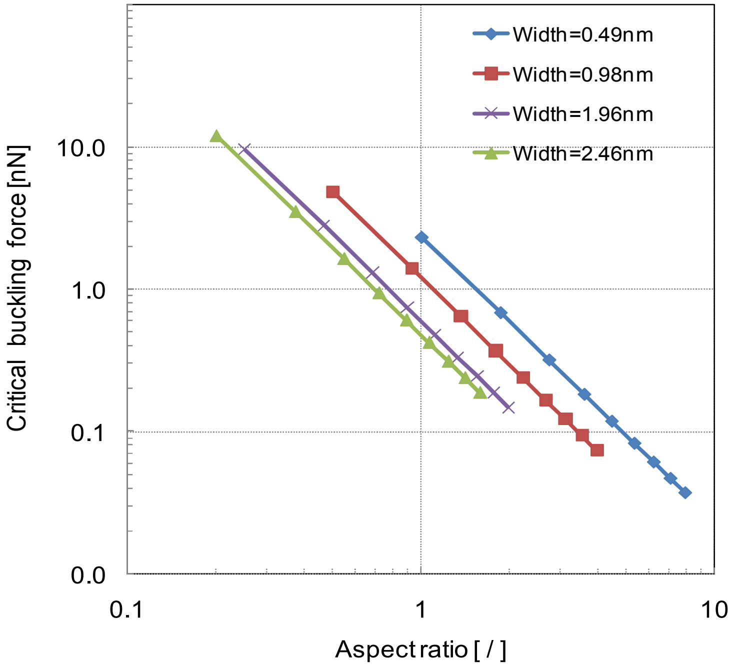

Fig.5.2 *Critical buckling force of flat graphene monolayers in zig-zag configuration for different sheet widths and aspect ratios.*

5.3.2 Effect of curvature on graphene sheet stability

Thus far, numerical analyses were performed for flat graphene sheets, i.e. with infinite radius of curvature. However, achieving a structure with perfectly flat graphene sheets is hardly possible due to non-bonding interactions such as van der

Waals forces. Hence, the effect of curvature is discussed in the present subsection. It can be inferred from the data plotted in Fig.5.4 for graphene monolayers with ‘zig-zag’ configuration and width of 2.46 nm that a curved profile improves buckling stability. Note that stability of graphene was found to increase with a decrease in radius of curvature up to approximately 5 nm; for even lower radii of curvature, buckling stability was observed to decline.

The effect of curvature was also investigated for graphene monolayers with ‘arm-chair’ configuration. Corresponding results are plotted in Fig.5.5. The data trend shown there is similar to the one obtained for the ‘zig-zag’ configuration, i.e. a decreasing radius of curvature is associated with an increase in buckling stability. However, for the ‘arm-chair’ configuration this effect is much less pronounced; in fact, it is rather insignificant. Hence, it can be concluded that sheet curvature only has an appreciable effect for graphene monolayers with ‘zig-zag’ configuration.

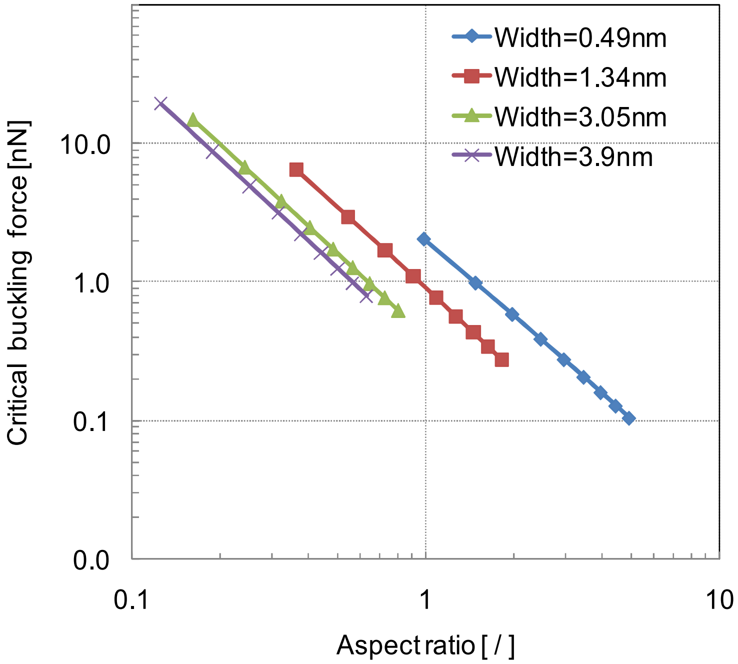

Fig.5.3 *Criticalbuckling force of flat graphene monolayers in arm chair configuration for different sheet widths and aspect ratios.*

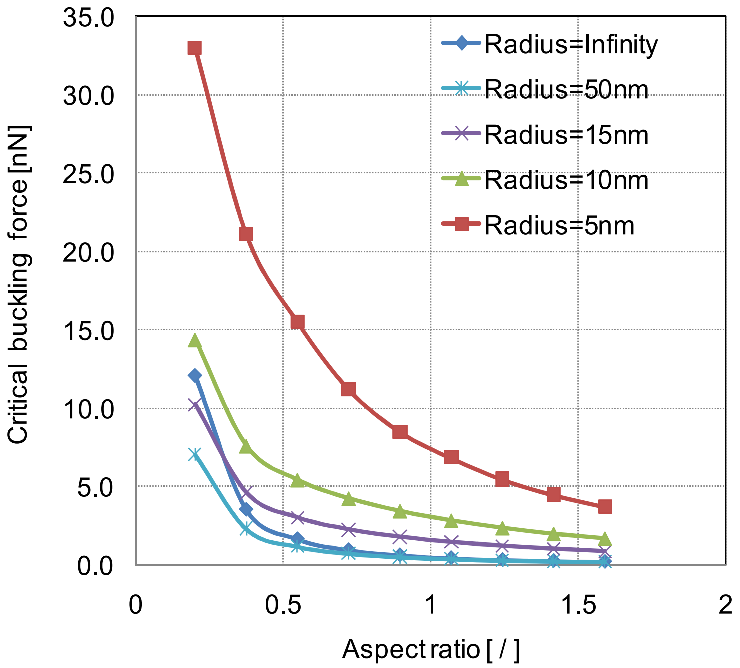

Fig.5.4 *Criticalbuckling force of graphene monolayers in zigzag configuration for different aspect ratios and radii of curvature.*

To enable further comparison, buckling stability for graphene monolayers with ‘zig-zag’ and ‘arm-chair’ configuration with a constant width of 8.1 nm and common radius of curvature of 5 nm were computed and plotted in Fig.5.6. It can be concluded from these results that graphene with ‘zig-zag’ configuration exhibits greater stability against buckling from compressive loading than the ‘arm-chair’ configuration. Higher buckling stability of the former is attributed to its bonding structure being aligned predominantly in the direction of applied loading.

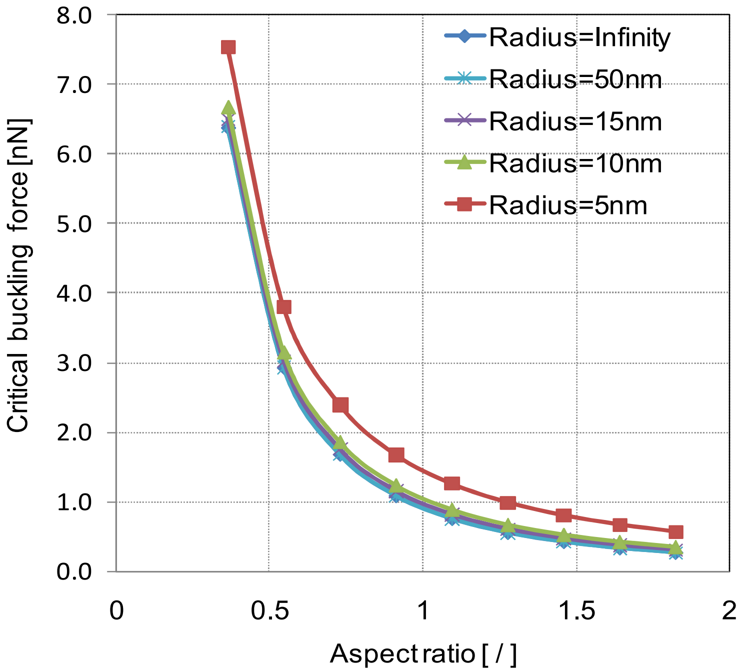

Fig.5.5 *Critical buckling force of graphene monolayers in arm chair configuration for different aspect ratios and radii of curvature.*

5.3.3 Effect of van der Waals forces on the buckling of graphene sheet[7]

As discussed, two different configurations for graphene ('zig-zag' and 'arm-chair') was considered during the finite element modelling. To investigate the effect of van der Waals forces, modelling was performed in two stages, first stage dealt with the influence of one or more graphene sheets on the buckling stability of a mono graphene sheet as shown in Fig.5.7. Second stage of investigation incorporates single, double and triple graphene sheets altogether to study their buckling stability in a group as shown in Fig.5.8. Interlayer spacing between the graphene sheets was investigated for their impact on the buckling phenomenon. Four different interlayer spacing of 0.344 nm (experimentally established

---

[7] A version of this section has been submitted for publication. A.Parashar and P.Mertiny 2012.Comput. Theor. Nanosci. (Accepted)

interlayer spacing), 0.3816 nm (spacing at which van der Waals forces become null), 0.425 nm (spacing with maximum van der Waals forces) and 0.500 nm (selected as maximum distance for modelling) were considered in the simulations. In the finite element model, dimensions of the ‘zig-zag’ configuration were kept fixed at 6.25 nm and 6.15 nm for length and width respectively, whereas for the arm-chair configuration length and width were flipped to 6.15 nm and 6.25 nm respectively.

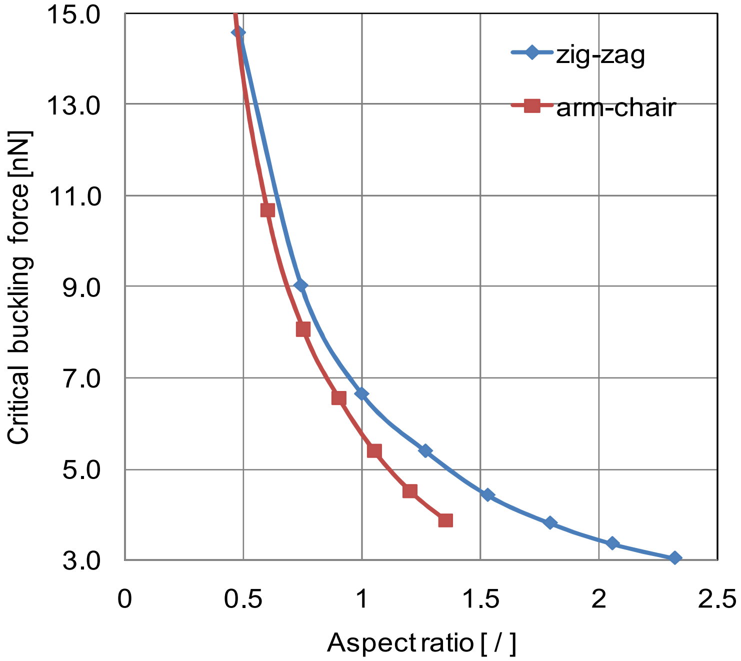

Fig.5.6 *Critical buckling force of graphene monolayers in zigzag and arm chair configuration with a constant width of 8.1nm and a common radius of curvature of 5 nm for different aspect ratios.*

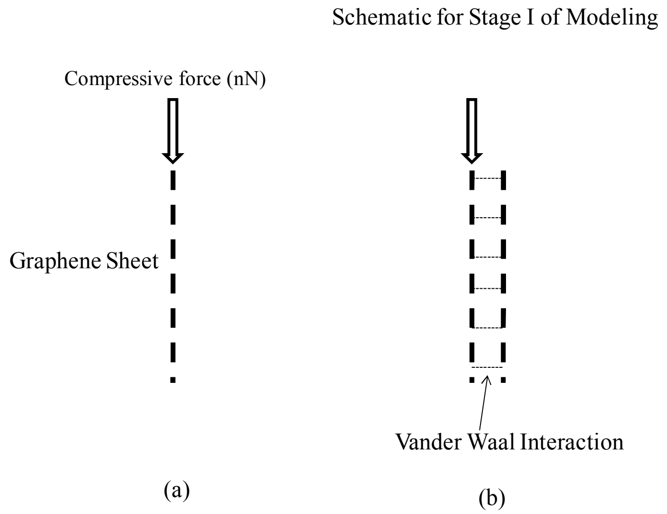

Fig.5.7 *Schematic of boundary conditions employed during the first stage of modelling (a) mono and isolated graphene sheet (b) mono graphene sheet in presence of another graphene sheet (c) mono graphene sheet in presence of two more graphene sheet on either side.*

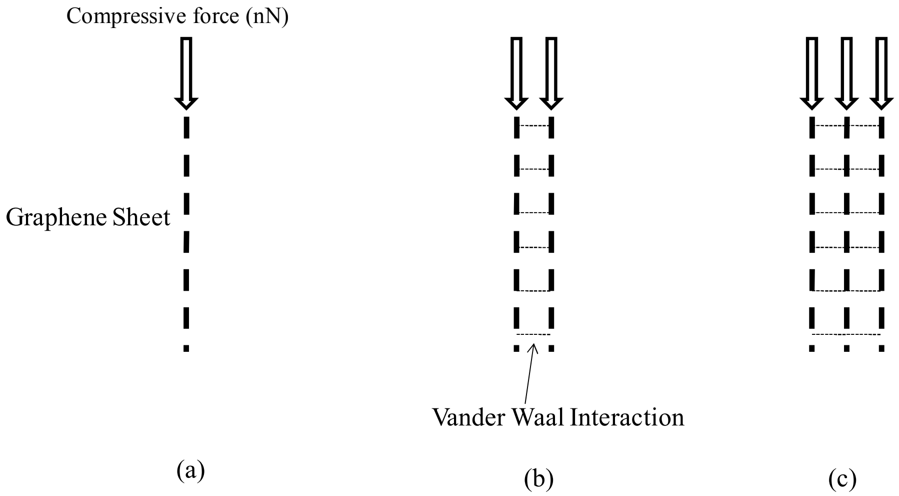

Fig.5.8 *Schematic of boundary condition employed during the second stage of modelling (a) Mono graphene sheet (b) Twin graphene sheets subjected to compressive loading (c) Triple graphene sheets subjected to compressive loading.*

Zig-zag configuration:

Results obtained for the stage I boundary conditions are depicted inFig.5.9. The buckling stability of an isolated mono graphene sheet (shown in Fig.5.7(a)) were compared with the buckling stability of graphene when accompanied with one or more graphene sheets on either of its sides as shown in Fig.5.7(b and c) respectively.

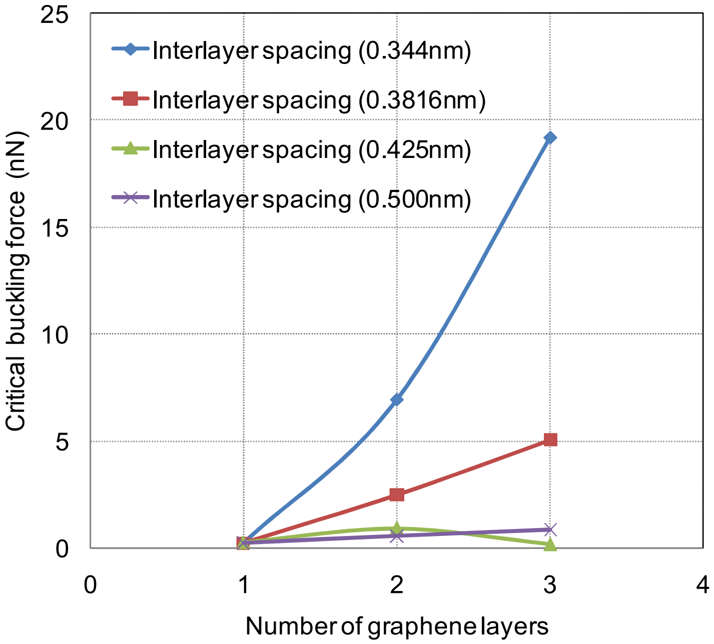

Fig.5.9 *Critical buckling force of single graphene sheets with zigzag profile under the influence of other graphene sheets.*

As discussed in previous sections, modelling was performed with uniformly spaced graphene sheets. It can be observed from Fig.5.9 that the isolated mono graphene sheet exhibits the minimum values for the critical buckling force, whereas a linear increase in buckling stability was observed with increasing number of graphene sheets employed in stage I of modelling. It was also observed that interlayer spacing between sheets played a significant role in deciding the overall buckling stability of graphene. The maximum buckling stability was observed when interlayer spacing was kept at 0.344 nm; any further increase in interlayer spacing reduced the buckling stability of the mono graphene sheets under consideration. The effect of non-bonded van der Waals interaction forces was found to be negligible for the buckling stability of mono graphene sheets at an interlayer spacing of 0.425 nm and 0.5 nm.

According to the boundary conditions shown in Fig.5.8, significant improvements in overall buckling stability are shown in Fig.5.10 when two or three graphene sheets were jointly tested for their unified buckling stability. At an interlayer spacing of 0.425 nm and 0.500 nm no significant improvement in buckling stability of multiple graphene sheets were observed as compared to isolated mono graphene sheet.

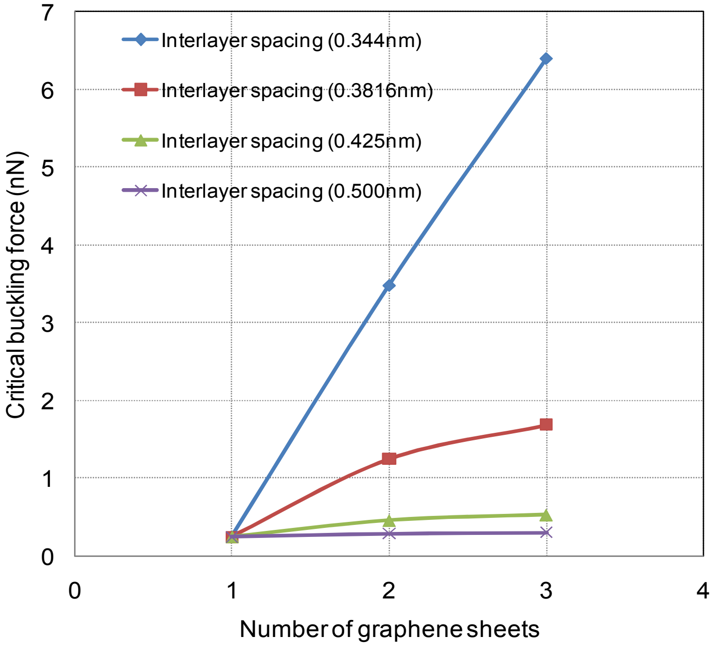

Fig.5.10 *Critical buckling force of multiple graphene sheets with zig-zag profile connected with non-bonded interactions.*

Arm-chair configuration:

In this subsection of modelling the 'arm-chair' configuration of graphene was simulated using finite elements to investigate the buckling stability of single as well as multiple graphene layers according to the boundary conditions defined in Figs.5.7 and 5.8 respectively. In Fig.5.11 results for stage I boundary conditions (defined in Fig.5.7) are plotted.

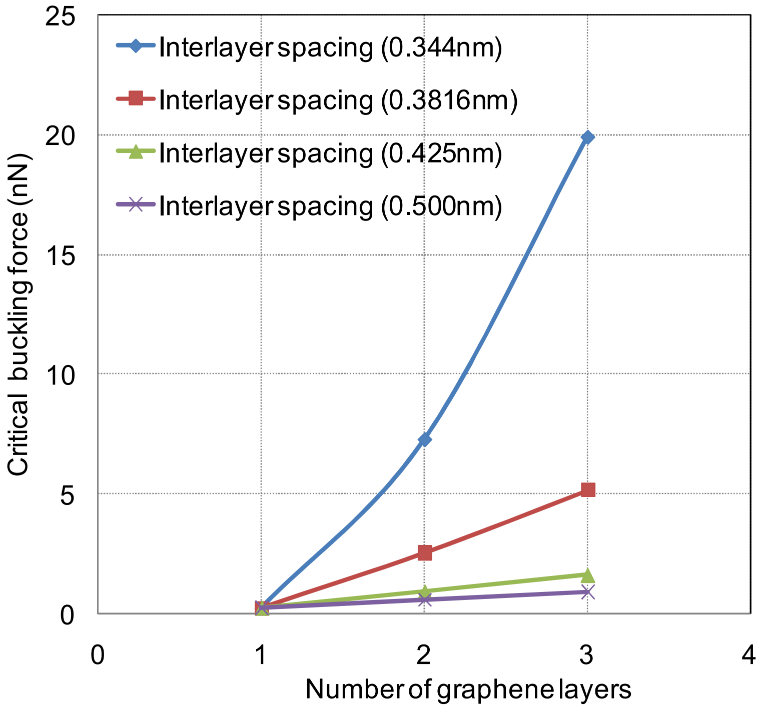

Fig.5.11 *Critical buckling force of single graphene sheets with arm chair configuration under the influence of van der Waals interactions.*

Results plotted in Fig.5.11 indicate the same trend as observed for graphene sheets with zig-zag configuration. A linear increase in graphene sheet buckling stability was obtained when it was accompanied with more sheets on either of its sides as shown in Fig.5.7. Once again, interlayer spacing between graphene sheets emerged as an important parameter for the buckling stability of mono graphene sheets. At an interlayer spacing of 0.344 nm and 0.3816 nm significant improvements in mono graphene sheet critical buckling stability was observed, whereas any further increase in interlayer spacing resulted in decreasing interaction between the sheets and reduced buckling stability.

In this last subsection of modelling, graphene with armchair configuration was investigated for its buckling stability under the influence of boundary conditions as shown in Fig.5.8. A significant improvement in buckling stability was observed in Fig.5.12 for an interlayer spacing of 0.344 nm. It can be concluded from the above results that interlayer spacing of 0.344 nm has the maximum stability under the influence of compressive loading which is also the experimentally established interlayer spacing in graphene. The effect of van-der Waals interaction forces was found to be more prominent in stage I of the modelling as compared to the stage II boundary conditions. The effect of van der Waals interaction forces was found to be independent of graphene configurations.

5.4 Conclusions

The finite element based atomistic model proposed in the previous chapter was successfully expanded in this chapter for the study of buckling stability of graphene sheets. Finite element based atomistic modelling was performed in this study to investigate the effects of dimensional and geometrical parameters on the buckling stability of graphene monolayers. Modelling results indicate that the buckling stability of graphene monolayers decreases significantly with increasing aspect ratio, where the latter is defined as the length-to-width ratio with the applied compressive buckling load acting in the length direction. This phenomenon was observed for both possible graphene lattice orientations, which herein were termed ‘zig-zag’ and ‘arm-chair’ configuration. Numerical analysis was also conducted with respect to the radius of curvature of graphene monolayers. Results from these analysis showed that higher buckling stability is achieved for graphene sheets with a curved profile. It was also established by this study that a graphene 'zig-zag' configuration exhibits greater stability against buckling than graphene with 'arm-chair' configuration. Through this study also the expedience of the developed finite element based atomistic model was demonstrated, which has the capability to assess the elastic response of graphene structures with low numerical cost.

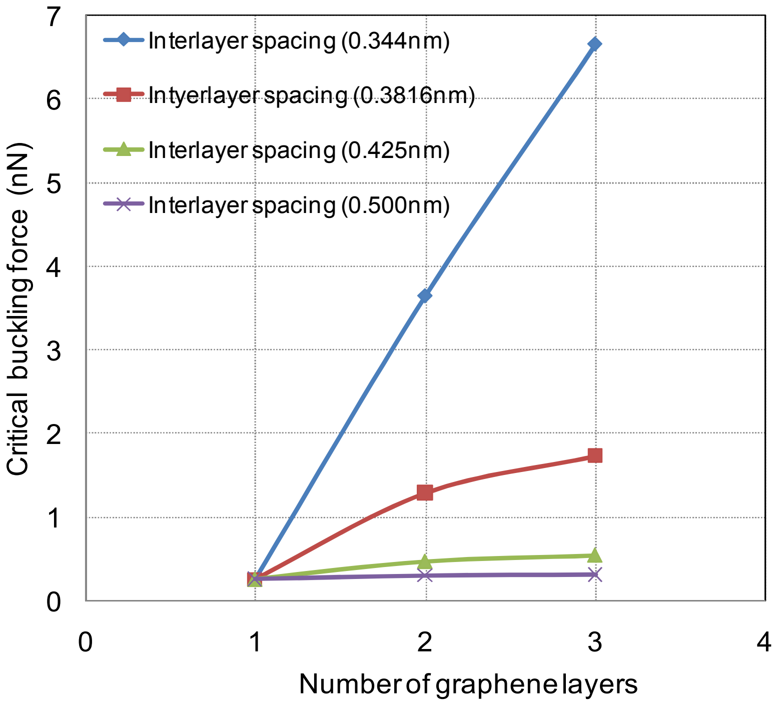

Fig.5.12 *Critical buckling force of multiple graphene sheets with arm chair configuration connected with van der Waals interactions.*

Significant effects of van der Waals forces on the buckling stability of multiple graphene sheets were found. It was concluded from the analysis that significant improvements in the buckling stability occurred at interlayer spacings of 0.344 nm and 0.3816 nm, whereas the influence of grouping of graphene sheets was negligible at higher interlayer spacings of 0.425 nm and 0.500 nm.

The proposed atomistic modelling technique for graphene has further been employed for multiscale modelling, which is discussed in subsequent chapters.

Van der Waals interaction forces as studied in phase II of this research project were found to provide a significant load transfer mechanism between graphene and polymer.

5.5 Bibliography

1. J.P.Wilber, C.B.Clemons, G.W.Young, *Continuum and atomistic modelling of interacting graphene layers*, Phys. rev. B: condens. matter. 75 (**2007**) 045418.
2. A.Sakhaee-Pour, *Elastic buckling of single-layered graphene sheet*, Comput. mater. sci. 45 (**2009**) 266-270.
3. S.C.Pradhan, *Buckling of single layer graphene sheet based on nonlocal elasticity and higher order shear deformation theory*, Phys. lett. A. 373 (**2009**) 4182-4188.
4. Z.Waszczyszyn, C.Cichon, M.Radwanska, *Stability of Structures by Finite Element Methods*, Elsevier, Amsterdam, **1994**.

Phase III (Multiscale analysis)

The scope of Phase III of this research study is as follows:

- Study of the effect of graphene as a nanofiller on the fracture toughening mechanism of developed nanocomposite.
- Investigate the buckling behaviour in graphene nanocomposite using the multiscale modelling approach.

Work as part of Phase III has previously been presented in the form of peer reviewed journal publications:

Avinash Parashar and Pierre Mertiny, *Buckling behaviour of graphene/polymer nanocomposite with a non-bonded interphase* .Nanoscale. Res.Lett. **2012**, 7:515.

Avinash Parashar and Pierre Mertiny, *Multiscale model to investigate the effect of graphene on the fracture characteristics of graphene/polymer nanocomposites*. Nanoscale. Res. Lett. **2012**,7:595.

Avinash Parashar and Pierre Mertiny, *Multiscale model to study fracture toughening in graphene/polymer nanocomposites*.Int.J.Frac.**2012**. (10.1007/s10704-012-9779-y).

Chapter 6

Multiscale Modelling to Study the Impact of Graphene Reinforcement on the Stability of Epoxy under Compressive Loading[8]

6.1. Introduction

The third phase of this research project, which commences with this chapter, discusses the impact of graphene on the mechanical properties of reinforced epoxy (adhesive). It was shown in the first phase of this research, i.e. Chapters 2 and 3 on dimensional scaling of adhesively bonded composite pipe section, that a shift occurs in the region susceptible to failure from composite pipe to isotropic epoxy based adhesive. On this basis it was proposed to enhance joint strength by reinforcing the adhesive material with a nanofiller. Based on its superior mechanical properties and economical aspects, graphene was selected as the nano-reinforcing agent for this research project. Before exploring the reinforcing effect of graphene on the mechanical properties of epoxy, an intermediate second phase was prepared as described in Chapters 4 and 5. This second phase was designed exclusively to explore and develop the numerical modelling for characterizing graphene as well as to study the significance of van der Waals forces as load transfer medium.

In the recent past graphene has emerged as a potential candidate for developing nanocomposites with improved properties [1,2]. The experimental characterization of graphene/polymer nanocomposites is a challenging process, and hence, computational approaches for predicting the behaviour of such materials have also extensively been employed. Various multiscale models are

---

[8] A version of this chapter has been published. A.Parashar and P.Mertiny 2012. Nanoscale Res.Lett. 7: 515

available in the literature for predicting the properties of carbon nanotube (CNT) based nanocomposites [3-5], but very few models have been presented to study graphene nanocomposites. For example, Cho et al. [6] developed a numerical model in conjunction with a Mori-Tanaka approach to study the elastic constants of randomly distributed graphene in polymer. Awasthi and his team [7] investigated the load transfer mechanism between polyethylene and graphene sheets. Montazeri and Tabar [8] developed a finite element (FE) based multiscale model to investigate the elastic constants of graphene based nanocomposites.

Buckling in isolated graphene sheets was modelled by several researchers [9-11]. However, buckling stability of graphene/polymer nanocomposites was only reported by Rafiee et al. [12]. Using an experimental and analytical approach, up to 50% and 32% improvement in the buckling stability of nanocomposites was reported respectively. In the analytical approach, an Euler buckling formulation was employed, and elastic properties required in the Euler equation were estimated by experimental means. Discrepancies between the two buckling stabilities were attributed to scaling issues.

It is well established that the reinforcement of polymer with graphene increases the elastic modulus of the material, which further improves buckling stability. The aim of this study is to propose a numerical model, which can estimate the increase in buckling stability with different volume fractions of graphene and can further be extended to complex shapes and structures. Proposed multiscale model helps in evaluating the effect of graphene nanofiller on one of the mechanical properties of developed nanocomposite.

It has been reported that achieving a uniform dispersion of two-dimensional graphene sheets in polymer is more challenging compared to the mixing of one-dimensional CNT. Moreover, the application of nanocomposites is not limited to simple structures, and the comprehension of material behaviour in complex structures is restricted when employing experimental and analytical methods. Consequently, research efforts are increasingly focused on numerical approaches.

To overcome some of the limitations that exist in experimental and analytical work a multiscale representative volume element (RVE)is proposed in this work to investigate buckling phenomena in graphene/polymer nanocomposites under the assumption that graphene is uniformly distributed in the polymer. To the knowledge of the present authors, no numerical model has been reported yet to study the effect of graphene on the buckling stability of nanocomposites. In the proposed technique graphene was modelled in the atomistic scale, whereas polymer deformation was analyzed as a continuum.

6.2 Finite element modelling of RVE

In this chapter a finite element technique was employed in conjunction with molecular and continuum mechanics to simulate buckling in graphene/polymer nanocomposites. In the proposed RVE, the polymer, epoxy in this case, was modelled as a continuum phase whereas the deformation in graphene was evaluated using an atomistic description. Non-bonded interactions were considered as the load transfer mechanism or interphase between polymer and graphene. FE modelling was performed in the ANSYS (Version 13) software environment.

6.2.1 Atomistic model for graphene

To model graphene in the proposed RVE, it was assumed that graphene behaves like a space frame structure, in which covalent bonding between C-C atoms constitutes the load bearing element while atoms act like a joint. Modelling of graphene in multiscale model was performed according to description provided in the section 4.2.2.

6.2.2 Continuum model for polymer

The volume filler fraction of graphene in polymer ranges commonly up to 10%. Most of the material volume is therefore occupied by polymer. Simulating the polymer phase on the atomistic scale would require large efforts in dealing with large numbers of degrees of freedom as well as substantial computational cost. Therefore, as a reasonable compromise, the polymer phase was modelled as a continuum, and three-dimensional SOLID45 elements were used for meshing the geometry. Epoxy with a Young's modulus of 3.4 GPa and a Poisson's ratio of 0.42 was considered for the polymer material in the present work.

6.2.3 Interphase between graphene and polymer

In this phase of the research project, non-bonded interactions were considered as load transfer mechanism between the polymer and graphene. Naturally, load transfer between non-functionalized graphene sheets and polymer takes place through the van der Waals interactions. The Lennard Jones "6-12" potential given in Equation 6.1 was employed to estimate the properties for the interface region, which is depicted in the schematic in Fig.6.1.

$$U(r) = 4\gamma\left[\left(\frac{\varphi}{r}\right)^{12} + \left(\frac{\varphi}{r}\right)^{6}\right] \tag{6.1}$$

where *r* is the atomistic distance between atoms, φ (0.34nm) is the hard sphere radius and γ (0.556kcal/mole) is potential well depth. In the finite element environment these non-bonding interactions were modelled with the help of LINK8 truss elements. As shown in Equation 6.2 properties for those truss elements were estimated by comparing classical continuum strain energy of truss elements with the Lennard Jones "6-12" potential. Note that the truss model described herein was earlier employed by Li and Chou [13] to simulate the interaction between CNT and epoxy polymer. Similar to earlier published work with mutlitscale models[8,13] it was assumed that the bulk properties of epoxy at the interphase remain unaffected in the presence of graphene.

$$E(r) = \frac{8\gamma R_{Eq}}{A\left(r - R_{Eq}\right)^2}\left[\left(\frac{\varphi}{r}\right)^{12} + \left(\frac{\varphi}{r}\right)^{6}\right] \tag{6.2}$$

whereR_{Eq} is the initial un-deformed length, r is the deformed length, A is the cross sectional area, and $E(r)$ is the Young's modulus of the truss element.

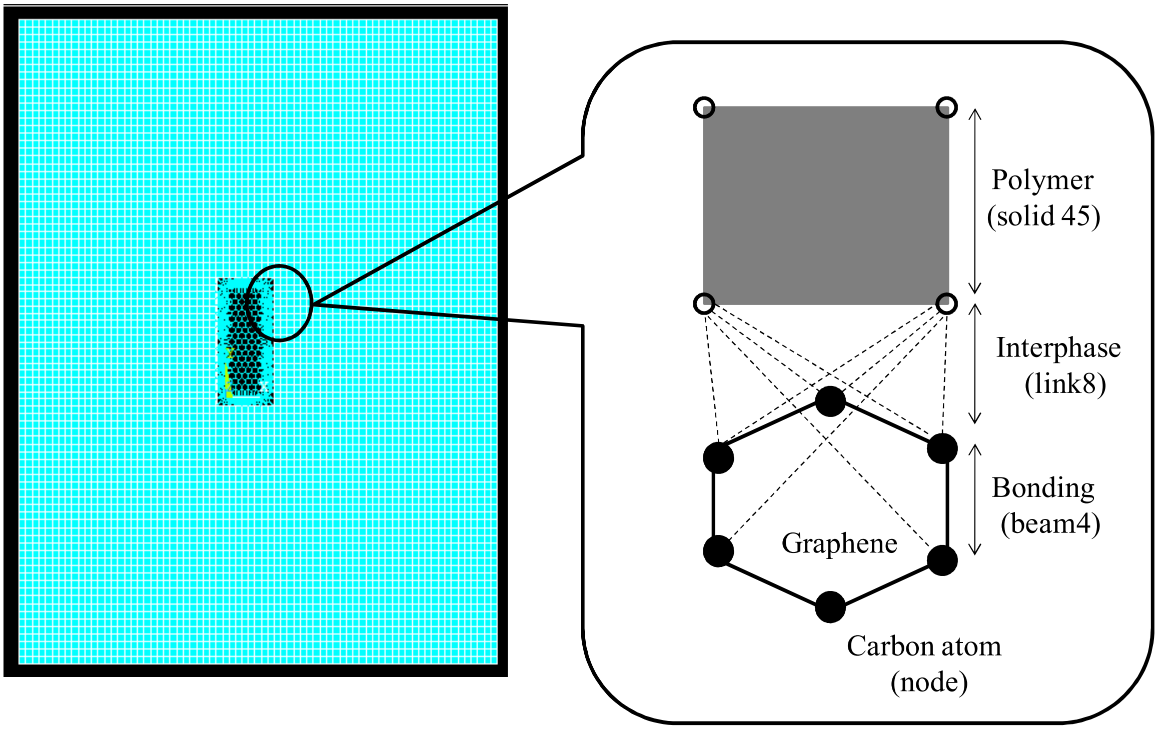

Fig.6.1 *Schematic of multiscale model.*

6.2.4 Eigenvalue buckling analysis

A linear analysis for mode one buckling was performed in this chapter, which is associated with the computation of a bifurcation load and corresponding buckling mode. The fundamentals underlying this section are same as the ones discussed in Section 5.2.2.

6.3 Results and analysis

The proposed RVE was employed to understand the buckling behaviour of graphene in a polymer matrix when graphene was assumed to be uniformly distributed. A second separate RVE structure with equal dimensions was developed using finite element modelling to study the buckling in neat (homogenous) polymer.

To validate the results of the proposed RVE, an alternative method (indirect method) was also employed in this work. The proposed RVE model with boundary conditions as shown in Fig.6.2 was first used to estimate the Young's modulus of the RVE as a whole for various volume fractions of graphene. The estimated material properties (*E*) were then used in defining the homogenous rectangular plate with dimensions of the proposed RVE model. Buckling loads were calculated for this homogenous rectangular plate shown in Fig.6.3(a) and were compared with the direct approach defined in Fig.6.3(b).

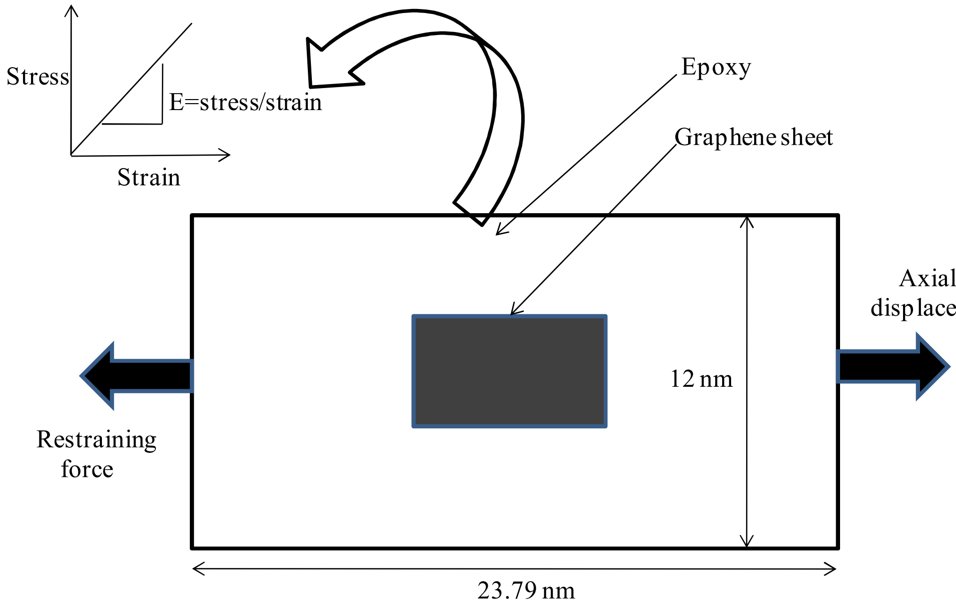

Fig.6.2 *Schematic of model and boundary condition for estimating Young's moduli of developed RVE with different filler volume fractions.*

The analytical formulation to estimate the buckling load for a rectangular plate is given in Equation 6.3, where P_x is the applied unidirectional compressive load, w is the displacement in the outward normal direction, and D is flexural rigidity (i.e. a function of the Young's modulus). Boundary conditions were kept identical in all RVE models. Only the value of flexure rigidity was varied, which afforded the proposed RVE model the capability of yielding E for different graphene volume fractions.

$$D\nabla^4 w(x,y) + P_x \frac{\partial^2 w}{\partial^2 x} = 0 \tag{6.3}$$

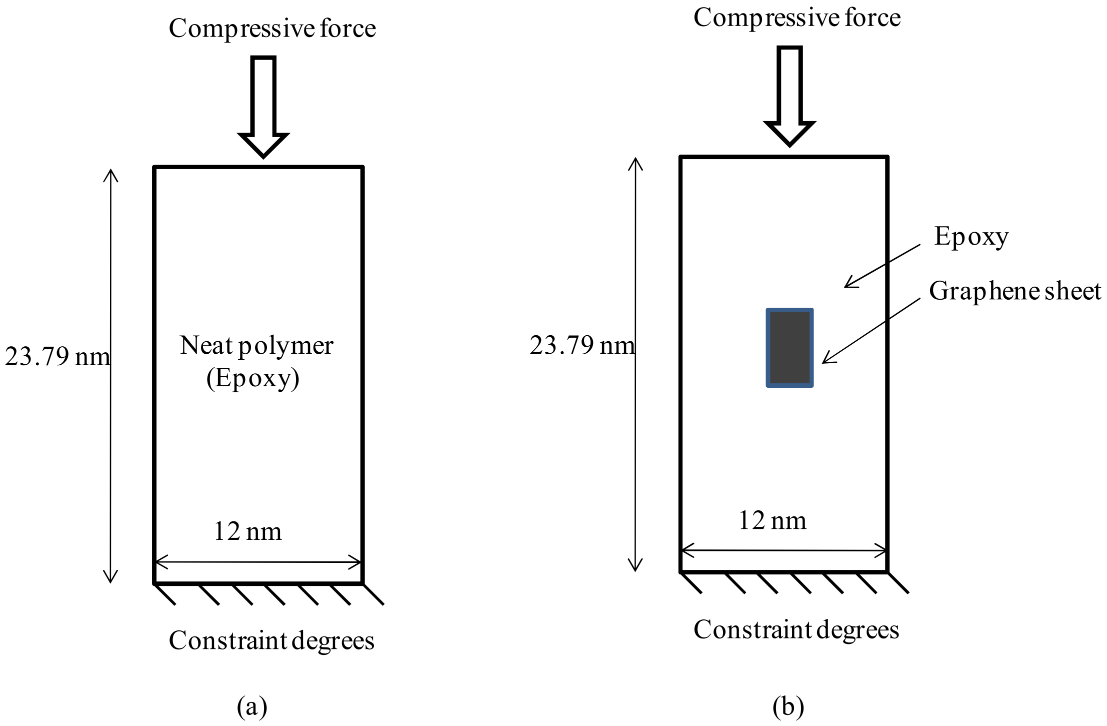

Fig.6.3 *Boundary conditions and dimensions for (a) Neat polymer model and (b) Multiscale graphene/polymer model.*

Boundary conditions along with dimensions for the proposed RVE model are shown in Fig.6.3. The thickness of graphene in the atomistic scale and for epoxy as a continuum phase was kept constant at 0.344 nm, whereas the thickness of the interphase was kept at 0.172 nm according to [14].

The graphene volume fraction in the proposed RVE model was varied by changing the size of the graphene sheet, leading to graphene volume fractions ranging from 2% to 6%. Filler volume fractions of reasonable and practical magnitude were thus studied omitting agglomeration effects in graphene nanocomposites with high filler content.

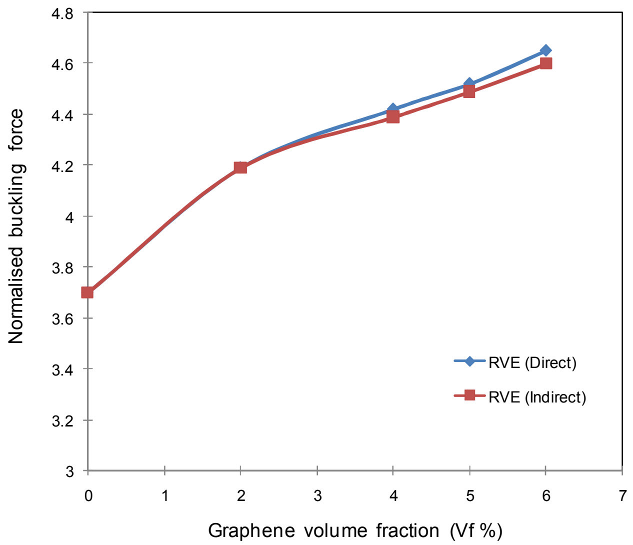

Fig.6.4 *Normalized buckling force estimated from multiscale modelling for graphene/polymer nanocomposites. Ordinate data was normalized by dividing the critical buckling force by* 10^{-2}*nN.*

Results obtained from the developed RVE structures were plotted in Fig.6.4. These data show a significant improvement in the buckling performance of nanocomposites under compressive loading. The buckling performance of neat epoxy (represented by the RVE defined in Fig.6.3a) was herein considered the reference level. The buckling forces calculated from the direct and indirect approach are in good agreement, which validates the proposed numerical technique. In the current work upto 26% improvement in the buckling performance over the neat epoxy sheet was estimated for only 6% volume fraction of graphene.

6.4 Conclusions

In this study a representative volume element method was successfully employed to investigate the buckling phenomenon in graphene/polymer nanocomposites, where graphene was assumed to be uniformly distributed. Graphene was modelled in the atomistic scale and polymer as a continuum. A significantly enhanced buckling performance of graphene reinforced polymers was observed as compared to neat polymer, i.e. buckling performance of graphene/polymer nanocomposite improved by 26% with only 6% filler volume fraction.

6.5 Bibliography

1. M.A.Rafiee, J.Rafiee, I.Srivastave, Z.Wang, H.Song, Z.Z. Yu, N.Koratkar, *Fracture and fatigue in graphene nanocomposites*. Small 6(**2010**) 179-183.
2. M.A.Rafiee, J. Rafiee, Z.Wang, H.Song, Z.Z.Yu, N. Koratkar, *Enhanced mechanical properties of nanocomposites at low graphene content*. ACS Nano 3(**2003**) 3884-3890.
3. M.R.Ayatollahi, S.Shadlou, M.M.Shokrieh, *Mutiscale modelling for mechanical properties of carbon nanotube reinforced nanocomposites subjected to different types of loading*, Compos.Struct. 93(**2011**) 2250-2259.

4. S.A.Meguid, J.M.Wernik, Z.Q.Cheng, *Atomistic based continuum representation of the effective properties of nano-reinforced epoxies*, Int. J. Solids Struct. 47(**2010**) 1723-1736.
5. G.M.Odegard, T.S.Gates, K.E.Wise, C.Park, E.Siochi, *Constitutive modelling of nanotube reinforced polymer composites*, Compos. Sci. Technol. 3(**2003**)1671-1687.
6. J.Cho, J.J.Luo, I.M.Daniel, *Mechanical characterization of graphite/epoxy nanocomposites by multi-scale analysis*, Compos. Sci. Technol. 67(**2007**) 2399-2407.
7. A.P.Awasthi, D.C.Lagoudas, D.C.Hammerand, *Modelling of graphene polymer interfacial mechanical behaviour using molecular dynamics*. Modell.Simul. Mater. Sci. Eng. 17(**2009**) 31-37.
8. A.Montazeri, H.R.Tabar, *Multiscale modelling of graphene and nanotube based reinforced polymer nanocomposites*, Phys.Lett. A 375 (**2011**) 4034-4040.
9. C.Q.Ru, *Effect of van der Waals forces on axial buckling of double walled carbon nanotube*. J.Appl.Phys.87(**2000**) 7227-7231.
10. S.C.Pradhan, *Buckling of single layer graphene sheet based on nonlocal elasticity and higher order shear deformation theory*, Phys.Lett. A 373 (**2009**) 4182-4188.
11. A.S.Pour, *Elastic buckling of single-layered graphene sheet*, Comput. Mater. Sci. 45(**2009**) 266-270.
12. M.A.Rafiee, J. Rafiee, Z.Z. Yu, N. Koratkar, *Buckling resistant graphene nanocomposites*. Appl. Phys.Lett. 95(**2009**) 223103-1:3
13. C.Li, T.W.Chou, *Multiscale modelling of compressive behaviour of carbon nanotube/polymer composites*, Compos. Sci. Technol. 66 (**2006**) 2409-2414.

Chapter 7

Multiscale Model with Non-Bonded Interphase to Study Fracture Toughness Mechanism in Graphene/Polymer Nanocomposites[9]

7.1 Introduction

The multiscale model discussed in the previous chapter was further enhanced to study fracture-toughening mechanisms in graphene nanocomposites. In Phase I of the research project, the adhesive bondline was identified as the weakest link in the adhesively bonded FRP pipe sections. This third and final phase of the research project is thus concerned with studying methods for the mitigating those weaknesses with the help of nanofillers.

The two-dimensional configuration of graphene poses complex challenges for experimental investigation of graphene nanocomposites. Hence, in this research project finite element based modelling technique has been employed to study fracture toughness mechanism in such nanocomposites.

Rafiee et al. in the published experimental work [1-2], reported significant increase in the fracture toughness of graphene-modified epoxy nanocomposites. They reported in their work that the addition of graphene sheets into the epoxy matrix resulted in a distinct increase in fracture toughness, i.e. fracture toughness of epoxy was increased by up to 65% with an inclusion of 0.125% weight fraction of graphene [1]. It was also reported in their experimental work that uniform distribution of graphene sheets in an epoxy matrix remains a challenging undertaking, which currently limits the full understanding of the mechanisms behind the property improvements. Hence, modelling is considered as a viable

---

[9] A version of this chapter has been accepted for publication. A.Parashar and P.Mertiny 2012. Nanoscale Res. Lett.

alternative to explore the effects of nanofiller dispersion on the fracture properties of polymer nanocomposites.

The number of theoretical/numerical works published on graphene nanocomposites has so far been limited. Existing works in this field are, for example, the molecular dynamics based simulation techniques employed by Awasthi et al. [3], who studied the load transfer mechanisms between polyethylene and a graphene sheet. Cho et al. [4] employed a Mori-Tanaka approach to study the elastic constants of nanocomposites with randomly distributed graphene sheets. Most recently, Montazeri and Tabar [5] developed a multiscale finite element model to study the elastic constants of a graphene based polymer nanocomposite.

To the author's knowledge, no theoretical studies are available in the technical literature on the fracture behaviour of graphene/polymer nanocomposites. In the present chapter an attempt has been made to develop a multiscale model to investigate the fracture characteristics of graphene-modified epoxy nanocomposites. The proposed multiscale modelling technique was developed in a finite element environment in conjunction with the virtual crack closure technique (VCCT). A multiscale approach employing the VCCT provides an efficient numerical analysis scheme in terms of the involved degrees of freedom. As a consequence, the analysis can be performed with the widely available computational systems.

7.2 Details of multiscale modelling

In the present work, considering the polymer matrix and graphene nano-filler as a continuum and atomistic phase respectively, a multiscale model of finite elements was developed. The bond interaction between carbon atoms in graphene was simulated with the help of beam elements. In the current finite element simulation, the modified Morse potential was employed to model bonded interaction between C-C bonds. The Morse potential has already been applied in number of research works [6, 7], where structures were subjected to large strain values.

According to the modified Morse potential, the potential energy of the isolated graphene sheet can also be expressed as a sum of the bond stretching component (E_{S}) and the angle bending component (E_{B}) as given in Equations 7.1-7.3.

$$E = E_{\mathrm{S}} + E_{\mathrm{B}} \tag{7.1}$$

$$E_{\mathrm{S}} = D_{\mathrm{e}}\left\{\left[1 - \exp^{-\beta\varepsilon r}\right]^2 - 1\right\} \tag{7.2}$$

$$E_{\mathrm{B}} = \frac{1}{2}k_{\theta}(\theta - \theta_{\mathrm{o}})^2[1 + k_{\mathrm{sextic}}(\theta - \theta_{\mathrm{o}})^4] \tag{7.3}$$

The parameters included in Equations 7.1-7.3 are summarized in Table 7.1 and can also be found in [8].

In the current research project, the bond-stretching component dominates the overall bond energy and therefore, the angle-bending component was neglected in the simulation. The inter-atomic force acting between the two C-C atoms can be explored by differentiating Equation 7.2 to give

$$F = 2\beta D_{\mathrm{e}}\left(1 - \exp^{-\beta\varepsilon r_o}\right)\exp^{-\beta\varepsilon r_o} \tag{7.4}$$

Elastic beam elements ‘Beam 4’ were employed in this work to simulate C-C bond strength. The cross-sectional area of each beam element was estimated as 0.09079 nm^2 (the diameter of each beam element was considered equal to the thickness of graphene sheet, that is, 0.34 nm), which was further employed in conjunction with Equation 7.4 to model the non-linear stress-strain behaviour of C-C bonds (plotted in Fig.7.1). From the initial slope of data plotted in Fig.7.1, the initial stiffness of C-C bonds was assigned as 1.33TPa.

Table 7.1 *Modified Morse potential variables and parameters*

Parameter	**Value**	**Description**
r (m)	-	Length of C-C bond
r_o(m)	0.1421x10^{-9}	Equilibrium C-C bond distance in graphene
ε	$(r - r_o)/ r_o$	Strain in C-C bond
D_e(Nm)	6.03105x10^{-19}	Dissociation energy
β (m^{-1})	2.625x10^{10}	Constant controlling the 'width' of the potential
θ (rad)	-	Current angle of the adjacent bond
θ_o (rad)	2.094	Initial angle of the adjacent bond
k_θ (Nm/rad^2)	0.9x10^{-18}	Force constant for bond bending
k_{sextic} (rad^{-4})	0.754	Constant in bending term of potential

The continuum phase (polymer) of the multiscale model as shown in Fig.7.2 was meshed with a three-dimensional continuum element (SOLID45). The continuum phase was modelled with a Young's modulus of (E = 3.4GPa) and with a value of 0.42 for Poisson's ratio. In general, the continuum mesh size in such multiscale models was kept to the same size as the individual cell in graphene/CNT, but in this chapter a more specific approach was employed. To formulate the interphase between the graphene and polymer, meshing of the continuum phase in the interphase region was done with a specific mapped mesh density. In the research work published in [9], epoxy was modelled as polymer chains, where the spacing between the chains was kept at 0.3816 nm, which is equilibrium spacing with respect to van der Waals forces. According to the above justification, the element

(SOLID45) thickness and width was kept at 0.3816 nm, which is same as the equilibrium distance in van der Waals interactions. The element size along the length of the representative volume element RVE (see Fig.7.4) was kept at 0.125 nm. The specified element density was kept in the near vicinity of the graphene/polymer interphase up to a distance of 0.85 nm from the graphene edge, whereas different mesh specifications were employed to mesh the region containing the crack plane.

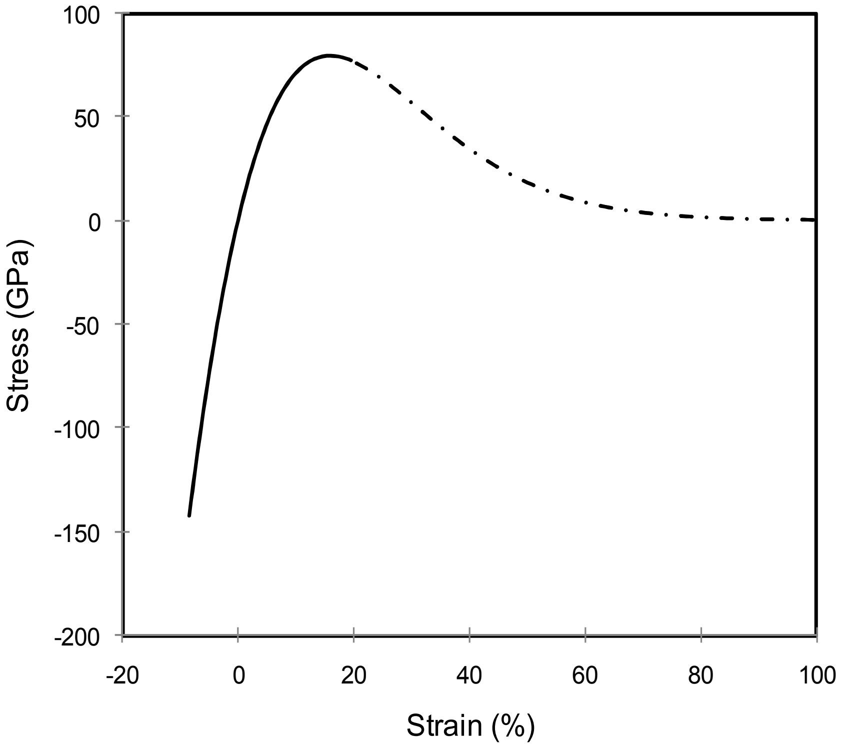

Fig.7.1 *Non-linear stress/strain relation for C-C bond developed from modified Morse potential*

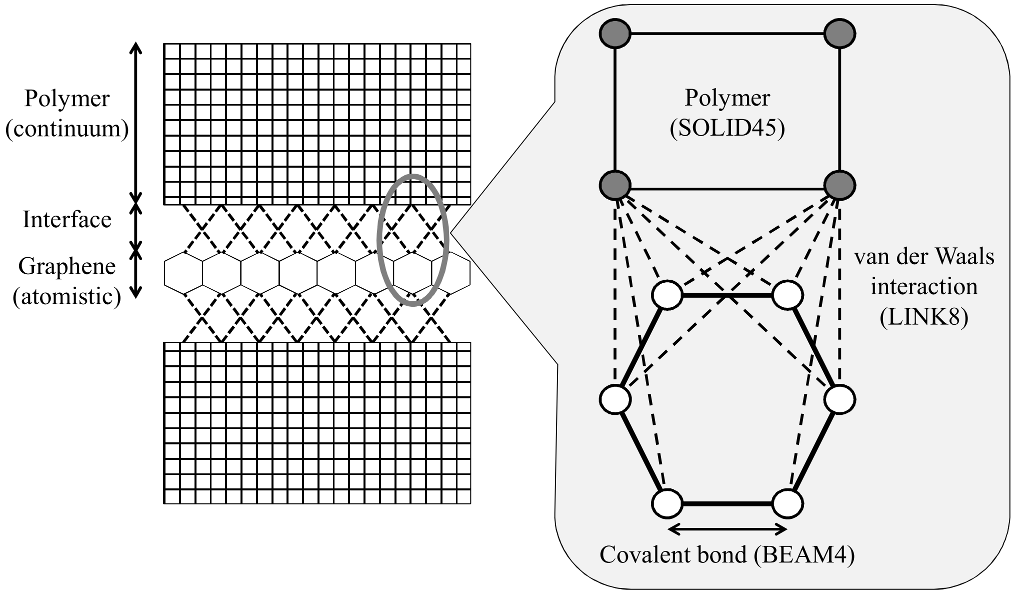

Fig.7.2 *Schematic of multiscale model.*

The most significant part of the proposed multiscale model is the interphase region between the atomistic graphene model and the continuum polymer representation (see Fig.7.2). A number of approaches have been considered to account for the interfacial properties and thickness. These depend on the type of bonding, i.e. functionalised or non-functionalised bonding, as well as on the load transfer mechanism through the interface. Hence, the interfacial properties have not unambiguously been defined yet. Hu et al. [10], in their work on polystyrene and carbon nano tubes (CNT), considered van der Waals interactions to be responsible for maintaining interfacial strength. They assumed 0.2851 to 0.5445 nm as the interface thickness. Meguid et al. [9] simulated the interaction between the CNT and polymer chains with an interfacial thickness of 0.3816 nm. In the present work, the interfacial thickness was set to 0.172 nm, which is consistent with the numerical model proposed by Li and Chou [11].

For simulating the van der Waals interactions at the graphene/polymer interphase, a truss model was employed as illustrated in Fig.7.2. The activation of a truss element is determined by the distance between an atom in the graphene sheet and a node in the continuum state model (see Fig.7.2). That is, a truss element is activated when the distance between an atom/node in the graphene and a node in the continuum mesh for the polymer material is less than or equal to 0.65 nm. Mechanical properties for the truss elements were determined in a similar manner to that presented in the research work by Odegard et al. [12], namely, the Lennard-Jones (LJ) '6-12' potential given in Equation 7.5 was considered for simulating van der Waals interactions.

$$U(r) = 4\gamma\left[\left(\frac{\phi}{r}\right)^{12} - \left(\frac{\phi}{r}\right)^{6}\right] \tag{5}$$

wherer is the distance between two atoms, ϕ is the hard sphere radius (ϕ = 0.34m) and γ is the potential well depth (γ = 0.0556 kcal/mol). The mechanical properties for the truss elements were obtained by equating the LJ 6-12 potential with the structural strain energy of truss elements. The resulting expression is provided in Equation 7.6and was used for assigning material stiffness values to each truss element with a cross-sectional area of 0.0907 nm^2.

$$E(r) = \frac{8\gamma R_{Eq}}{A(r - R_{Eq})^2}\left[\left(\frac{\phi}{r}\right)^{12} - \left(\frac{\phi}{r}\right)^{6}\right] \tag{7.6}$$

The thickness of graphene sheets and continuum polymer phase was kept at 0.344 nm and 0.3816 nm respectively for all model configurations investigated in this study. The proposed RVE simulated the crack growth under plane stress conditions, as the thickness of the RVE under consideration is comparably smaller than the other dimensions.

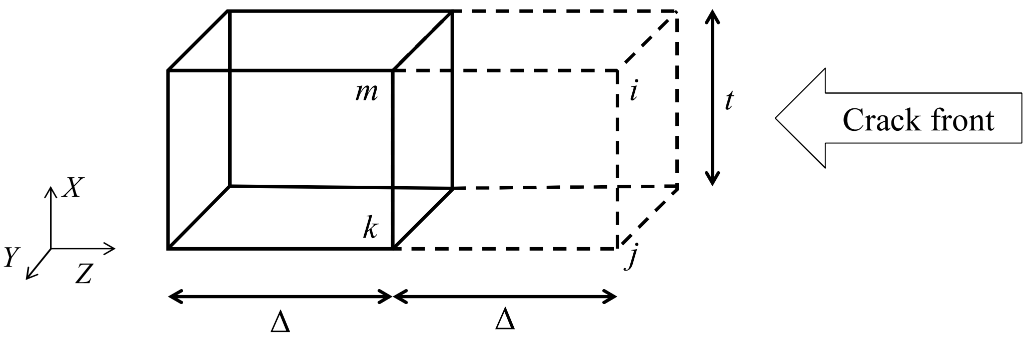

Fig.7.3 *Schematic of crack front in eight node 3D solid 45 element with proper coordinates.*

$$G_{\mathrm{I}} = \frac{1}{2t\Delta}\{F_{iy}(v_m - v_{m'}) + F_{jy}(v_k - v_{k'})\} \tag{7.7}$$

In this work, the virtual crack closure technique (VCCT) was employed in conjunction with a multiscale model to study the fracture characteristics of graphene/polymer nanocomposites under the opening mode of crack propagation. The strain energy release rate (SERR) (G_{I}) was considered as the characterizing parameter in this work. The mathematical formulation based on Fig.7.3 is provided in Equation 7.7 for estimating (G_{I}) under the opening mode of fracture [13].

7.3 Results and discussion

The multiscale model discussed in the preceding section was employed in this research work to characterize fracture behaviour and toughening mechanism in graphene nanocomposites. In this chapter, two different cases were considered for the modelling, first when the crack does not interact with the graphene (Fig.7.4) and the other case when crack interacts with the graphene (Fig.7.10). Calculations for graphene volume fraction involved in the RVE were performed according to Equation 7.8.

$$\text{Volume fraction (VF)} = \frac{\text{length}_{\text{Gr}} \times \text{width}_{\text{Gr}} \times \text{thickness}_{\text{Gr}}}{\text{Length}_{\text{RVE}} \times \text{Width}_{\text{RVE}} \times \text{Thickness}_{\text{Gr}}} \tag{7.8}$$

where VF, G_r and RVE represents graphene volume fraction, graphene and representative volume element respectively.

7.3.1 Modelling without interaction of crack with graphene interphase

The graphene considered in the multiscale models had 19 cells fixed along the length of the RVE, whereas a different number of cells were employed along the width of RVE, according to the volume fraction of graphene.

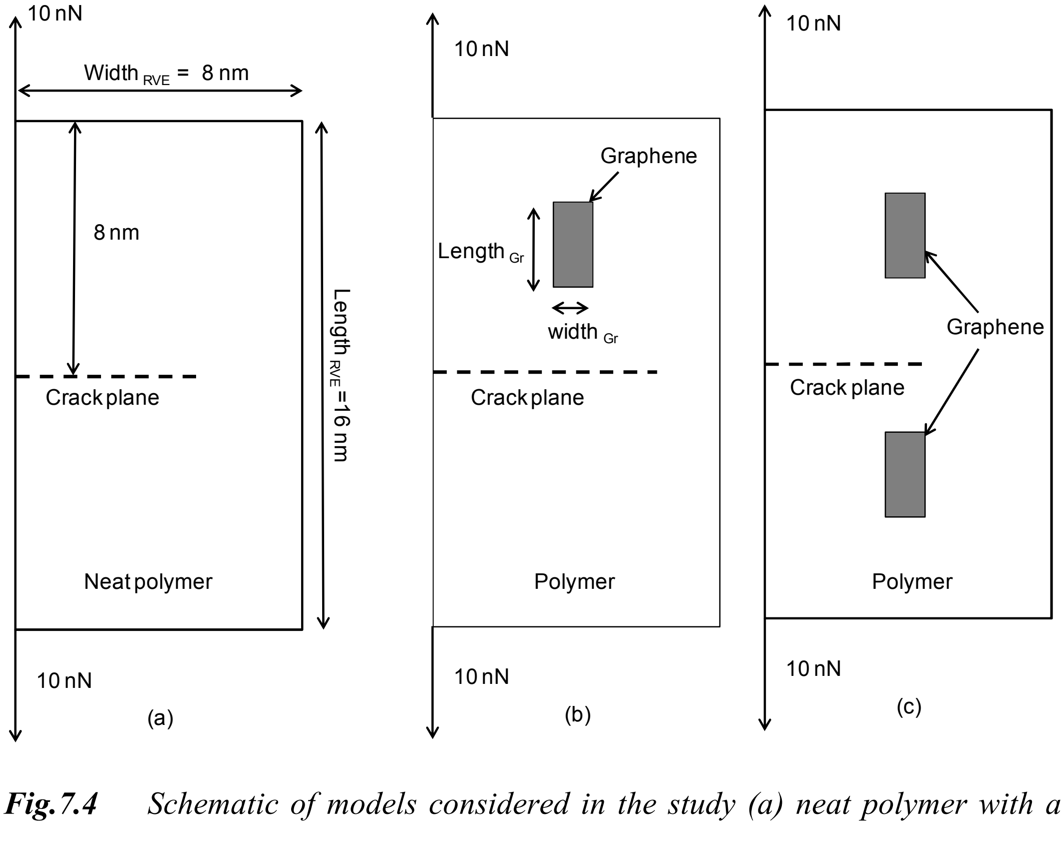

Fig.7.4 *Schematic of models considered in the study (a) neat polymer with a crack (b) Single graphene/polymer nanocomposite (c) twin graphene /polymer nanocomposite.*

SERR (G_I) values obtained for the crack shown in Fig.7.4 (a, b and c) were tested for convergence. Convergence results plotted in Fig.7.5 correspond tothe model developed for pure epoxy (Fig.7.4a), single graphene (graphene size 4.1209 nm x 1.47 nm) (Fig.7.4b) and two graphene sheets of length and width 4.1209 nm and 1.47 nm (Fig.7.4c) respectively. It can be concluded from the plotted results in Fig.7.5 that SERR (G_I) values converged to a finite value even with a coarse mesh size. In this study, an element size length of 0.3 nm was considered for modelling the crack tip coordinates.

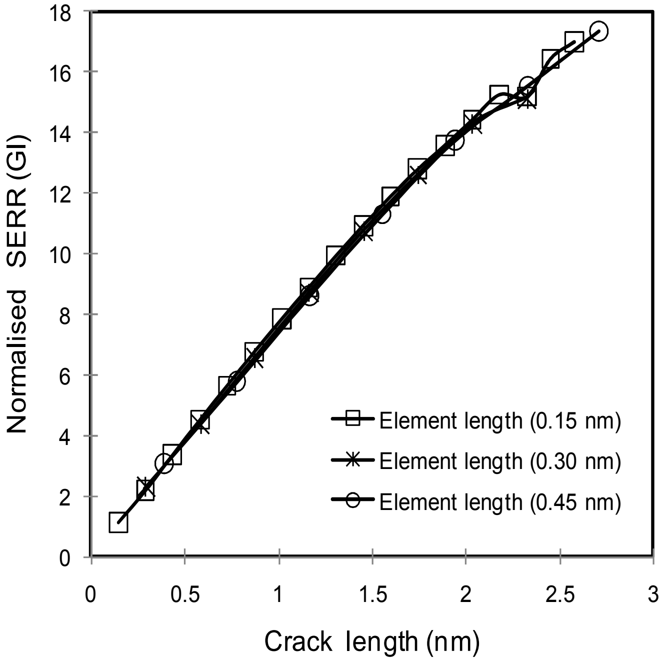

Fig.7.5a *Convergence results for model developed for the neat epoxy.*

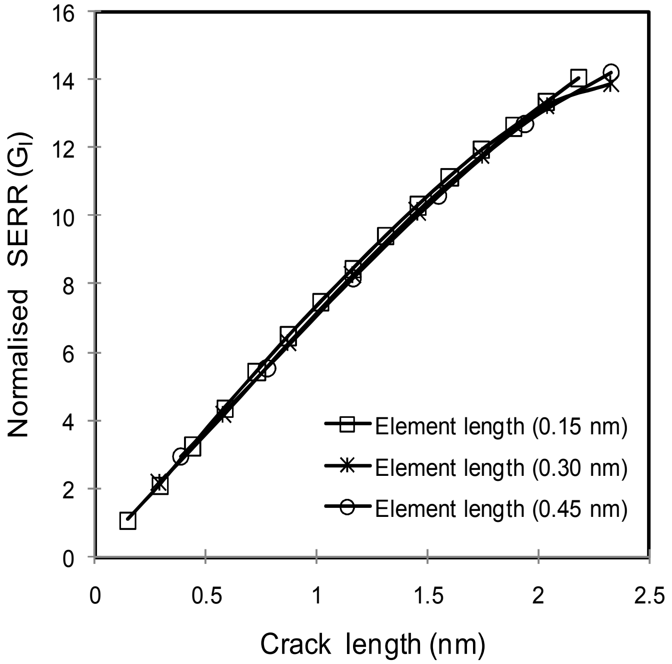

Fig.7.5b *Convergence results with single graphene sheet.*

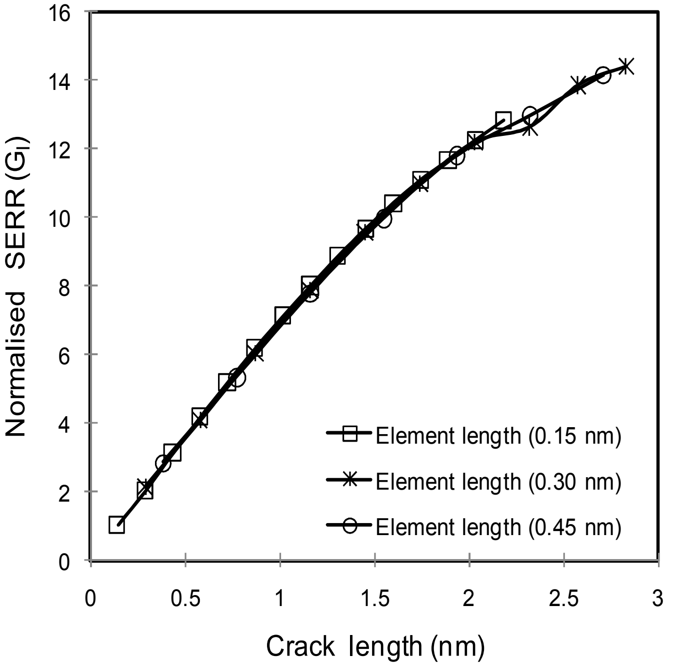

Fig.7.5c *Convergence results for the model with twin graphene sheet.*

Initially, SERR values were estimated for a crack propagating in neat polymer with boundary conditions as shown in Fig.7.4 a. Resulting SERR values were considered as reference values G_{IR} for subsequent investigations.

In the first part of this study the effect of graphene volume fraction on mode I (G_{I}) cohesive crack growth was investigated, considering boundary conditions as illustrated in Fig.7.4b. Results obtained from the simulations are shown in Fig.7.6.It can be inferred from the data plotted in this figure that crack growth in terms of SERR G_{I} was reduced with the increase in graphene volume fraction. In comparison to the neat epoxy model (i.e. aforementioned reference values (G_{IR})an improvement of up to 6% in fracture toughness (when the crack passes in the vicinity of the graphene sheet) was observed for a graphene volume fraction of 2.125%, which increased to 18% for a volume fraction of 8.5%.Note that in the current modelling approach an increase in graphene volume fraction is associated with a reduction of the graphene sheet aspect ratio, which is defined as the length to width ratio. The influence of graphene aspect ratio will further be discussed in the following sections.

Observed improvements in fracture toughness of graphene nanocomposites were attributed to the change in stress distribution in the (continuum) polymer epoxy phase due to the graphene inclusion in the vicinity of the crack. It is postulated that graphene with its space frame structure and high stiffness bears most of the applied load and shields the crack tip from opening loads or crack driven forces, whereas higher SERR ($G_{1\mathrm{R}}$) values in neat epoxy can be attributed to the absence of this shielding effect.

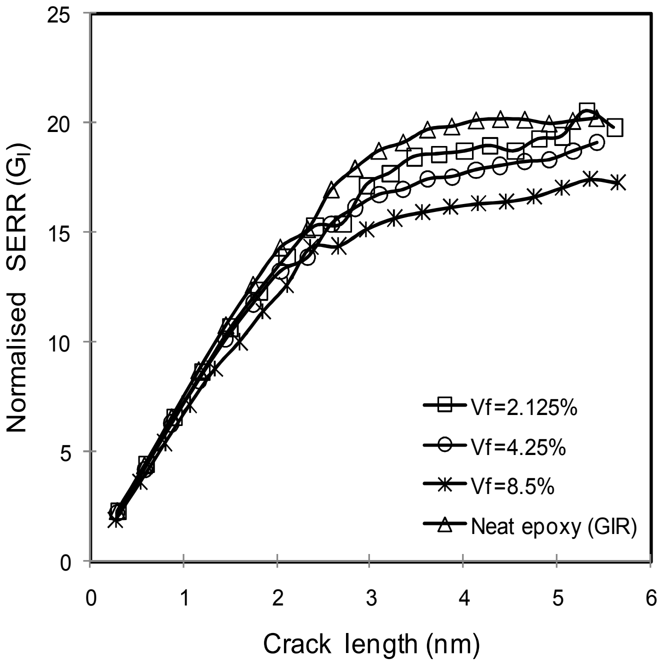

Fig.7.6 *Effect of graphene volume fraction on SERR (G_I)*

Shielding effects in graphene/polymer nanocomposites:

To further investigate the influence of graphene on fracture characteristics and the aforementioned shielding effect of graphene in graphene/polymer nanocomposites, modelling was performed with all three models as described in Fig.7.4. Again, the SERR G_{IR} values obtained according to Fig.7.4a were compared with G_I values employing the conditions defined in Figs. 7.4b and 7.4c. Corresponding results are plotted in Fig.7.7. Legend entries of 'Neat epoxy', 'Single graphene' and 'Twin graphene' in this figure correspond to SERR values obtained from models defined in Figs.7.4a, 7.4b and 7.4c respectively. The graphene sheets considered in the RVE for the 'Single graphene' and 'Twin graphene' cases had a fixed aspect ratio of 2.8, i.e. length and width were 4.1209 nm and 1.47 nm respectively. The graphene volume fractions were correspondingly 4.25% and 8.5%.

It can be inferred from the SERR values plotted in Fig.7.7 that a significant improvement in fracture characteristics was obtained for the nanocomposite reinforced with a graphene sheet on both sides of the crack plane. For this configuration, G_I values were reduced up to 24% (for crack propagation near the graphene sheet) compared with the G_{IR} reference values. Modelling results therefore indicate that the crack tip shielding effect from crack driving forces is more pronounced when graphene is present next to the crack on both sides of the crack plane. It shall be mentioned at this point that an improvement in SERR also occurs when a 'Single graphene' model with a graphene volume fraction identical to the 'Twin graphene' case is considered, which is shown in the subsequent section.

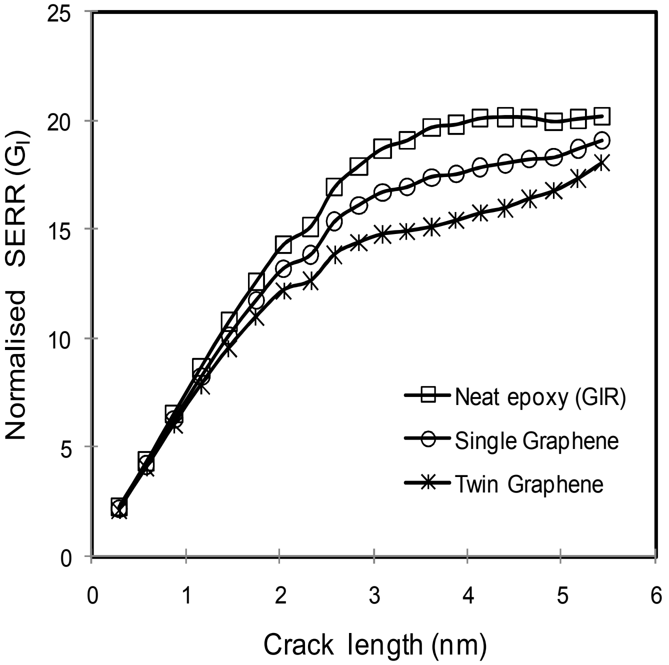

Fig.7.7 *Effect of graphene reinforcement on SERR (GI) values for polymer material.*

Graphene dispersion and dimensional effects:

Earlier experimental works [2,3] showed that graphene/polymer nanocomposites have enhanced fracture toughness compared to neat polymer. Due to challenges associated with the mixing of graphene in polymer, none of the studies have thus far been devoted to evaluating the effect of graphene dispersion and its aspect ratio on nanocomposite fracture toughness. Experimental results mostly dealt with graphene volume fraction and its impact on fracture toughness. This section of numerical analysis was conducted to study the effect of graphene aspect ratio and its distribution in the polymer matrix on fracture toughness of the developed nanocomposite.

The multiscale models as defined in the schematics in Figs. 7.4b and 7.4c were again used in this final part of the analysis. Results obtained from the model defined by Fig.7.4b, i.e. graphene with a low aspect ratio, are referred to as 'Single graphene' in Figs. 7.8 and 7.9. A graphene nanocomposite with high aspect ratio and uniform dispersion was simulated using the model from Fig.7.4c. The length of the graphene sheets ($length_{\mathrm{Gr}}$) employed in the above models was kept constant at 4.1209 nm. The sheet width, however, was adjusted, that is, for the high aspect ratio and uniform dispersion model (Fig.7.4c) half the width ($width_{\mathrm{Gr}}$) of the graphene sheet was employed compared to the low aspect ratio model (Fig.7.4b). The analysis in this section was performed for two different cases, i.e. graphene volume fractions of 4.25% and 8.5%.

First, modelling was performed for a graphene volume fraction of 8.5%. Corresponding SERR values are plotted with respect to crack length in Figure 7.8, where legend entries of 'Single graphene' and 'Twin graphene' represents graphene with an aspect ratio (A.R.) of 1.4 and 2.8 respectively. In Fig.7.8 the maximum improvement in fracture toughness (crack passing the graphene sheet) compared to the neat polymer was approximately 18% for the 'Single graphene' case, whereas the improvement was about 24% for the 'Twin graphene' model, which is a difference of 6 percentage points. These results indicate that nanocomposite fracture toughness improves with increasing graphene aspect ratio as well as for nanofillers being uniformly distributed in the matrix.

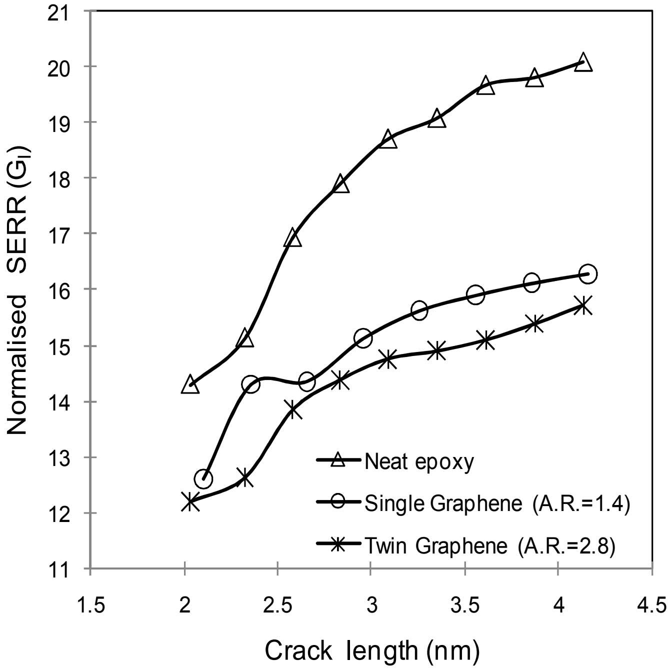

Fig.7.8 *Effect of graphene aspect ratio and dispersion on SERR (GI) for a constant graphene volume fraction of 8.5%.*

To corroborate the above findings, modelling was next performed for a graphene volume fraction of 4.25%, and results are shown in Fig.7.9. Here, legend entries of ‘Single graphene’ and ‘Twin graphene’ correspond to graphene aspect ratios of 2.8 and 5.6 respectively. Fig.7.9again shows a superior performance for the ‘Twin graphene’ configuration, yet improvements in SERR were lower in absolute terms than in the previous case with higher graphene volume fraction. Notably, for this lower graphene volume fraction as well as the higher graphene aspect ratios, the fracture toughness improvement for the ‘Twin graphene’ configuration compared to the ‘Single graphene’ model was greater, which is now 10 percentage points (compared to 6 percentage point in the previous analysis with a graphene volume fraction of 8.5%). Based on these results it is postulated that the greatest enhancement of fracture toughness can be expected from a nano-graphene filler that is uniformly distributed in the polymer matrix and has high aspect ratio graphene sheets.

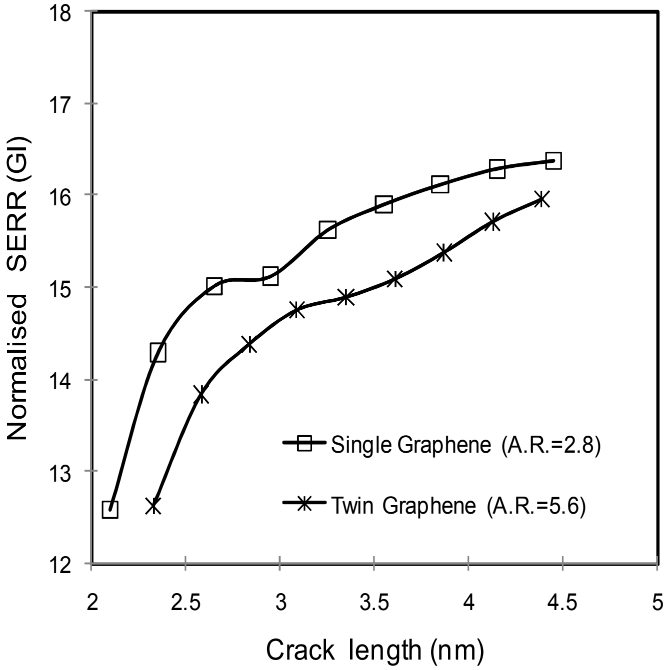

Fig.7.9 *Effect of graphene aspect ratio and dispersion on SERR (GI) for a constant graphene volume fraction of 4.25%.*

7.3.2 Simulation to study fracture toughening with crack interacting with graphene interphase[10]

Similar to the preceding work, the multiscale model was enhanced in this part of the research to identify the underlying fracture toughening mechanism in graphene nanocomposites. In this subsection of modelling, results are discussed

---

[10] A version of this section has been submitted for publication. A.Parashar and P.Mertiny 2012.Adv. Eng. Mat. (Under review)

with respect to a crack that interacts with a graphene interphase as indicated with the help of ‘Crack D’ in Fig.7.10. The applied loading and boundary conditions employed in the current study are defined and illustrated in Fig.7.10a and 7.10b. The model schematics illustrated in Figs.7.10a and 7.10b correspond to neat epoxy and polymer reinforced with graphene respectively.

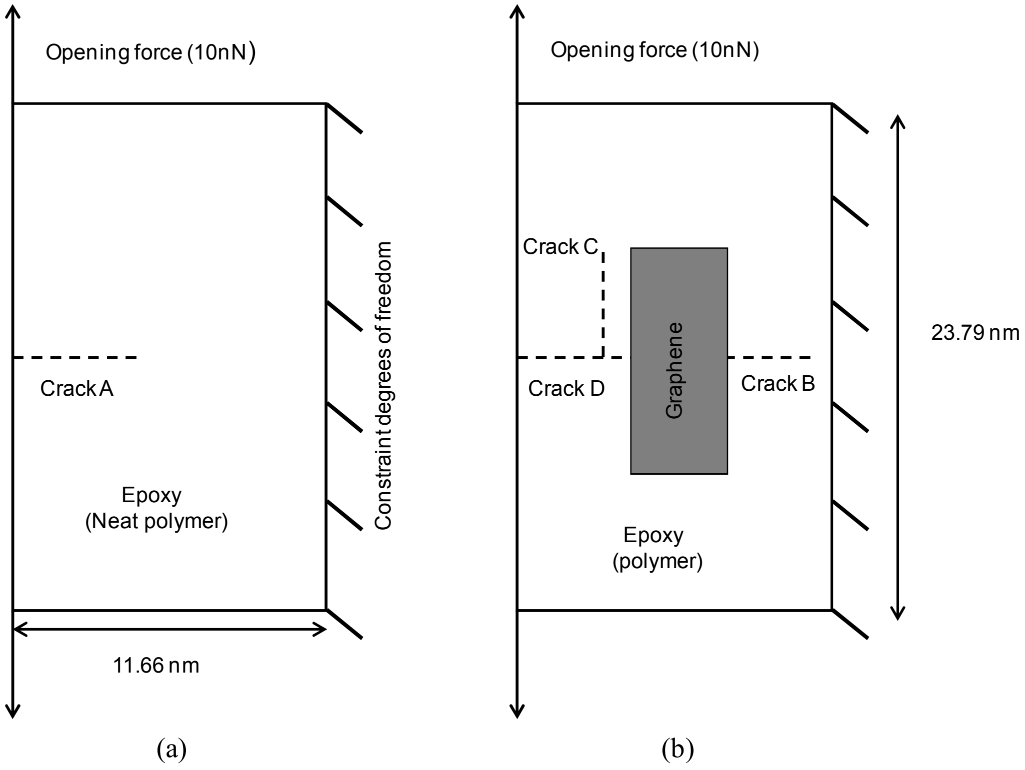

Fig.7.10 *(a) Schematic of model for 'Crack A' in neat epoxy (b) schematic of model for 'Crack D', 'Crack B' and 'Crack C' in graphene/polymer nanocomposite.*

Initially, modelling was performed to study the effect of graphene on fracture toughening of nanocomposites. Schematics of both models defined in Fig.7.10 were employed to simulate ‘Crack A’ and ‘Crack D’. SERR (G_I) values obtained for 'Crack A' residing in the neat epoxy were compared with the SERR (G_I) values obtained for a 'Crack D' (defined in Fig.7.10b) for a nanocomposite with graphene volume fraction of 3%. Corresponding results are illustrated in Fig.7.11.

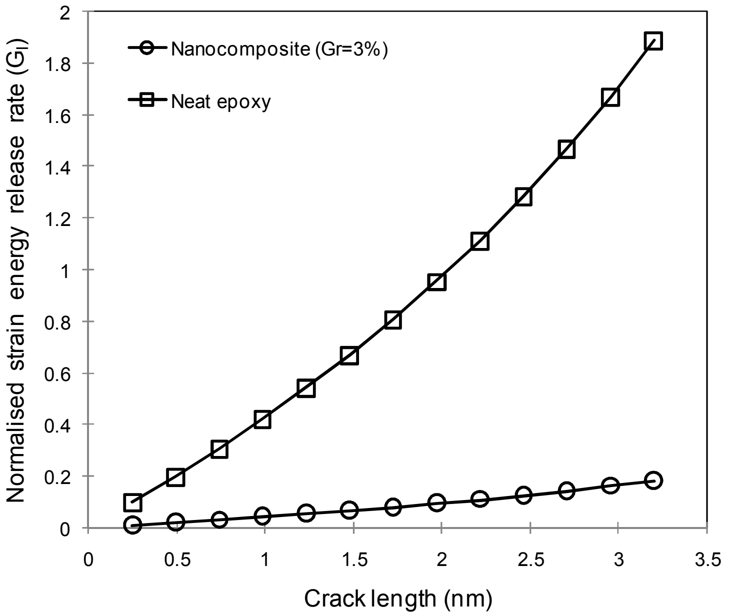

Fig.7.11 *Comparison of SERR (GI) values for 'Crack A' in neat epoxy and 'Crack D' in graphene nanocomposite.*

A significant improvement in fracture toughness of the nanocomposite with graphene volume fraction of 3%was observed. The two-dimensional geometry of graphene, along with its high stiffness values helps in improving the fracture toughness of graphene nanocomposites. The strong interphase between graphene and polymer also helps in transferring the applied load to the graphene and improved the load bearing capability of graphene nanocomposites.

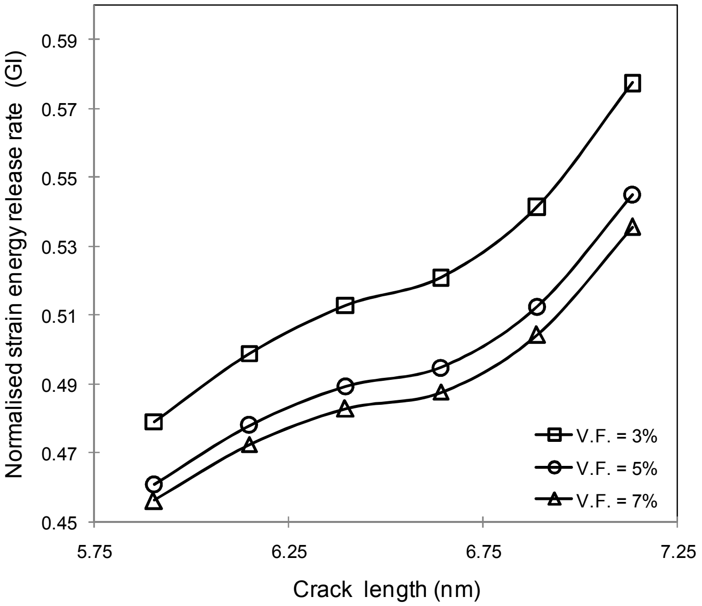

Fig.7.12 *SERR (GI) values for 'Crack D' in graphene nanocomposite with different volume fraction of graphene.*

Next part of the simulation was performed with the help of the model defined in Fig.7.10b. A simulation was performed to study the effect of graphene volume fraction on the growth of ‘Crack D’ under mode I fracture. Results obtained in terms of SERR (G_I) values with respect to different graphene volume fractions are plotted in Fig.7.12. It can be seen that fracture toughness of nanocomposite improves with increasing graphene volume fraction. A significant improvement in fracture toughness was observed when graphene volume fraction was raised from 3% to 5%, whereas a comparatively small increment in percentage points was observed for a rise from 5% to 7% in graphene volume fraction. An overall increase of 10 percent points in the fracture toughness was observed with a raise in graphene volume fraction from 3% to 7%.

In the final and concluding part of the simulation, an investigation was performed to study the interaction of a ‘Crack D’ with the graphene nanofiller. Two possible crack paths ('Crack B' and 'Crack C') were assumed for 'Crack D' after interacting with the graphene as explained in Fig.7.10b. SERR (G_I) values were estimated for 'Crack B' and 'Crack C' with respect to crack length.

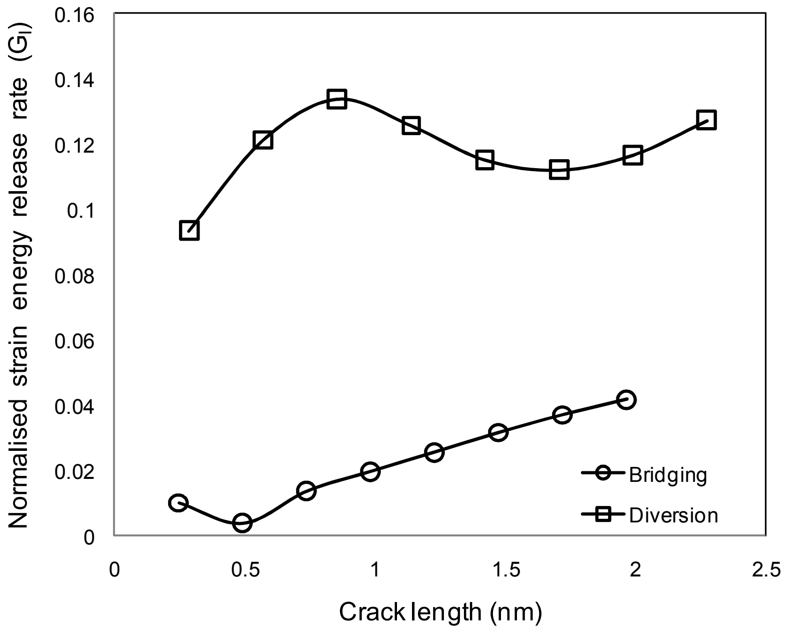

Fig.7.13 *SERR (GI) values for possible crack paths after interacting with the graphene interphase.*

From the data plotted in Fig.7.13, it can be concluded that the probable fracture toughness mechanism in graphene nanocomposites is crack diversion rather than a bridging mechanism. It can be seen in Fig.7.13 that SERR (G_I) values for 'Crack C' (representing diversion mechanism) is 10 times higher compared to the situation for 'Crack B'(representing bridging mechanism). The two-dimensional planar structure of graphene is considered responsible for the strong interphase between graphene and polymer, which emphasizes crack diversion as the main toughening mechanism rather than crack bridging.

The proposed multiscale model was successfully employed also in this part of the research project in which the fracture toughening mechanism in graphene nanocomposites was studied. Crack diversion from the graphene/polymer interphase is considered the main toughening mechanism in graphene based nanocomposites.

7.4 Conclusions

A finite element based multiscale modelling technique has been employed in this chapter to study the fracture toughening mechanisms in graphene nanocomposites. Significant improvements in the fracture toughness of graphene/polymer nanocomposites were predicted by the current modelling results. It can be concluded from these results that a uniform distribution of high aspect ratio graphene is required to harness the full potential of graphene as a nanofiller. Uniform graphene distribution and high aspect ratio of graphene were found to be more important parameters then graphene volume fraction for improving fracture toughness of developed nanocomposites.

Crack diversion from the graphene/polymer interphase is seen as the main toughening mechanism in graphene based nanocomposites. The planar structure of graphene was assumed to be the reason behind deflecting the crack more efficiently compared to a crack bridging mechanism.

7.5 Bibliography

1. M.A.Rafiee, J.Rafiee, I.Srivastave, Z.Wang, H.Song, Z.Z.Yu, N. Koratkar, *Fracture and fatigue in graphene nanocomposites*, Small 6(**2010**)179-83.
2. M.A.Rafiee, J.Rafiee, Z.Wang, H. Song, Z.Z. Yu , N. Koratkar, *Enhanced mechanical properties of nanocomposites at low graphene content*. ACS Nano 3(**2003**) 3884-3890.
3. A.P.Awasthi, D.C.Lagoudas, D.C.Hammerand, *Modelling of graphene polymer interfacial mechanical behaviour using molecular dynamics*. Modell. Simul. Mater. Sci. Eng.17(**2009**) 31-37.

4. J.Cho, J.J.Luo, I.M.Daniel, *Mechanical characterization of graphite/epoxy nanocomposites by multi-scale analysis*, Compos. Sci. Technol. 67(**2007**) 2399-2407.
5. A.Montazeri, H.R.Tabar, *Multiscale modelling of graphene and nanotube based reinforced polymer nanocomposites*, Phys. Lett. A375 (**2011**) 4034-4040.
6. K.I.Tserpes, P.Papanikos, S.A.Tsirkas, *A progressive fracture model for carbon nanotubes*. Composites Part B 37 (**2006**) 662-669.
7. K.I.Tserpes, P. Papanikos, G. Labeas, Sp.G. Pantelakis, *Multiscale modelling of tensile behaviour of carbon nanotube reinforced composites*. Theor. Appl. Fract. Mech. 49(**2008**) 51-60.
8. T.Belytschko, S.Xiao, G.Schatz, R.Ruoff, *Atomistic simulations of nanotube fracture*, Phys.Rev. B:Condens. Matter 65 (**2002**) 235430.
9. S.A.Meguid, J.M.Wernik, Z.Q.Cheng, *Atomistic based continuum representation of the effective properties of nano-reinforced epoxies*, Int J Solids Struct. 47(**2010**) 1723-1736.
10. N.Hu, H. Fukunaga, C.Lu, M.Kameyama, B. Yan, *Prediction of elastic properties of carbon nanotube reinforced composites*, Proc. R. Soc. Lond. A 461(**2005**) 1685-1710.
11. C.Li, T.W.Chou, *Multiscale modelling of compressive behaviour of carbon nanotube/polymer composites*, Compos. Sci. Technol. 66(**2006**) 2409-2414.
12. G.M.Odegard, T.S.Gates, K.E.Wise, C.Park, E.J.Siochi, *Constitutive modelling of nanotube reinforced polymer nanocomposites*. Compos.Sci.Technol. 63(**2003**) 1671-1687.
13. G.De. Roeck, M.M.A. Wahab, *Strain energy release rate formulae for 3D finite element*. Eng. Fract. Mech. 50(**1995**) 569-80.

Chapter 8

Conclusions and Recommendations

8.1 Concluding remarks

Adhesive bonding for fibre-reinforced polymer pipe sections is emerging as a promising alternative to mechanical means of joining. Several advantages such as a large number of design variables, intact fibre architecture, uniform stress distribution and ease of handling are associated with adhesive bonding of polymer composite pipe sections. Over several decades researchers have contributed to the optimization of manufacturing techniques and design parameters related to adhesively bonded composite piping. The present research project successfully proposed a numerical solution to identify the most damage prone components in bonded pipe sections and also suggests a numerical framework to improve joint characteristics.

The first phase of the research project, which dealt with the macroscopic analysis of adhesively bonded FRP pipe sections, provided the insight that the region of likely joint failure shifts as a function of the inside pipe diameter, when pipe and coupler with multi-angle fibre architecture [±30, $\pm60_m$] was considered. The region susceptible to failure resides in the composite pipe sections for small diameter pipe joints, whereas it shifts toward the adhesive material in joints for large diameter piping. Adhesives are thus seen to be the weak link the development of large diameter piping.

In the second and third phase of the project a numerical modelling approach was developed for improving joint characteristics. The second phase identified graphene as a suitable nanofiller for reinforcing adhesives. To evaluate the effect of graphene nanofiller on the macroscopic properties of an adhesive material, an atomistic modelling technique was proposed. This finite element based atomistic model is less numerical demanding compared to other numerical techniques such as molecular dynamics and Monte Carlo simulations as it deals with fewer degrees of freedom.

The third and final phase of the research revealed promising improvements in the properties of polymer materials (adhesives) with the inclusion of graphene nanofiller. It was shown that graphene reinforced polymer materials exhibit higher fracture toughness and stability than the neat polymer. A uniform distribution of graphene as well as a high aspect ratio of graphene was found to be more important parameters than graphene volume fraction for achieving superior nanocomposite mechanical properties.

The developed multiscale approach constitutes as a viable solution to the limitations that are associated with experimental testing of graphene nanocomposites. The numerical methods therefore enhance the understanding of adhesively bonded composite pipe joints and improvements that can be achieved in adhesives through nanofiller addition. The presented research work thus contributes to extended the range of applications of nanocomposites as adhesives.

8.2 List of publications

- **Avinash Parashar**, Pierre Mertiny. (**2012**)*Failure mechanism in adhesively bonded FRP pipe sections with different fibre architecture*, Composite Part B,10.1016/j.compositesb.2012.10.041.
- **Avinash Parashar**, Pierre Mertiny. (**2012**)*Multiscale model to study fracture toughening in graphene/polymer nanocomposites*, International Journal of Fracture, 10.1007/s10704-012-9779-y.
- **Avinash Parashar**, Pierre Mertiny. (**2012**) *Multiscale model to investigate the effect of graphene on the fracture characteristics of graphene/polymer nanocomposite*, Nanoscale research letters. 7, 595.
- **Avinash Parashar**, Pierre Mertiny. (**2012**) *Representative volume element to estimate buckling behavior of graphene/polymer nanocomposite*. Nanoscale research letters.7, 515.
- **Avinash Parashar**, Pierre Mertiny. (**2012**)*Effect of FRP pipe scaling on its adhesive bonding strength*. Journal of Adhesion. 88,866-880.

- **Avinash Parashar**, Pierre Mertiny. (**2012**)*Study of mode I fracture of graphene sheets using atomistic based finite element modeling and virtual crack closure technique*. International Journal of Fracture. 176,119-126.

- **Avinash Parashar**, Pierre Mertiny.(**2012**)*Adhesively bondedcomposite tubular joints: Review*. International Journal of Adhesion and Adhesives. 38, 58-68.

- **Avinash Parashar**, Pierre Mertiny. (**2012**) *Finite element analysis to study the effect of dimensional and geometrical parameters on the stability of graphene sheets*. Journal of Computational and Theoretical Nanoscience (**Accepted**).

- **Avinash Parashar**, Pierre Mertiny. (**2012**)*Effect of van der Waals forces on the buckling strength of multiple graphene sheets*. Computational and theoretical nanoscience (**Accepted**).

- **Avinash Parashar**, Pierre Mertiny. Effect of van der Waals interaction on the fracture characteristics of graphene sheet, Solid state communications (**Submitted**).

- **Avinash Parashar**, Pierre Mertiny. (**2011**) *Impact of scaling on fracture strength of adhesively bonded fibre reinforced polymer piping*. Procedia Engineering. 10, 455-459.

- **Avinash Parashar**, Pierre Mertiny. (**2010**) *Challenges in joining thermoset composite piping*. International pipeline conference, Calgary - IPC2010-31297.

- Pierre Mertiny, Mohamed T. Bashar, **Avinash Parashar**, Kulwinder Juss. (**2010**) *Technological advances for improved performance and operation of fiber reinforced polymer piping*. *ASME Pressure Vessels & Piping Conference*.

8.3 Future research work

The scope of nanocomposite is vast, however, only a small portion is considered in this research project. Based on experiences gained during this research the following topics are recommended for future work:

- The multiscale modelling approach can further be expanded to include the interaction between multiple graphene sheets and its impact on the mechanical properties of nanocomposites.
- Upon characterizing actual graphene/polymer samples using e.g. tomography, the coordinates and orientation of graphene platelets can be determined and then employed to develop multiscale models with realistic graphene distribution. It is conceivable that mechanical properties for actual nanocomposites can thus be predicted and compared to experimental data.

Appendix 1

ANSYS Codes

(1) Codes for atomistic fracture model

```
/Title, Zig Zag Graphene Sheet Model for Fracture in Mode I with VCCT
/zoom,1,off
*AFUN,DEG
/REPLOT
l          =   0.1421          ! Bond Length in nano alerady estabilished with
N1         =   20             ! Along Vertical direction
N2         =   34             ! Along horizontal direction
c****************************************************
c***** Total Nodes and Elements with Full Geometry
C****************************************************
! Node              =          5000
! Element           =          5000
c****************************************************
/PREP7
c***********************************************
c**** Defining Element and Material Properties
c***********************************************
et,1,beam3
mp,ex,1,5.49e-6
mp,gxy,1,0.8716e-6
!r,1,0.01687,0.2267e-4,0.2267e-4,0.1466,0.1466,,,,,,,
r,1,0.01687,0.2267e-4,0.1466
n,1,l*1.732*0.5,0,0
n,2,0,0.5*l,0
n,3,0,1.5*l,0
n,4,l*1.732*0.5,2*l,0
n,5,l*1.732*0.5,3*l,0
e,1,2
e,2,3
e,3,4
```

```
e,4,5
*get,nmax1,node,,num,max
egen,N2,nmax1,all,,,,,,,,l*1.732,0,0
*get,nmax2,node,,num,max
*get,emax1,elem,,num,max
emax1=emax1+1
e,4,8
egen,N2,nmax2,emax1,emax1,,,,,,,l*1.732,0,0
nsel,all
nummrg,all
numcmp,node
numcmp,elem
*get,nmax3,node,,num,max
*get,emax2,elem,,num,max
e,1,7
egen,N2,nmax3,emax2+1,emax2+1,,,,,,,l*1.732,0,0
nsel,all
nummrg,all
numcmp,node
numcmp,elem
c*************************
c*****Check Node Selections
c*************************
*get,nn1,node,,num,max
n,nn1+1,l*1.732*N2,0.5*l
n,nn1+2,l*1.732*N2,1.5*l
nummrg,node,,,,high
e,nn1+1,nn1+2
nsel,all
numcmp,node
numcmp,elem
eplot
*get,nmax4,node,,num,max
c*********************************
c**** Along Vertical Direction
```

```
c**************************************
egen,N1,nmax4,all,,,,,,,,0,3*l,0
nsel,all
nummrg,all
numcmp,node
numcmp,elem
c**************************************
c**** Delete Last Row of Elements
c**************************************
nsel,s,loc,y,3*l*N1 !+0.15
esln,s,0
edele,all
ndele,all
nsel,all
esel,all
/replot
eplot
/replot
nsel,all
nummrg,all
c*********************************************
c*****Calculation of Dimenional Parameter
c*********************************************
width  = l*1.732*N2           ! Width of the graphene sheet
length = 3*l*(N1-1)+2*l     ! Length of the graphene sheet
AR     = length/width         ! Aspect Ratio of the graphene sheet
!*status,AR
c***************************************************
c**** SELECTING ELEMENTS FOR CRACK PROPAGATION
c***************************************************
esel,s,elem,,1849,1981,4
edele,all
esel,all
cs,11,0,1279,1283,1418
csys,11
```

```
x=0
*do,ii,1,34,1
n,7000+ii,x,0,0
x=x+l*1.732
*enddo
nsel,s,loc,y,0
NUMMRG,NODES,,,,high
c************************************
c***** Nodes to create crack elements
c************************************
x=0
*do,ii,1,34,1
n,8000+ii,x,0,0
x=x+l*1.732
*enddo
c*****************************************
nsel,all
cs,12,0,1280,1284,1418
csys,12
x=0
*do,ii,1,34,1
n,9000+ii,x,0,0
x=x+l*1.732
*enddo
nsel,s,loc,y,0
NUMMRG,NODES,,,,high
c************************************
c***** Nodes to create crack elements
c************************************
x=0
*do,ii,1,34,1
n,10000+ii,x,0,0
x=x+l*1.732
*enddo
c******************************
```

```
c***** Crack Elements Creation
c******************************
numstr,elem,7001
*do,ii,1,34,1
nsel,s,node,,8000+ii
nsel,a,node,,10000+ii
e,8000+ii,10000+ii
*enddo

c*************************************************************
c***** Coupling of nodes at two ends of the crack beam element
c************************************************************
*do,ii,1,34,1
nsel,s,node,,7000+ii
nsel,a,node,,8000+ii
cp,next,all,all
*enddo
*do,ii,1,34,1
nsel,s,node,,9000+ii
nsel,a,node,,10000+ii

cp,next,all,all
*enddo
nsel,all
c***************************************
c***** Node Generation at the other end
c***************************************
esel,s,elem,,2052,2184,4
esel,a,elem,,2255
edele,all
esel,all
cs,13,0,1415,1419,1418
csys,13
x=0
*do,ii,1,35,1
```

```
n,11000+ii,x,0,0
x=x+l*1.732
*enddo
nsel,s,loc,y,0
NUMMRG,NODES,,,,high
nsel,all
eplot
c******************************************
c***** Nodes to create couple elements with
c******************************************
x=0
*do,ii,1,35,1
n,12000+ii,x,0,0
x=x+l*1.732
*enddo
c************************
c****** Nodes at top Part
c************************
cs,14,0,1416,1420,1418
csys,14
x=0
*do,ii,1,35,1
n,15000+ii,x,0,0
x=x+l*1.732
*enddo
nsel,s,loc,y,0
NUMMRG,NODES,,,,high
nsel,all
eplot
c****************************
c**** Creating beam elements
c****************************
numstr,elem,9001
*do,ii,1,35,1
nsel,s,node,,12000+ii
```

```
nsel,a,node,,15000+ii
e,12000+ii,15000+ii
*enddo
c**************************************************************
c***** Coupling of nodes at one end of the crack beam element
c**************************************************************
*do,ii,1,35,1
nsel,s,node,,11000+ii
nsel,a,node,,12000+ii
cp,next,all,all
*enddo
nsel,all
esel,all
csys,0
finish
C********************************
c***** Apply Boundary Conditions
c********************************
/solu
nsel,s,loc,x,width
d,all,all,0
nsel,all
f,2659,fy,1e-2
f,1,fy,-1e-2
nsel,all
solve
c********************
c*****Postprocessing
c********************
jj=1
*do,ii,1,25,1
/post1
nsel,s,node,,10000+ii
nsel,a,node,,11000+ii
nsel,a,node,,11000+ii+1
```

```
/FORMAT,,,16,8,400
/OUTPUT,force,solF,,APPEND
PRNLD,F
/output
nsel,all
/prep7
edele,7000+ii
finish
/solu
solve
finish
/post1
nsel,s,node,,10000+ii
nsel,a,node,,11000+ii
nsel,a,node,,11000+ii+1
/FORMAT,,,16,8,400
/OUTPUT,displacement,solU,,APPEND
PRNSOL,U,COMP
/OUTPUT
*enddo
```

(2) Sample codes for generating Multiscale model

```
/Title," Multiscale modeling to study bridging with graphene sheets"
/zoom,1,off
*AFUN,DEG
/REPLOT
xx      =   0
l           =   0.1421             ! Bond Length in nano already established with
N1         =   10                  ! Along Vertical direction
N2         =   6                   ! Along horizontal direction
c***********************************************
c******* defining continuum model geometry
c***********************************************
nn2   =  34
l2     =  0.2842*nn2
int    =  0.172
t      =  0.172
width  =  l*1.732*N2
length =  3*l*(N1-1)+2*l
ww     =  12
w1     =  ww-width-2*int
w2     =  w1*0.5
c***************************************************
/PREP7
c**********************************************
c**** Defining Element and Material Properties
c**********************************************
et,1,beam4
mp,ex,1,5.49e-6
mp,gxy,1,0.8716e-6
!r,1,0.01687,0.2267e-4,0.2267e-4,0.1466,0.1466,,,,,,,
r,1,0.01687,0.2267e-4,0.1466
```

```
n,1,l*1.732*0.5,0,0
n,2,0,0.5*l,0
n,3,0,1.5*l,0
n,4,l*1.732*0.5,2*l,0
n,5,l*1.732*0.5,3*l,0
e,1,2
e,2,3
e,3,4
e,4,5
*get,nmax1,node,,num,max
egen,N2,nmax1,all,,,,,,,,l*1.732,0,0
*get,nmax2,node,,num,max
*get,emax1,elem,,num,max
emax1=emax1+1
e,4,8
egen,N2,nmax2,emax1,emax1,,,,,,,l*1.732,0,0
nsel,all
nummrg,all
numcmp,node
numcmp,elem
*get,nmax3,node,,num,max
*get,emax2,elem,,num,max
e,1,7
egen,N2,nmax3,emax2+1,emax2+1,,,,,,,l*1.732,0,0
nsel,all
nummrg,all
numcmp,node
numcmp,elem
c************************
c*****Check Node Selections
c************************
*get,nn1,node,,num,max
n,nn1+1,l*1.732*N2,0.5*l
n,nn1+2,l*1.732*N2,1.5*l
```

```
nummrg,node,,,,high
e,nn1+1,nn1+2
nsel,all
numcmp,node
numcmp,elem
eplot
*get,nmax4,node,,num,max
c********************************
c**** Along Vertical Direction
c********************************
egen,N1,nmax4,all,,,,,,,,0,3*l,0
nsel,all
nummrg,all
numcmp,node
numcmp,elem
c********************************
c**** Delete Last Row of Elements
c********************************
nsel,s,loc,y,3*l*N1 !+0.15
esln,s,0
edele,all
ndele,all
nsel,all
esel,all
/replot
eplot
/replot
nsel,all
nummrg,all
numcmp,node
numcmp,elem
c**************************************
c*****Calculation of Dimenional Parameter
c**************************************
width  = l*1.732*N2           ! Width of the graphene sheet
```

```
length = 3*l*(N1-1)+2*l       ! Length of the graphene sheet
AR     = length/width         ! Aspect Ratio of the graphene sheet
*get,nmax5,node,,num,max
*get,emax3,elem,,num,max
c******************
c******key points
c******************
k,1,-int-w2,length+int+l2,t
k,2,-int,length+int+l2,t
k,3,width+int,length+int+l2,t
k,4,width+int+w2,length+int+l2,t
k,5,width+int+w2,length+int,t
k,6,width+int,length+int,t
k,7,-int,length+int,t
k,8,-int-w2,length+int,t
k,101,-int-w2,-int,t
k,102,-int,-int,t
k,103,width+int,-int,t
k,104,width+int+w2,-int,t
k,105,width+int+w2,-int-l2,t
k,106,width+int,-int-l2,t
k,107,-int,-int-l2,t
k,108,-int-w2,-int-l2,t
c*********************************
c*********************************
k,11,-int-w2,length+int+l2,0
k,12,-int,length+int+l2,0
k,13,width+int,length+int+l2,0
k,14,width+int+w2,length+int+l2,0
k,15,width+int+w2,length+int,0
k,16,width+int,length+int,0
k,17,-int,length+int,0
k,18,-int-w2,length+int,0
k,111,-int-w2,-int,0
k,112,-int,-int,0
```

```
k,113,width+int,-int,0
k,114,width+int+w2,-int,0
k,115,width+int+w2,-int-l2,0
k,116,width+int,-int-l2,0
k,117,-int,-int-l2,0
k,118,-int-w2,-int-l2,0
c***********************************
c***********************************
k,21,-int-w2,length+int+l2,-t
k,22,-int,length+int+l2,-t
k,23,width+int,length+int+l2,-t
k,24,width+int+w2,length+int+l2,-t
k,25,width+int+w2,length+int,-t
k,26,width+int,length+int,-t
k,27,-int,length+int,-t
k,28,-int-w2,length+int,-t
k,121,-int-w2,-int,-t
k,122,-int,-int,-t
k,123,width+int,-int,-t
k,124,width+int+w2,-int,-t
k,125,width+int+w2,-int-l2,-t
k,126,width+int,-int-l2,-t
k,127,-int,-int-l2,-t
k,128,-int-w2,-int-l2,-t
c**********************************
c**********************************
c*******creating volumes
c**********************************
c**********************************
v,1,2,7,8,11,12,17,18
v,11,12,17,18,21,22,27,28
v,2,3,6,7,12,13,16,17
v,12,13,16,17,22,23,26,27
v,3,4,5,6,13,14,15,16
v,13,14,15,16,23,24,25,26
```

```
v,8,7,102,101,18,17,112,111
v,18,17,112,111,28,27,122,121
v,6,5,104,103,16,15,114,113
v,16,15,114,113,26,25,124,123
v,101,102,107,108,111,112,117,118
v,111,112,117,118,121,122,127,128
v,102,103,106,107,112,113,116,117
v,112,113,116,117,122,123,126,127
v,103,104,105,106,113,114,115,116
v,113,114,115,116,123,124,125,126
c****************************
c****** Meshing attributes
c****************************
lsel,s,line,,1
lsel,a,line,,6
lsel,a,line,,14
lsel,a,line,,21
lsel,a,line,,25
lsel,a,line,,30
lsel,a,line,,34
lsel,a,line,,38
lsel,a,line,,43
lsel,a,line,,3
lsel,a,line,,10
lsel,a,line,,18
lsel,a,line,,23
lsel,a,line,,28
lsel,a,line,,33
lsel,a,line,,36
lsel,a,line,,41
lsel,a,line,,46
lsel,a,line,,48
lsel,a,line,,52
lsel,a,line,,57
lsel,a,line,,86
```

```
lsel,a,line,,89
lsel,a,line,,93
lsel,a,line,,61
lsel,a,line,,65
lsel,a,line,,70
lsel,a,line,,74
lsel,a,line,,78
lsel,a,line,,83
lsel,a,line,,88
lsel,a,line,,92
lsel,a,line,,96
lsel,a,line,,98
lsel,a,line,,101
lsel,a,line,,104
lesize,all,0.246
lsel,s,line,,4
lsel,a,line,,12
lsel,a,line,,20
lsel,a,line,,2
lsel,a,line,,8
lsel,a,line,,16
lsel,a,line,,22
lsel,a,line,,26
lsel,a,line,,31
lsel,a,line,,35
lsel,a,line,,39
lsel,a,line,,44
lsel,a,line,,49
lsel,a,line,,54
lsel,a,line,,59
lsel,a,line,,47
lsel,a,line,,50
lsel,a,line,,55
lsel,a,line,,62
lsel,a,line,,67
```

```
lsel,a,line,,72
lsel,a,line,,60
lsel,a,line,,63
lsel,a,line,,68
lsel,a,line,,97
lsel,a,line,,99
lsel,a,line,,102
lsel,a,line,,87
lsel,a,line,,90
lsel,a,line,,94
lsel,a,line,,73
lsel,a,line,,76
lsel,a,line,,81
lsel,a,line,,75
lsel,a,line,,80
lsel,a,line,,85
lesize,all,0.2842
lsel,s,line,,7
lsel,a,line,,15
lsel,a,line,,5
lsel,a,line,,13
lsel,a,line,,24
lsel,a,line,,29
lsel,a,line,,37
lsel,a,line,,42
lsel,a,line,,11
lsel,a,line,,19
lsel,a,line,,9
lsel,a,line,,17
lsel,a,line,,27
lsel,a,line,,32
lsel,a,line,,40
lsel,a,line,,45
lsel,a,line,,53
lsel,a,line,,58
```

```
lsel,a,line,,51
lsel,a,line,,56
lsel,a,line,,66
lsel,a,line,,71
lsel,a,line,,64
lsel,a,line,,69
lsel,a,line,,100
lsel,a,line,,103
lsel,a,line,,91
lsel,a,line,,95
lsel,a,line,,77
lsel,a,line,,82
lsel,a,line,,79
lsel,a,line,,84
lesize,all,,,1
c******Isotropic Adhesive Material
et,2,solid 45
mp,Ex,2,4.8e-9
mp,Prxy,2,0.34
type,2
mat,2
numstr,node,50001
numstr,elem,50001
mshape,0,3D
mshkey,1
vmesh,all
lsel,all
nsel,all
esel,all
c****************************************
c******* Creating nodes for van der Waals
c****************************************
yy=0
*do,ii,1,17,1
n,20000+ii,-int,-int+yy,t
```

```
n,20000+17+ii,-int,-int+yy,0
n,20000+34+ii,-int,-int+yy,-t
n,20000+51+ii,width+int,-int+yy,t
n,20000+68+ii,width+int,-int+yy,0
n,20000+85+ii,width+int,-int+yy,-t
yy=yy+0.27906
*enddo
xx=0.055588
*do,ii,1,n2+1,1
n,20000+102+ii,xx,length+int,t
n,20000+102+(n2+1)+ii,xx,length+int,0
n,20000+102+2*(n2+1)+ii,xx,length+int,-t
n,20000+102+3*(n2+1)+ii,xx,-int,t
n,20000+102+4*(n2+1)+ii,xx,-int,0
n,20000+102+5*(n2+1)+ii,xx,-int,-t
xx=xx+0.227588
*enddo
uu=20000+102+6*(n2+1)
c************************
c****** Merging nodes
c************************
lsel,s,line,,47
nsll,s,1
nsel,a,node,,20001,20017
nummrg,node,1e-1,,,low
lsel,s,line,,50
nsll,s,1
nsel,a,node,,20018,20034
nummrg,node,1e-1,,,low
lsel,s,line,,55
nsll,s,1
nsel,a,node,,20035,20051
nummrg,node,1e-1,,,low
lsel,s,line,,62
nsll,s,1
```

```
nsel,a,node,,20052,20068
nummrg,node,1e-1,,,low
lsel,s,line,,67
nsll,s,1
nsel,a,node,,20069,20085
nummrg,node,1e-1,,,low
lsel,s,line,,72
nsll,s,1
nsel,a,node,,20086,20102
nummrg,node,1e-1,,,low
c****************
c****** Top/lower
c****************
lsel,s,line,,23
lsel,a,line,,28
lsel,a,line,,33
lsel,a,line,,86
lsel,a,line,,89
lsel,a,line,,93
nsll,s,1
nsel,a,node,,20103,uu
nummrg,node,1e-1,,,low
nsel,all
lsel,all
esel,all
c***********************************************
c************* truss elements for Vander Waals
c***********************************************
si   =  0.34         ! vander waal constant
ga   =  3.863e-13    ! vander waal constant
A_tr  =  0.090746    ! cross-sectional area of truss element
Rv   =  0.3816       ! Equlibrium distance between atoms (F=0)
kk   =  (8*ga*Rv)/(A_tr)
jj   =  10           ! term used to define element #
*do,i,1,nmax5,1
```

```
*do,ii,20001,uu,1
ndist,i,ii
dd = _return
*if,dd,lt,0.65,then
aa1 =  (si/dd)* (si/dd)* (si/dd)
aa2 =  aa1*aa1
bb2 =  aa2*aa2
et,jj,link8
r,jj,A_tr,(dd-Rv)/Rv
ss=(dd-Rv)*(dd-Rv)
E = kk*(bb2-aa2)/ss       ! Youngs modulus of truss element
c***************************
c***************************
*if,E,lt,0,then
E=-E
*endif
c***************************
c***************************
mp,ex,jj,E
type,jj
mat,jj
e,i,ii
jj=jj+1
*endif
*enddo
*enddo
nsel,all
esel,all
lsel,all
finish
c*****************************************
c********** Boundary conditions
c*****************************************
/solu
nsel,s,loc,y,-int-l2
```

```
d,all,all
nsel,s,loc,y,length+int+l2
cp,next,all,all
nsel,r,loc,x,-int-w2
nsel,r,loc,z,0
f,all,fy,-1e-6
nsel,all
esel,all
solve
finish
```

Appendix 2

Third Node Criterion

In the context of the stress-at-a-distance or third-node criterion, a stress is considered at a small distance from the region experiencing singular behaviour. Stress values were therefore taken in such a way that they remained uninfluenced by the singular stress field but still close enough to be considered an approximation for the maximum stress values. In finite element based analysesa distance equal to third node from the edge of a bi-material interface (as shown in Fig.A1) is often considered as appropriate for avoiding singular stress values.

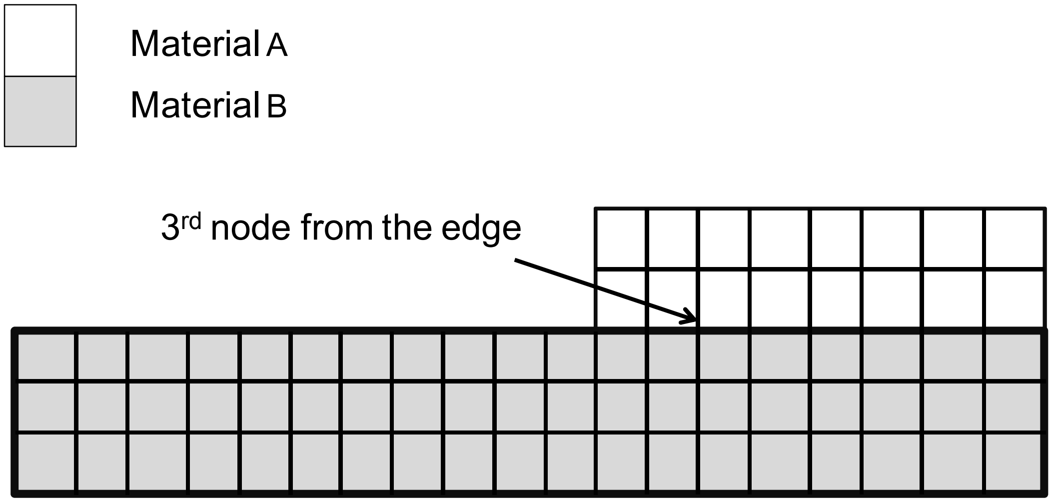

Fig. A1 *Finite element mesh showing location of third node from the edge considered for the stress analysis.*